UNIVERSITÀ
DI TRENTO

DEPARTMENT OF INDUSTRIAL ENGINEERING

Doctoral School in Materials, Mechatronics and Systems Engineering
XXXIV *Cycle*

Rolling-diaphragm hydrostatic transmission for the remote actuation of high-performance robots

SUPERVISORS:
Prof. Marco Fontana
Prof. Luca Zaccarian

PHD CANDIDATE:
Marco Bolignari

APRIL 2022

Abstract

The capability of safely operating in crowded, unstructured, anthropic environments led to a rapid spread of force-controllable collaborative robotic arms. However, the conflicting requirements posed by the traditional industrial applications in terms of operating speed and desired impedance still represent an unsolved trade-off. **R**olling **D**iaphragm **H**ydrostatic **T**ransmissions (RDHTs) are an ideal technology to merge collaborative and industrial robots in a unified advanced technological paradigm. Shaping a suitable open-loop response, regardless the applied control, by embedding requirements of safety and performance in smart mechanical structures is the key principle that drove this study: lightweight design and backdrivability are considered as the ultimate approach to the design of the next generation of human-like robotic arms. RDHTs are simple, passive systems that reflect torques across long distances in the form of fluid pressure and enable the remote positioning of electric motors, whose mass is taken away from the robot. Remotely located low-inertia direct or quasi-direct drive actuators, transparent and stiff torque transmission of the motors' action to the joints, and lightweight links are the main ingredients to create safe robots with low mechanical impedance, high specific power, excellent backdrivability and large force bandwidth.

In this thesis, a modular robotic joint based on novel hydraulic cylinders is developed; the cylinders implement rolling diaphragms and feature a minimally constrained floating-bonnet architecture that enables zero-leakage, low-friction operation. The joint generates a maximum rated torque of 25 Nm and exhibits a static friction value of just 0.24 Nm (0.96% of the maximum rated torque). Moreover frictional properties are independent of the applied load, which is a favorable feature inaccessible to the widely-used cable-based transmission systems. Exploiting a low-cost pressure sensing technique, a Smith-predictor-based joint torque control is developed to achieve enhanced torque setpoint regulation and high-quality physical Human-Robot Interaction (pHMI). Experimental tests show a reduction in backdriving torque of 67% and in settling time of 95% with respect to the open loop. The open-loop response is still largely acceptable over the whole range of frequencies that characterise realistic scenarios of manipulation and interaction. An advanced configuration of the robotic joint equipped with pressure sensors is then integrated in a remotely-actuated planar robotic arm. Excellent force controllability is confirmed in collaborative manipulation tasks that involve the displacement of a heavy payload over its entire workspace. The novel layout of the rolling diaphragm cylinders is further challenged by developing a miniaturized pneumatic version of the transmission system with intrinsic series-elastic properties for the remote actuation of the ankle joint of an agile hopping robotic leg. Finally, an effective solution for implementing programmable physical damping in hydrostatic transmissions is conceived.

I'm not giving up on you.
You do not understand this yet,
but people need you.
So let's get back to work!

– Big Hero 6 –

List of Publications

List of papers published during my PhD:

- [1] M. Bolignari, G. Moretti, and M. Fontana. Design and experimental characterisation of a hydrostatic transmission for upper limb exoskeletons. *IEEE/RSJ International Conference on Intelligent Robots and Systems (IROS)*, pp. 2768-2773, 2018.
- [2] M. Bolignari and M. Fontana. Design and experimental characterization of a high performance hydrostatic transmission for robot actuation. *Meccanica*, vol. 55, no. 5, pp. 1169-1179, 2020.
- [3] I. D. Sîrbu, G. Moretti, G. Bortolotti, M. Bolignari, S. Diré, L. Fambri, R. Vertechy and M. Fontana. Electrostatic bellow muscle actuators and energy harvesters that stack up. *Science Robotics*, vol. 6, no. 51, 2021.
- [4] M. Bolignari, G. Rizzello, L. Zaccarian and M. Fontana. Smith-predictor-based torque control of a rolling diaphragm hydrostatic transmission. *IEEE Robotics and Automation Letters*, vol 6, no. 2, pp. 2970-2977, 2021.

List of submitted papers (currently under review):

- [5] M. Bolignari, A. Mo, M. Fontana and A. Badri-Spröwitz. Diaphragm Ankle Actuation for Efficient Series Elastic Legged Robot Hopping. *IEEE Robotics and Automation Letters*, 2022.

Contents

Chapter 1

Introduction

The next generation of robots is expected to spread in our society and enhance human lifestyle by addressing issues of various aspects of our daily life. Robots will safely interact with humans, operate in crowded and unstructured anthropic environments, and accomplish repetitive-yet-dexterous tasks that nowadays burden on human workers. Typical requirements of highly-specialized industrial robots and safe collaborative robots, currently lying into two separate technological families, will merge together giving rise to an advanced common design paradigm. Safety and performance will be the key features embodied by the next generation of robots, uncompromisingly. A radical change in design methodologies of robotic architectures is then required, concurrently redefining mechanical, control and sensing strategies.

1.1 Electric Actuators: Performance & Safety

Conventional industrial robots implement dexterous serial kinematics, actuated by electric motors located closely to each joint in order to maximise transmission stiffness, controllability and position accuracy. In this configuration, proximal joints undergo large torques to accomplish tasks and sustain the weight of distal motors. Because of low specific torque characterizing electric motors, high torque requirements are associated with large mass and size of the actuator: direct-drive actuation fails in conferring a suitably practical and slender size to robotic arms

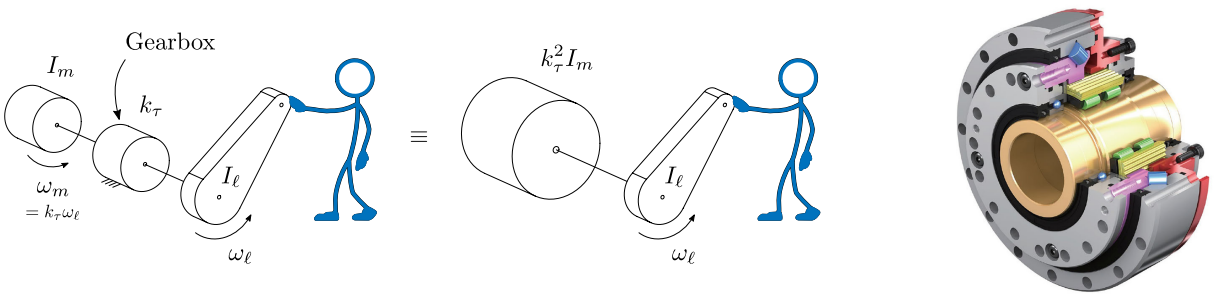

Figure 1.1: *Left:* inertia amplification generated by the gearbox; the amplification effect is represented by two equivalent schemes. Constant $k_\tau^2 I_m$ is called "reflected inertia". *Right:* harmonic-drive gearbox commonly used in robotic arms to obtain high gear ratios.

[6, 7]. Necessarily, electric motors have to be miniaturized and gearboxes are used to amplify their rated torque by a factor $k_\tau > 1$ [8]. Constant k_τ is called "gear ratio". This strategy allows building robots capable of successfully perform a number of complex, precise and accurate tasks, but the resulting large output impedance makes them unsuitable to manage interactions. During motion, geared motors spin k_τ times faster than the corresponding joints, gaining high kinetic energy and making their inertia appearing k_τ^2 times larger at the output, where the robot interacts with the external environment; Fig. 1.1 explains this condition by means of two equivalent schemes. Certainly gearboxes allow the selection of smaller and lighter motors, i.e. smaller I_m, but in practical scenarios (realistic components) the effect of the k_τ^2 amplification dominates, resulting in large output impedance and unsafe interaction. Having motors spinning k_τ times faster, also poses upper bounds to the maximum speed of the joint, thus limiting the execution speed of the tasks.

The major danger in human-robot-interaction, which may result in serious injury, is the possibility of impact loads generated in case the robot unpredictably comes in contact with a human being during the execution of a given task. Several indices have been defined to address the safety of interaction between humans and robots. The Head Injury Criterion (HIC) is the most widely used one; it considers the accidental collision between the robot and the head of a worker during an uncontrolled impact and relates the injury level to head acceleration and impact duration. Intense accelerations are tolerable only if the impact lasts a very short time, namely less than 10–15 ms [9]. Effective strategies for reducing accelerations consist in decreasing the total amount of kinetic energy transferred to the human body and increasing the total duration of the energy transfer, [10]. Soft covering of robotic links can consistently reduce injury risks but covering thickness is commonly required to be large and impractical (more than 120 mm for standard geared manipulators [11]). Clearly, adding large amounts of soft covering and forcing robots to move slowly do not address the root cause of high-impact loads. Extensive sensorization has been investigated to employ traditional robotic arms in scenarios where safety is critical. Force control strategies have been developed to handle accidental collisions with very little knowledge of the surrounding environment and dynamical characteristics of the robot itself. Joint-level torque sensing [12] and active impedance control improve low-speed backdrivability and extend interactive and safety capabilities of the robot to its entire body [13]; the concept of *whole body manipulation* also arose [14]. However this approach does not prove robust with respect to the variety of different environmental properties the robot may interact with (see Appendix A for details about contact instability and *chattering*) and it inherently poses upper bounds to admissible control gains. It turns out that limited-bandwidth controllers are unable to modulate the robot response beyond a certain cut-off frequency. The combination of control frequency limitations and the high-frequency nature of impact loads makes these strategies ineffective in modulating the robot response during unexpected collisions. The key role played by intrinsic open-loop response in high-frequency interactions and collisions emerges. It might be stated that the dynamical transparency of the device is dominated by its frictional and control characteristics at low frequency, while it is dominated by its effective inertia at high frequency. The large effective inertia of most modern robotic arms has been identified as a major limitation. Making a high-impedance robotic structures behaving gently and safely in unstructured environments is basically an hopeless task [9]. The solution to reducing the effective impedance, and thus improving safety, is to build lightweight, low-inertia manipulators. Moreover, injury hazard must be

prevented under any working condition, also in case of software, electrical or mechanical failures; sensors and control alone cannot provide a satisfying solution to the problem. The concept of *inherently* safe robots has therefore been devised, and the new design paradigm of embedding the demanded safety capabilities in appropriate smart mechanical structures rose.

1.1.1 Series Elastic Actuators

In 1995 *Series Elastic Actuators* (SEA) [15] first offered a solution to the problem of high-impedance actuators, meeting inherent safety requirements using elastic joints. Elastic elements, such as springs, are purposely introduced at the gearbox output in order to create a compliant connection with the link; the name Series Elastic Actuators well describes this topology. Elasticity dynamically decouples the rotational inertia of the motor from that of the robotic joint, critically reducing the arm output impedance and guaranteeing safety across the frequency spectrum. Additional energy storing capabilities are provided, increasing efficiency of cyclic tasks, such as legged locomotion. Also, because of the increment in reflected inertia caused by gearing, impact loads generate much higher forces on the gear teeth and failures of gearing due to shocks usually happen. For lightweight actuators the peak torque is more commonly limited by the gearing structural limits than by the motor. Intrinsic elasticity of SEAs low-pass filters the shock loads and decreases the peak forces on gear teeth, thereby protecting the structural integrity of the gearbox. The presence of the elastic element allows sensing the transmitted torque according to the Hooke law by measuring the differential displacement through the spring and relying on previous knowledge of spring stiffness; the Hooke model is reasonably accurate and reliable in most of practical cases. Sensing torque and controlling the spring deformation turns the force control problem into a position control problem, greatly improving torque accuracy because position is more easily controllable through geartrains than torque. Exploiting feedback control based on such a downstream sensing also compensates for torque errors usually caused by the introduction of gearing, such as friction and backlash; backdrivability can be easily restored. Series elasticity gives the actuator back the qualities that are lost when gears are introduced [15], yet maintaining high specific torque. Although elasticity beneficially smooths impulsive loads, also the actuator output is low-pass filtered and the actuation bandwidth is indeed limited; furthermore stability margins and torque accuracy are enhanced by lowering the interface stiffness. Despite the great contribution offered by SEAs in breaking the traditional “stiffer is better” design paradigm, an intrinsic trade-off between safety and performance is established.

1.1.2 Variable Stiffness Actuators

Combination of low-frequency benefits and high-frequency limitations determined by the presence of intrinsic elasticity led series elastic actuators to naturally evolve into *Variable Stiffness Actuators* (VSA) [16]; VSAs allow the passive compliance of transmission to vary during the execution of the task. The stiffness modulation strategy actually mimics the behaviour adopted by humans and many biological organisms, which change the stiffness, and therefore the impedance, of their limbs by contracting and relaxing muscles. Muscles are contracted when performing low-speed tasks that require position and force accuracy, while they are relaxed when performing highly dynamical tasks where energy storage, disturbance rejection and balance maintenance

are critical. The capability of reducing structural impedance also helps biological organisms to prevent damaging the their own body in case of high-speed or unexpected collisions. Similar considerations can be translated to robotics. Furthermore, optimal solutions to the minimum-time control problem under safety guarantees have been determined in [9] exploiting stiffness modulation capabilities. The best strategy to drive the robot from a given initial state to a given final state as quickly as possible while guaranteeing desired levels of safety along the entire trajectory (measured in terms of injury criteria) consists in disposing of high transmission stiffness at low velocities and low transmission stiffness at high velocities. This solution is also intuitive. High stiffness is desired in the initial phase of the task to promptly put links in motion. Similarly, high stiffness is also beneficial in the final deceleration phase to limit the amplitude of oscillations about the target position. Safety is ensured because velocities are small. During the portion of trajectory laying between acceleration and deceleration phases, low transmission stiffness is therefore viable because links move at high cruise velocity without requiring sudden corrections or accelerations; low stiffness also comply with safety requirements in this high-speed phase, whereby motor and joint inertia have to be decoupled. Popular solutions to simultaneously control joint stiffness and position (i.e. equilibrium point) consist in using two actuators connected to the same joint by means of nonlinear elastic elements, such as springs [17] or pneumatic muscles [18]. Other topologies make use of compliant constraining of transmission elements like belts and cables [19, 20], cam mechanisms [21–23], or variable lever-arm length [24–26]. Anyway, two actuators are always needed to implement variable stiffness robotic joints: this increases robotic arms mass and size. Moreover implementing variable stiffness at mechanical level usually introduces high complexity in the joint design, revealing impractical and too expensive for most of real-world applications. Finally, limitations exist to the stiffness modulation velocity and to the range of stiffness values that VSAs can generate.

1.2 Remotization

Lightweight design and high backdrivability can be considered as the ultimate approach to human-like manipulators. “Remotization” approaches can pursue this goal. Remotization consists in relocating actuators far from the robotic structure and reflecting their action to the robotic joints by means for transmission systems. The weight of the motors is therefore relieved on the robotic structure, which results lightweight and slender. Since motors are placed on the ground, their weight and size can be large, and the use of gearboxes is prevented: direct-drive or quasi direct-drive actuation is therefore feasible, minimizing the output inertia and the stored kinetic energy associated with motor rotation, even at high speeds. Safety is guaranteed under any working condition. Compliant drivetrains are no more needed and high-frequency performance is preserved. Moreover, this configuration allows actuators to also act as torque sensors, thereby enhancing the control stability of interaction with the surrounding environment. Partial remotization and quasi-direct drive actuation can be achieved via differential mechanisms [27] or similar solutions, but despite structural simplicity, actuator mass is not completely remotized and arm structure results bulky.

1.2.1 Closed-loop Kinematics

One viable solution to implement remotization is closed-loop kinematics.Motors actuate a set of joints fixed to the ground and a closed-chain combination of lightweight rod-like elements defines the motion of the end effector in the space. Also, closed-loop kinematics generally induces only axial forces on these rod-like elements, preventing structural bending and therefore determining a stiff and transparent reflection of the motors' action to the end-effector. Therefore, low mechanical impedance, excellent backdrivability and high force-control accuracy are achieved. Robotic legs for highly agile locomotion of ATRIAS [28] and MIT Cheetah [29] have been designed based on closed-loop kinematics, showing excellent intrinsic dynamical properties. Motors are not placed on the ground in this case, but they are placed in the robot torso instead, which is the body segment that experiences the lowest accelerations during locomotion; remotization is still dynamically effective in this configuration. Despite a set of attracting features, closed-loop mechanisms are not generally used to implement collaborative or humanoid robotic arms because of their limited workspace and the difficulty in implementing a large number of degrees of freedom. Workspace restrictions and singularity limitations can be overcame through redundant actuation [30–33] but structural and control complexity increase considerably.

1.2.2 Cable-based Transmissions

In those applications where an open-chain kinematic is preferred, the technical problem is then shifted to the development of lightweight transparent transmission systems. Cable actuation has been mostly investigated among existing solutions. "*Bowden cables*", for example, are steel cables running inside a polymeric sheaths, similar to those used in bicycle brakes. They can be arranged in antagonistic pairs or in single push-pull configurations [34]. Applications of bowden cables have been investigated for wearable devices [35] because of their marked lightness and versatile integration into mechanical soft structures. On the other hand, their performance is poor. Bowden cables suffer from wear, backlash, torque hysteresis [36], and high friction with nonlinear dependence on bending angle and applied load [37]. In the hand exoskeleton developed in [38] the percentage of friction torque accounting for the driving torque is up to 95% during stable movements. Backdrivability can be recovered by exploiting combination with series elastic elements in distal position [39], but good-quality response is not achievable at high frequency. Efficiency and performance are guaranteed when steel cables are routed through the mechanical structure by running on pulleys instead of sliding into polymeric sheaths. In this case only the antagonistic layout is feasible. Steel-cable transmissions have been extensively applied to the design of interactive and collaborative robots because of their efficiency, lightness, and reduced encumbrance [14], [40], [34]. Depending on the application, small or large reduction ratios in distal locations are usually needed to make cables carrying a fraction of the tension force needed at the joint. Thereby smaller cross-section cables can be used and their routing result easier through the internal structure of the arm because of the larger tolerable curvature; this is also beneficial in terms of transmission stiffness [10]. Anyway, the routing complexity increases when building multi-degree of freedom robots and the need for deviating the heavily loaded cables about a multitude of pulleys generally introduces compliance in the transmission. Flexible modes limit the bandwidth of closed-loop torque control. Moreover, cables wear, complex assembling and high integration of cable routing in the link geometry make this solution not

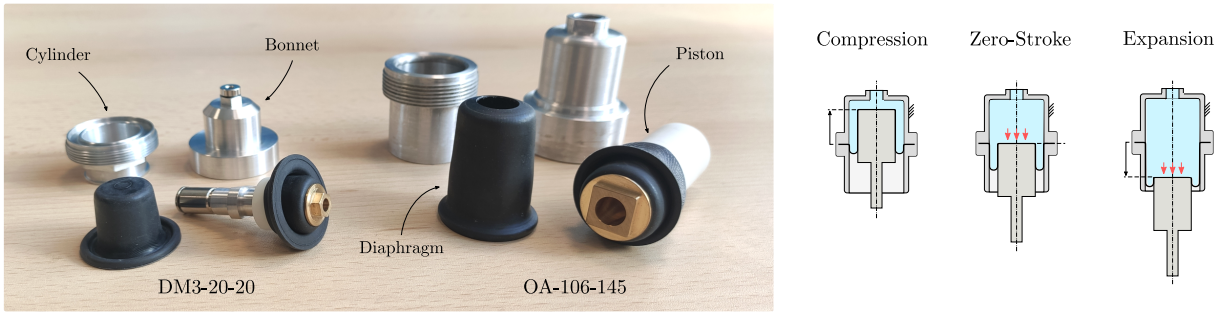

Figure 1.2: Rolling Diaphragm Cylinders. *Left:* diaphragms and custom-made components. The OA-106-145 diaphragms by DiaCom are used to build the devices presented in Chapters 2, 3, 4 and 6, while DM3-20-20 diaphragms by Fujikura are used in Chapter 5. *Right:* working principle of the rolling diaphragm, bending and unbending along the cylinder stroke.

versatile and impractical. Any time the transmission is modified, the link has to be redesigned; any time the shape of the link is modified, the transmission has to be redesigned.

1.2.3 Distributed Macro-Micro Actuation

Bandwidth limitations due to the compliance of cable-based transmissions can be recovered by means of the advanced and sophisticated "*Distributed Macro-Micro*" (DM^2) approach: small-size direct-drive actuators are placed at the robot joint to generate those small-amplitude high-frequency torque components that are filtered out by the cable-based transmission [41], while geared actuators are still remotely placed. In general, macro-micro actuation can be realised by connecting two actuators to each robotic joint in parallel. One actuator is highly geared to generate the slowly-varying large-amplitude torques in static or quasi-static regime (generally associated with gravity compensation); it is connected to the robotic joint by means of an elastic element to guarantee low impedance, as series elastic actuators do. A second small actuator is rigidly connected (direct drive) to the same joint in parallel: this second actuator is responsible for the generation of smaller amplitude torques beyond the cut-off frequency of the first compliant actuator. The resulting system is characterised by low impedance and is capable of generating torques in a large range of frequencies. The same concept has also been successfully applied to pneumatic-muscle-based robots [42]. Actuation authority is well shaped across the frequency spectrum but distal mass is added again and the use of two actuators for each joint increases complexity and cost.

1.3 Hydrostatic Transmissions

In this work, **R**olling **D**iaphragm **H**ydrostatic **T**ransmissions (RDHTs) are selected as the best candidate to create the new generation of human-friendly robots.
Requirements of safety, dynamical transparency and productivity can be met by pursuing design criteria of lightness, backdrivability, high-speed and high specific-power. Electric motors achieve accurate control of interaction forces at low and high speeds, but low-specific torque prevents their direct implementation in robotic arms. On the other hand, hydraulic components (transmission hoses, linear cylinders, single/double vane actuators) are lightweight and provide

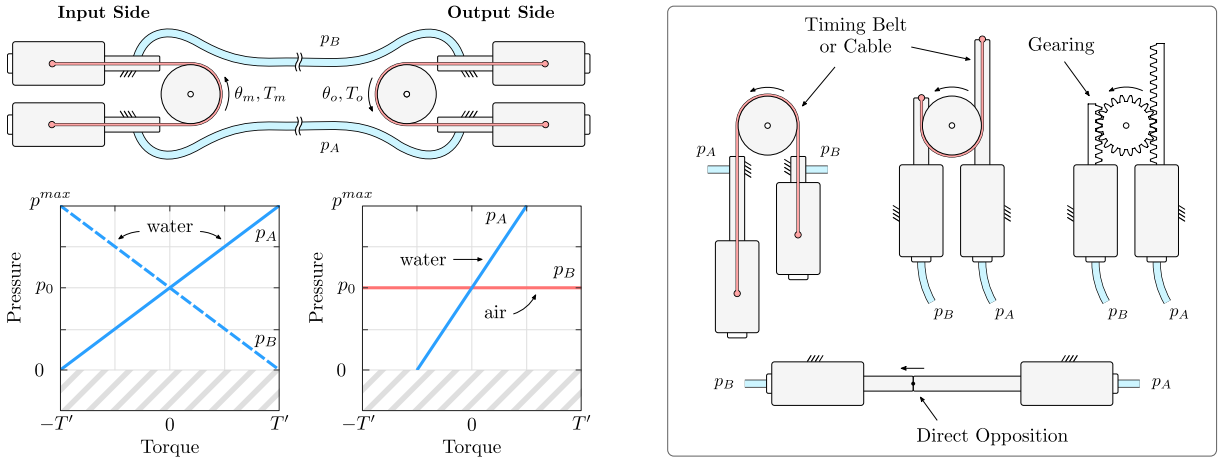

Figure 1.3: Closed-volume passive hydrostatic transmission. *Top-Left:* scheme of the hydrostatic transmission. Fixed-piston moving-bonnet cylinders are used in this case. External torque T_m in applied on the input pulley by the selected actuator, while torque T_o is applied on the robotic joint/link by the transmission. *Right:* alternative antagonistic configurations. *Bottom-Left:* Pressure–Torque transformation; incompressible fluids are represented in blue (water), compressible fluid are represented in red (air).

high specific torque and power, but traditional valve-based actuation units prevent backdrivability and determine high impedance and complexity. The challenge of designing gentle-yet-powerful manipulators can be achieved by combining the specific power of hydraulic systems and the controllability of electric motors: electric actuators, placed at a proximal location, provide the input actuation power and flexible hydraulic elements, named “hydrostatic transmissions” in this configuration, distribute power across the system. In particular, hydrostatic transmissions gain attractiveness when based on hydraulic cylinders that implement rolling diaphragms instead of traditional sliding seals. Rolling diaphragms are reinforced rubber seals that roll from bore to piston surfaces by bending and unbending, instead of sliding, Fig. 1.2. Rolling diaphragms solve the well-known trade-off between static friction and leakage that affect traditional hydraulic cylinders. In traditional devices O-ring-like seals are generally compressed between bore and piston surfaces to prevent leakage, determining high friction and stiction that degrade transparency and controllability. Backdrivability can be restored by removing sliding seals and relying on the accurate manufacturing of bore and piston surfaces [43]; however leakage is substantial in this configuration and external compensation systems are required, increasing structural and modeling complexity. When using rolling diaphragm, instead, the working fluid is perfectly sealed and the sliding contact is replaced by rolling contact, achieving virtually frictionless functioning. The absence of sliding surfaces also implies simplicity and cost-effectiveness, because bore and piston do not wear and can be manufactured with large tolerances. Moreover, the working fluid is not required to lubricate sliding seals: common purified water can be used, which incidentally has lower viscosity and higher bulk modulus than oil, ensuring cleanliness, lower damping and higher transmission stiffness.

The use of hydrostatic transmissions for the actuation of robotic interactive devices was first suggested by in Arthur Lutz and Irving Wagman in 1965 [44]. No further publication followed until 2004, when the modern implementation of hydrostatic transmissions based on antagonistic pairs of hydraulic lines, Fig. 1.3 (left), was suggested in [45]. This configuration allows bidirec-

tional actuation. Rolling diaphragms, in fact, cannot support reverse pressure: if the pressure gradient reverses across the membrane, i.e. the fluid pressure is lower than the atmospheric pressure, the convolution that rolls from bore to piston would reverse, and the diaphragm jam. Practically, rolling diaphragms can exert forces in a single direction, i.e. along the direction of expansion only. These cylinders cannot compress on their own and a preload or antagonistic action is required. Indeed, bidirectional actuation can be achieved by preloading the cylinders by means of external elements, like springs. However, the presence of elastic elements produces spring-rate effects along the cylinder stroke, reducing the maximum force that the cylinder can generate according to the deformation state of the elastic element. Homogeneous properties over the entire range of motion can be generated by preloading the cylinder by means of constant-force mechanisms, but they are generally bulky, heavy and complex. An effective solution for preloading the system and allowing bidirectional actuation consists in connecting two identical fluid lines, equally pressurized at rest $p_A = p_B = p_0$, in antagonistic configuration. Using a second hydraulic line as preloading element to balance the mechanism doubles the mass of the transmission, but still offers higher specific power than using springs or constant-force solutions. In Fig. 1.3 (left) a pair of cylinders balance each other at each end of the transmission by mean of belts (or any other suitable flexible transmission element) routed about input and output pulleys; alternative antagonistic configurations are shown in Fig. 1.3 (right). Pulleys –and the corresponding shafts– are the interfaces through which the transmission exchanges power with the external environment. When no external action is applied on the pulleys, pressures p_A and p_B are equivalent to p_0 and the mechanism is in equilibrium. When a positive torque (or rotation) is applied at the input pulley, instead, the pressurization level of the two fluid lines is perturbed with respect to p_0, increasing p_A and decreasing p_B, Fig. 1.3 (bottom-left); a differential pressure $\Delta p = p_A - p_B$ is then originated. Δp propagates through the fluid lines up to the output side, where two output cylinders convert Δp into torque (or rotation) again; the same description holds in case of application of negative torques. Positive fluid pressure is guaranteed by pre-pressurizing the cylinders up to pressure p_0, equal to one-half of the maximum operating pressure p_{max} required by the selected task; equivalently, the maximum torque required by the given task does not generate pressure drops large enough to induce negative pressure in one of the two channels. Pre-pressurization is performed by means of external apparatus, then disconnected during standard operating conditions. The overall transmission is therefore a closed-volume, passive and likely symmetrical mechanism that transparently reflects torques form input to output and vice versa, without necessarily requiring external control, compensation or actuation systems. Pre-pressurizing the antagonistic cylinder pairs also produces a beneficial anti-backlash effect on the mechanical elements that transform linear motion into rotation, e.g. pulleys and belts. It is worth noticing that small reduction ratios can be implemented with high efficiency and low mechanical complexity by selecting different cylinder diameters at input and output sides.

The previous description holds in case the same fluid is used in both of the transmission channels; using different fluids is certainly interesting. Fig. 1.3 (bottom-left) shows also the alternative working principle conceived in [46] by filling the antagonistic lines with different fluids: in particular, when the bulk modulus of the two fluids differs by several orders of magnitude, only the fluid with higher bulk modulus takes part to the torque transmission (blue line) while the other one maintains at virtually constant pressure (red line), acting as a constant force element. This is the practical case of coupling hydraulic and pneumatic lines. In fact, the change in volume corre-

sponding to eventual input or output rotations generates a pressure increment in the stiffer fluid that is considerably higher than the increment generated in the compliant channel. The pressure variation of the air volume is practically negligible and the pressure difference Δ_p is generated by the pressure variation of the hydraulic channel alone, reducing by half the maximum rated torque and the transmission stiffness. Despite halving the performance of the transmission in terms of maximum rated torque and stiffness, this configuration offers attractive advantages in implementing multi-dof systems: since the air pressure maintains constant, one single pneumatic channel can be shared between all of the joints of the robotic arm, determining a tremendous savings in the number of hoses routed around the arm structure, especially in close proximity of the robot base. The actuation of a robotic arm with N degrees of freedom requires a total of $N + 1$ hoses in the hybrid water/air configuration, instead of $2N$ hoses required by the fully hydraulic configuration. Moreover, pneumatic lines can be realised using small highly-flexible hoses made of soft material because of the low air viscosity and the negligible influence that relatively small changes in the air volume have on the transmission response. Anyway, the analysis of the fully-hydrostatic transmission will be preferred to the hybrid configuration in this thesis, because its superior performance in terms of maximum rated torque and stiffness better suit the objective of investigating the maximum controllability performances achievable by hydrostatic transmissions.

Recent research focuses on exploring alternative working principles, such as soft vacuum tendons [47] and variable stiffness mechanisms [48]. Intrinsic stroke limitations of rolling diaphragms have been investigated in [49] and custom fabrication processes have been devised to obtain long strokes. High-bandwidth ankle exoskeletons have been developed in [50, 51]; magnetorheological clutches have been used to decouple the motor and the robotic joint inertia, and further decrease the impedance of RDHT-based devices. Low-efficiency is expected in this configuration. Related research focuses on generic interactive robotic arms [52] and wearable supernumerary robotic arms [53, 54] and legs [55]. Other applications include advanced force-controllable grippers [56, 57], telepresence avatars [46] and teleoperation manipulators for extending the reach inside MRI bores [58–60].

1.4 Vision and Goal Statement

Encouraged by the unprecedented set of attracting properties that make Rolling Diaphragm Hydrostaic Transmissions standing out from other existing actuation solutions used in robotics, see Tab. 1.1, this thesis aims at investigating the use of RDHTs to create a new generation of powerful, efficient, lightweight, force-controllable robots. High specific power, extreme mechanical transparency, accurate torque rendering and simple controllability make RDHTs good candidates for the actuation of safe interactive robotic devices, with the additional potential of tackling high-speed and heavy duty applications. RDHT-based robots may therefore represent the bridge between highly specialised industrial robots and safe interactive co-bots. The additional feature of modular design, allowing the use of the same joint design (both lightweight and powerful) to indiscriminately actuate any degree of freedom of the robotic structure, offers a reduction in design, manufacturing and maintenance complexity. Together with intrinsic simple manufacturing (absence of demanding tolerances) and the usability of standard industrial brushless motors (no optimized and miniaturized solutions are required), RDHTs are cost effective with respect to

Table 1.1: Comparison of the actuation principles. The table highlights the weaknesses of existing technologies. Backdrivability, inertia, torque bandwidth, mechanical complexity and joint size have been extensively described in the chapter. Workspace extension refers to the possibility of easily increase the reach of the robotic arm with the minimum redesign effort or without excessive increment of actuators' power and size. Customization is the property of easily redesign the shape of the links or change their length with the minimum redesign effort.
*robots with highly geared joints are assumed equipped with torque/force sensors to enable force control

Actuation	Backdrivability (good = high)	Inertia (good = low)	Torque Bandwidth (good = large)	Mechanics Complexity (good = low)	Joint Size (good = small)	Workspace Extension (good = large)	Customization (good = easy)
Geared motors*	fair	**bad**	fair	fair	**poor**	fair	fair
Series Elastic Actuators	good	fair	fair	fair	**poor**	fair	fair
Variable Stiffness Actuators	good	fair	good	**poor**	**poor**	fair	fair
Closed-loop kinematics	good	good	good	fair	fair	**poor**	**poor**
Bowden cables	**poor**	good	**poor**	good	good	fair	good
Cables routed on pulleys	good	good	fair	**poor**	good	good	**poor**
Distributed Macro-Micro	good	fair	good	**poor**	fair	good	**poor**
RDHT	good	good	good	good	fair	good	good

many existing technologies. Absence of leakages, cleanliness of water-based functioning and silent operation (no gearing or pneumatic valves) motivate possible application of RDHT-based devices in medical and cleanroom environments. Finally, having the actuation block detached from the mobile structure of the robot facilitates the cooling of motors with appropriate external systems. The further possibility of sealing the actuation unit combined with a sensorless configuration of the robotic arm gives the premise for creating robots capable of operating underwater or in hazardous (explosive) environments.

1.5 Summary

This thesis is a comprehensive study of the application of Rolling Diaphragm Hydrostatic Transmissions to remotely-actuated robotic arms. It collects the results that I achieved during my PhD project, from November 2018 to February 2022.
This thesis is divided into seven chapters that identify the main thematic areas of my work, followed by appendices describing technical details and theoretical background I consider highly motivating or instructive.

- Chapter 2 aims at achieving extremely transparent mechanical response of the transmission. The prototype of a remotely actuated robotic joint is developed based on the novel design of low-friction hydraulic cylinders. Static and frictional characteristics of the RDHT-based actuation system are experimentally assessed.

- Chapter 3 extends the characterization of the transmission response to the frequency domain and exploits a low-cost, pressure-based, distal sensing technique to develop a Smith-predictor-based joint torque control and achieve enhanced torque setpoint regulation and high-quality pHMI. Experimental tests validate the significant advantages of the closed-loop control architecture.

- Chapter 4 offers the overall validation of the proposed design criteria by combining the results of previous chapters to build a lightweight, remotely-actuated, planar robotic arm. The robot is force controlled in a variety of experiments to analyse its accuracy and transparency features in various collaborative scenarios.

- Chapter 5 describes a side-project in collaboration with the Max-Planck-Institute for Intelligent Systems of Stuttgart. A miniaturized pneumatic version of the transmission system with intrinsic series-elastic properties for the remote actuation of the ankle joint of an agile hopping robotic leg is developed. The hopping robot is characterised in agile forward hopping experiments.

- Chapter 6 extends the capabilities of RDHT with additional adaptable-damping features. The response of the system is characterized in the frequency domain and the range of values of the damping coefficient that can be generated is measured.

- Chapter 7 draws the conclusions of the thesis and analyses the overall picture of the project; future developments and applications are finally devised.

- Appendix A presents the analytical analysis of the effects produced by the main sources of compliance on the stability properties of force-controlled systems. In particular, it introduces the problem of noncolocation that plays a key role in the robot actuation through flexible transmission systems. This chapter is a literature review of papers that have been very instructive for me.

- Appendix B analyses of cogging torque produced by brushless electric motors and presents an effective compensation strategy.

Chapter 2

Working Principle, Design and Experimental Characterisation

2.1 Overview

This chapter focuses on the mechanical design and characterisation of hydrostatic transmissions for the remote actuation of highly-dynamical, lightweight robots. Direct or quasi-direct drive electric motors are placed away from the structure of the robotic arm and their power is propagated to the robotic joints, across long and possibly twisted pathways, in the form of fluid pressure. This provides high specific power and low-friction torque reflection. Hydrostatic transmissions are good candidates for the actuation of safe interactive robotic devices, with the additional potential of tackling high-speed and heavy duty applications.
The chapter is organized as follows. Sect. 2.2 gives an overview of the working principle of hydrostatic transmissions. Sect. 2.3 presents the design of an integrated robotic joint based on hydrostatic actuation and introduces the novel concept of low-friction "floating-bonnet" cylinder. Sect. 2.4 describes the test-bench used for experimental characterization. In Sect. 2.5 experiments are performed and the system is described in terms of static torque reflection, stiffness and friction. The indirect sensing of joint torque based on fluid pressure measurement is also investigated in the static case; extension to closed-loop and frequency-domain analysis will be presented in Chapter 3. Sect. 2.6 discusses the results and draws the conclusions of the chapter.

2.2 Working Principle

Fig. 2.1 (left) shows the scheme of the Rolling Diaphragm Hydrostatic Transmission (RDHT) for the remote actuation of a single degree of freedom. The transmission is a passive element conceived to establish a transparent one-to-one connection between its input and output rotation axes; when implementing a robotic device, the electric motor is connected at the input and the robotic link is connected at the output. The kinematic coupling between the rotation of the input and output axis, θ_m and θ_o, is implemented through two fluid lines, nominally channels A and B. At each side of the transmission a pair of hydraulic cylinders couple the rotation of the axis with the fluid displacement inside the hoses. The two cylinders are balanced in antagonistic configuration about the rotation axis by means of flexible (yet inextensible) transmission elements, such

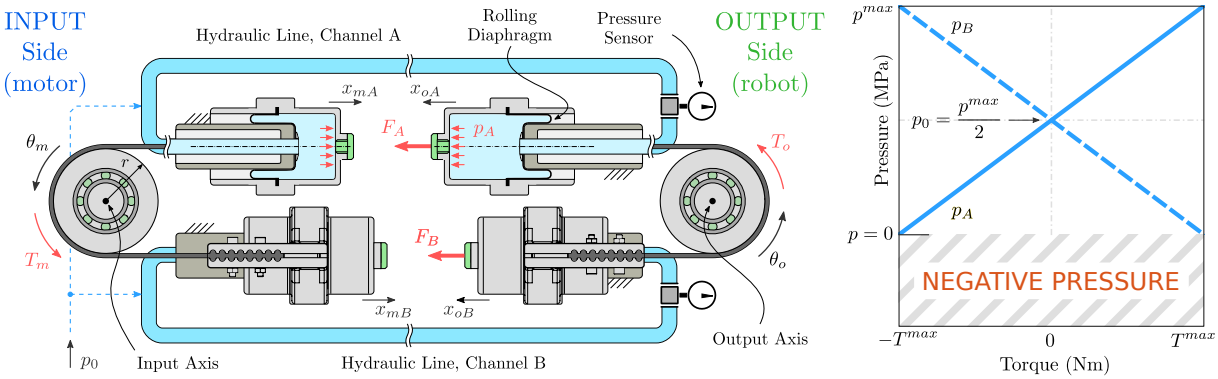

Figure 2.1: *Left:* Schematic of the hydrostatic transmission. θ_m and θ_o are the rotation the input and output shafts, T_m is the driving torque applied on the input shaft, and T_o is the output torque applied on the robot link by the transmission. The blue dashed lines represent the external pressurization system used to pre-pressurize the hydraulic channel up to initial value p_0. Afrer setting pressure p_0 the pressurization system is disconnected. *Right*: pressure-torque transformation taking place at the input and output ends of the transmission; indeed the transmission is symmetric and the plot abscissa can be referred to T_m or T_o indifferently.

as timing belts or steel cables routed around proper pulleys. The following kinematic relations between cylinder displacements and pulley rotation is determied at the input side

$$x_{mA} = -r\theta_m, \quad x_{mB} = r\theta_m, \tag{2.1}$$

and at the output side

$$x_{oA} = r\theta_o, \quad x_{oB} = -r\theta_o, \tag{2.2}$$

where constant r is the pulley radius. When the working fluid is incompressible, such as in the case of water or oil, the volume inside the transmission lines maintains virtually constant, implying $x_{oA} = -x_{mA}$ and $x_{oB} = -x_{mB}$ (all the cylinders has the same effective area), and therefore synchronous rotation $\theta_o = \theta_m$. However, some compliance exists in practice due to the presence of dissolved air and to the elasticity of hoses, belts and diaphragms. This kinematic relation holds as long as the transmitted torque is reasonably small and the operating condition is far from the resonance frequency.

The overall motion $\theta_o \approx \theta_m$ is consequence of the equilibrium between external torques and internal fluid pressures. As described by Fig. 2.1 (right), when a positive torque T_m is applied on the input pulley, the pressurization level of the two fluid lines is perturbed with respect to the initial value p_0, increasing p_A and decreasing p_B. A differential pressure $\Delta p = p_A - p_B$ is then originated, and pressures p_A and p_B evolve as follows:

$$p_A = p_0 + \frac{\Delta p}{2}, \quad p_B = p_0 - \frac{\Delta p}{2}, \tag{2.3}$$

with

$$\Delta p = \frac{T_m}{r A_e}, \tag{2.4}$$

where constant A_e is the effective area of the cylinders. Δp propagates through the fluid lines up to the output side, where two output cylinders convert it back into torque T_o. In fact, because of transmission symmetry, the transformation described in Fig. 2.1 (right) also takes place at the

output side – notice that T_m is the torque applied by external elements on the input pulley, while T_o is the torque applied by the output pulley on external elements –. Ideally

$$T_o = T_m. \tag{2.5}$$

Further details about internal forces produced by the antagonistic configuration at the output side are offered in Fig. 2.1 (left) (same reasoning holds at the input side). The two output cylinders apply forces F_A and F_B proportional to their internal pressure on their respective belt branches

$$F_A = A_e p_A, \quad F_B = A_e p_B. \tag{2.6}$$

When no external action is applied, pressures p_A and p_B coincide, determining the resting condition $p_A = p_B = p_0$; the two cylinders thus balance each other and no torque is generated on the pulley. When the two pressures are different, the cylinders are no longer balanced and thus a net torque T_p is generated according to the following algebraic relation

$$T_p = A_e r \Delta p. \tag{2.7}$$

Since the elements connecting the fluid action to the pulley (i.e. membrane, belts and bearings) are a source of reasonably low friction and hysteresis, the torque applied on the output pulley, i.e. acting on the robot arm, can be approximated to be the same as the torque generated by the pressure difference, namely $T_o \approx T_p$.

2.2.1 Pressure sensing

The accuracy of assumption (2.5), which defines transmission transparency, worsen at high velocities because of fluid viscous friction and resonance modes, while at low velocities it is affected by the frictional properties of the bearings mounted on the joint shafts and by reasonable levels of hysteresis associated with bending and unbending of membranes. Improved input-output transmission transparency can be pursued by designing a joint-level torque controller exploiting the feedback signal T_p (2.7), measured by means of pressure sensors placed at distal location, i.e. close to the output side. T_p is considered a reliable indirect measurement of output torque T_o. Measuring the output torque by means of pressure sensors instead of load cells or torque sensors is a cost-effective and robust solution.The challenge is then achieving large sensing accuracy and bandwidth. This chapter offers the experimental characterisation of measurement T_p in static conditions, while the analysis is extended to the dynamic domain in Chapter 3.

2.3 Robotic Joint Design

Fig. 2.2 (left) presents the novel design of an hydrostatic robotic joint based on rolling diaphragms. The robotic joint implements two hydraulic cylinders with fixed piston and moving bonnet, characterised by the novel layout called “floating-bonnet”, described in detail in Sect. 2.3.2. The two cylinders are balanced in antagonistic configuration about the rotation axis by means of two toothed pulleys (rigidly connected to the joint shaft) and two timing belts. The timing belts couple the shaft rotation and the cylinder linear displacements, guaranteeing synchronous motion. Belt

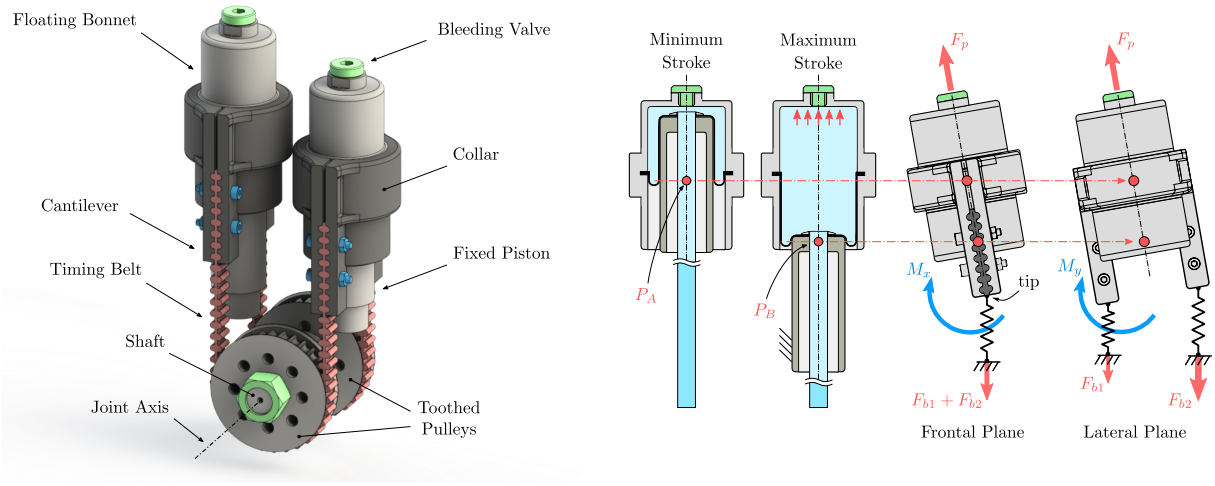

Figure 2.2: *Left:* Drawing of the hydrostatic robotic joint based on the floating-bonnet architecture. *Right:* Working principle of the "floating-bonnet" configuration. The convolution section moves from point P_A to point P_B along the full stroke of the bonnet. The cantilever always offer a lever to belt forces to generate restoring torques M_x and M_y in the frontal and lateral planes.

branches are connected to the corresponding cylinders by means of clamping elements called "collars". Bleeding valves placed on top of each cylinder allow a correct filling of the transmission channels with water, preventing residual air bubbles to be trapped into the fluid. Residual air bubbles would decrease transmission stiffness because of their compressibility, degrading positioning accuracy and control bandwidth. Bleeding valves are placed upwards with respect to each cylinder, where air bubbles accumulate: opening the valves easily allows for their expulsion.

2.3.1 Requirements and Specifications

The robotic joint is designed to provide a rotation angle of $\approx 140°$ and a peak torque of 20 Nm. These requirements are representative of a robotic elbow implemented in rehabilitation exoskeletons [61, 62], collaborative robots [42] or similar lightweight robotic applications [53]. Moreover, the joint geometry must be small enough to be integrated in a compact assembly that reasonably fits the shape of common robotic arms.

Both custom and off-the-shelf components have been chosen pursuing low-cost, easy manufacturing and easy availability features.The selection of the rolling diaphragms embedded into the hydraulic cylinders revealed the critical step in the definition of the overall geometry of the robotic joint. Off-the-shelf diaphragms are usually characterized by small stroke-to-diameter ratios. Diaphragms with larger ratios increase the angular stroke of the joint, but they are not commercially available and they have been developed for low-force applications only (i.e. in the range of 10–15 N) through custom manufacturing [49, 63, 64]. Feasible stroke-to-diameter ratio is obtained by selecting the OA-106-145 diaphragm from DiaCom Corp., characterized by a 24 mm piston diameter, a 27 mm cylinder diameter and a $x = 56.8$ mm stroke. According to the rotation requirement, a toothed pulleys having 23.9 mm primitive radius is selected. The resulting joint angular range is therefore $\theta = x/R = 136.2°$ where constant x is the diaphragm stroke and constant R is the pulley primitive radius. Providing the OA-106-145 diaphragm with a general purpose reinforcement fabric FA-0503 (polyester) with 11.6 N/mm tensile strength, the maximum

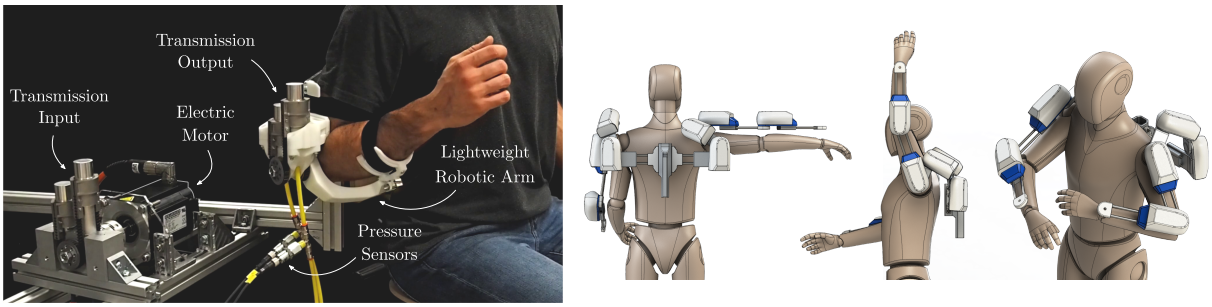

Figure 2.3: Joint integration. *Left:* experimental prototype of the remotely actuated exoskeleton elbow. *Right:* CAD conceptual modular design of a complete upper-limb exoskeleton.

safe working pressure results ≈ 2 MPa (burst pressure ≈ 8 MPa): accordingly, cylinders can exert up to a peak linear force of 1 kN (burst force ≈ 4 kN) and the overall joint can transmit a maximum torque of 25 Nm (burst torque ≈ 100 Nm). A better understanding of encumbrance and ergonomics of the proposed geometry is provided by the preliminary prototype of a remotely-actuated exoskeleton elbow presented in Fig. 2.3 (left); dimensions are comparable with those of human arms and the overall shape appears easily embeddable in the body of a robot link. In contrast with existing moving-piston configurations recently conceived [46, 47], the proposed layout allows a properly integration of the joint in the structure of a robotic arm by confining its encumbrance to a single side of the rotation axis. A more developed example is offered in Fig. 2.3 (right), showing the concept design of an upper-limb exoskeleton based on the proposed hydrostatic joint, which provides great mobility to the user's arm. Performing remote actuation by means of hydraulic lines, instead of using highly embedded cable-based transmissions, enables simple modification of the links' length to adapt the exoskeleton to different users.

2.3.2 Floating-Bonnet Cylinders

The novel "floating-bonnet" architecture conceived to create extremely low-friction and leakage-free hydraulic cylinders is the major contribution offered by the current chapter. Whereas the idea of floating-piston configuration was first presented in [46] and the implementation of rolling diaphragm cylinders with fixed piston and moving bonnet was fist proposed in [47], the novel floating-bonnet layout, which is actually a favorable combination of the two, has been invented in this PhD project; it was first presented in [1], and further refined in [2]. Differently from alternative moving bonnet solutions that employ bushing and sealing elements to steer the relative motion of moving parts [50, 53], bonnets are not subjected to any kinematic constraint in the novel floating configuration. The keystone of the proposed layout is the replacement of position constraints with a stable equilibrium of forces acting on moving parts. In fact, during experiments it was observed that constraining the rolling trajectory of diaphragms can produce internal loads acting on the bonnet and degrade the transparency of torque transmission. Elastomeric components, such as rolling diaphragms, are generally manufactured through molding process with relatively poor accuracy and every diaphragm can deviate from nominal geometry. Therefore, the floating solution allows the bonnet to assume the most convenient trajectory to compensate possible manufacturing or assembling errors without inducing reaction forces on the constraints. In other terms, the device remains transmission transparency even if the motion of the bonnet is not perfectly aligned with the axis of the piston or even not perfectly linear.

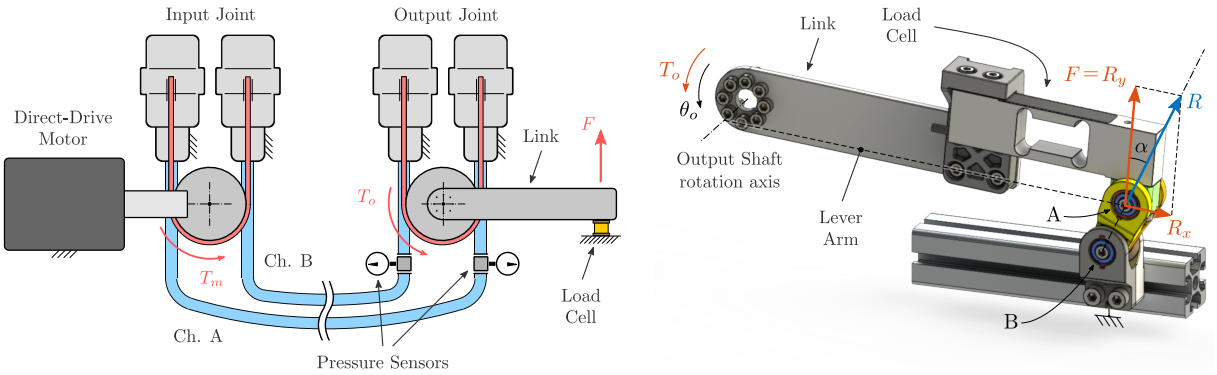

Figure 2.4: Experimental test-bench used for the static characterisation of the transmission system. *Left:* scheme of the overall actuation system. *Right:* detailed representation of the constraint scheme used for preventing the rotation of the output link and measuring its reaction force F by means of the load cell.

The floating-bonnet layout is described in Fig. 2.2 (right). The bonnet is actually suspended between the membrane, the fluid and two timing belt branches without requiring any additional "stiff" constraint. However, such a minimally-constrained architecture requires careful design in order to guarantee the stability of the bonnet along its full stroke. As mentioned above, during joint rotation the timing belts are conveyed by the bonnet which moves along the axis of the cylinder, while the diaphragm rolls form the piston to the cylinder surfaces. The diaphragm convolution section translate from point P_A to point P_B along the full axial stroke and it works as a spherical contact between piston and bonnet, which can be approximated to a pivot point about which the bonnet is free to rotate (red point in the drawing). The relative position between the pivot point and the bonnet determines the stability properties of the load scheme. In fact, the resultant force of the fluid pressure F_p is always aligned with the bonnet axis and it does not produce any moment about the pivot point; the only forces that produce a moment in case of bonnet rotation are those associated with the belts branches, F_{b1} and F_{b2}. When the bonnet rotates, either in the frontal or in the lateral planes, the cantilever beams offer a lever to forces F_{b1} and F_{b2} in order to generate stabilizing reaction moments M_x and M_y. It is worth noticing that the two cantilever beams are shaped according to the consideration that the load scheme guarantees stability as long as the tip of the two beams lies below the pivot point. The fully expanded cylinder (pivot point in position P_B) is the most critical configuration, since the shortest lever is offered to the forces F_{b1} and F_{b2}. If the beams are long enough to maintain the fully expanded configuration stable, then the stability condition is also satisfied in any other configuration. The length of such beams is chosen as trade-off between stability and overall added encumbrance.

2.4 Transmission Test-Bench

2.4.1 Implementation

A schematic drawing of the test-bench is shown in Fig. 2.4. The motor is connected at the input side of the transmission and the fluid hoses transmit the actuation torque T_m at the output side, where a link is connected. The load-cell measures the output force F and, consequently, the exact output torque T_o (2.8). Two pressure sensors, placed close to the output side, sense fluid

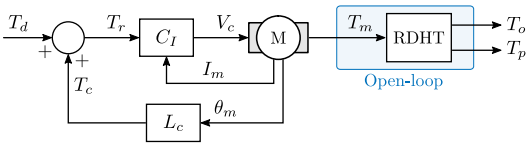

Figure 2.5: Scheme of the overall "actuation system", comprehending the hydrostatic transmission "RDHT", the electric motor "M", the current controller "C_I" executed in the motor driver and the cogging-torque compensation element "L_c".

pressures and therefore offer an indirect measurement of the transmitted torque T_p, calculated through equation (2.7). Direct and indirect measurements T_o and T_p are compared to assess the accuracy of torque sensing achieved by means of pressure sensors. The output link is constrained to the ground in a fixed position, i.e. $\theta_o = 0$, by means of the load cell, Fig. 2.4 (right). In order to measure the output torque T_o using a single-axis load cell, i.e. capable of measuring forces along the F direction only, this scheme guarantees that no external force, apart from those aligned to F, affects the link equilibrium. For this purpose, point A is fixed to ground by means of the connection rod $\overline{\text{AB}}$, thus generating a statically determined problem and guaranteeing reaction force R to be aligned with the direction of the rod (in fact, the direct connection of point A to ground would generate a statically indeterminate structure and therefore an undetermined direction of reaction R). Even if the link geometry offers a null arm length to component R_x about the rotation axis, i.e. R_x has no effect in balancing torque T_o, taking care of adjusting $\alpha \approx 0$ prevents reaction R_x to affect the link equilibrium in case of small assembling errors. R_y, which is measurable by the load cell, is the only force affecting the link equilibrium and the output torque T_o is measurable as follows:

$$T_o = bR_y = bF \tag{2.8}$$

where constant b is the arm length of force F.

According to the aim of highlighting the mechanical properties of the proposed system, a basic control scheme is implemented to drive the test-bench in feedforward mode, e.g. without relying on a force/torque feedback, Figure 2.5: The overall scheme with input T_d and outputs T_o and T_p is called "actuation system". T_d is the desired torque tracked by the motor, while torques T_o and T_p have been previously described. The transmission itself is represented by the "RDHT" block and receives the feedforward torque input T_m generated by the motor "M". The motor is powered by the current controller C_I executed by the motor driver and based on the measurement of current draw I_m.Torque reference T_r is defined as the desired torque T_d plus a compensation term T_c used to reduce the effect of the cogging torque produced by the electric motor. The compensation waveform T_c is stored in form of look-up table, "L_c", and evaluated based on the measurement of the motor position θ_m. The look-up table L_c is determined in a separate set of tests via standard practices (see Appendix B for more details).

2.4.2 Test-Bench Details

The main components used to build the experimental test-bench are listed below. A CX51 Beckhoff Embedded-PC based on TwinCAT real-time communication protocol is used for controlling the system; a fixed sampling frequency of 1 kHz is set for all the experiments shown in this

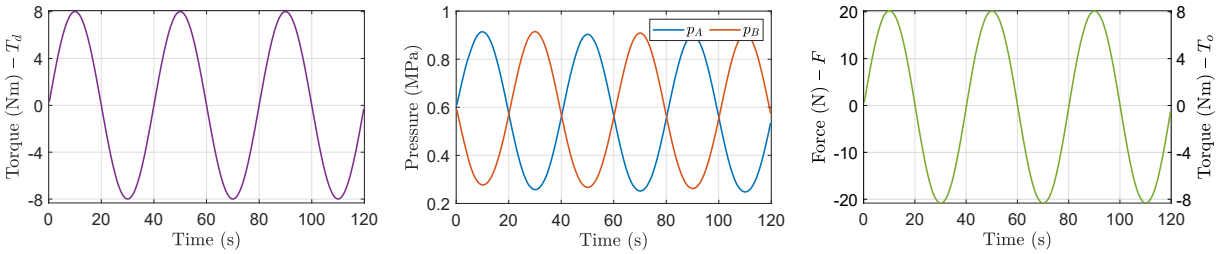

Figure 2.6: Measurement of the relevant quantities during static tests (Fig. 2.4). *Left:* the desired torque T_d is defined in terms of a sinusoidal reference with 8 Nm amplitude and 40 s period. *Center:* measurement of pressures p_A and p_B (the initial pressurization used in this experiment is $p_0 = 0.6$ MPa). *Right:* measurement of the output force F; the measurement is also reported in terms of output torque T_o on the right y-axis by applying (2.8).

chapter. An AKM52L direct-drive motor from Kollmorgen (8.67 Nm rated torque, 19.6 Nm peak torque) is used as input actuator. Input rotation and input torque are measured by means of sensors embedded in the motor driver. Transmission channels are implemented using hydraulic hoses characterised by a 1.5 m length, a 6 mm inner diameter, and a flexible coating of Kevlar fibers. A distance of 1.5 m between actuator and joint is considered sufficient to remotize the actuators of most of robotic arms employed in practical applications. Purified water is used as working fluid and two 3100x pressure sensors from Gems Sensors (with a 16 bar maximum measurable pressure and a 0.04 bar accuracy) measure the fluid pressure. An RM08D01-12 encoder from *RLS* (4096 cpr resolution) measures the output rotation, while a single-point load cell from Tedea Huntleigh (model *1024*, 3 kg capacity) measures the forces applied at the end-effector, located at a distance of $b = 400$ mm from the arm rotation axis.

2.5 Experimental Characterisation

Experiments are conducted in three different sessions. First, static tests (i.e. zero output rotation) validate the working principle presented in Sect. 2.2, analyse the accuracy of the indirect torque measurement through pressure sensing and measure transmission stiffness. In the second session, static and viscous friction are measured. Finally,the transmission transparency is characterized under large displacements and different load conditions.

In static configuration (Fig. 2.4), the motor applies the torque T_m at the transmission input, while the output rotation is prevented by the load cell, which is fixed to ground and measures the exact output torque T_o trough (2.8). A sinusoidal torque reference $T_d = A \sin(wt)$ with large amplitude $A = 8$ Nm and low frequency $\omega = 0.025$ Hz (approximating static working conditions) is imposed, Fig. 2.6 (left). Fig. 2.6 (center) verifies that positive values of commanded torque T_d (or motor torque T_m) increase pressure p_A and decrease pressure p_B with respect to the initial pressure $p_0 = 0.6$ MPa, according to (2.3). Finally, Fig. 2.6 (right) shows the load cell measurement F; this plot can also be interpreted in terms of torque T_o on the right y-axis, showing that transmission transparency guarantees a close matching between desired and output torques.
Fig. 2.7 (left) shows the high accuracy of the indirect torque measurement by means of pressure sensing T_p. Measurements T_p and T_o, which are displayed as function of Δp, are extremely

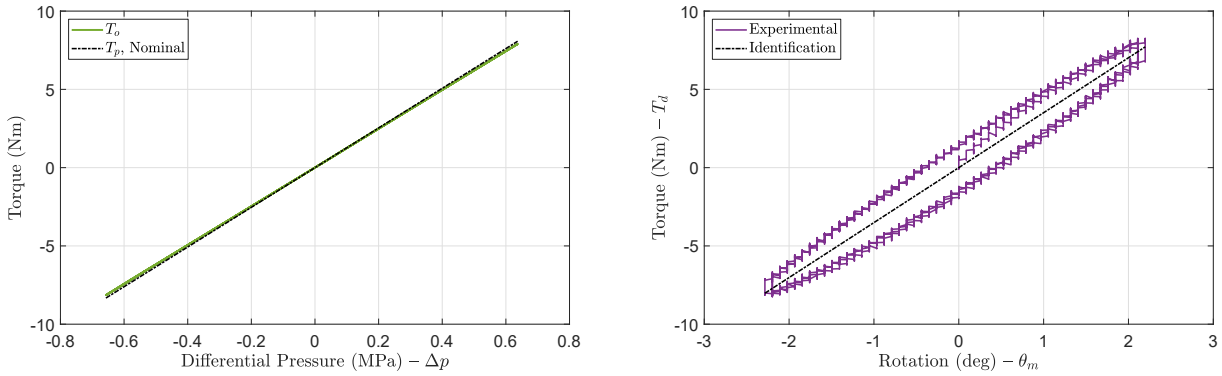

Figure 2.7: Static characterisation. *Left:* comparison of the output torque measurement by means of the load cell T_o and by means of pressure sensors T_p. *Right:* stiffness measurement.

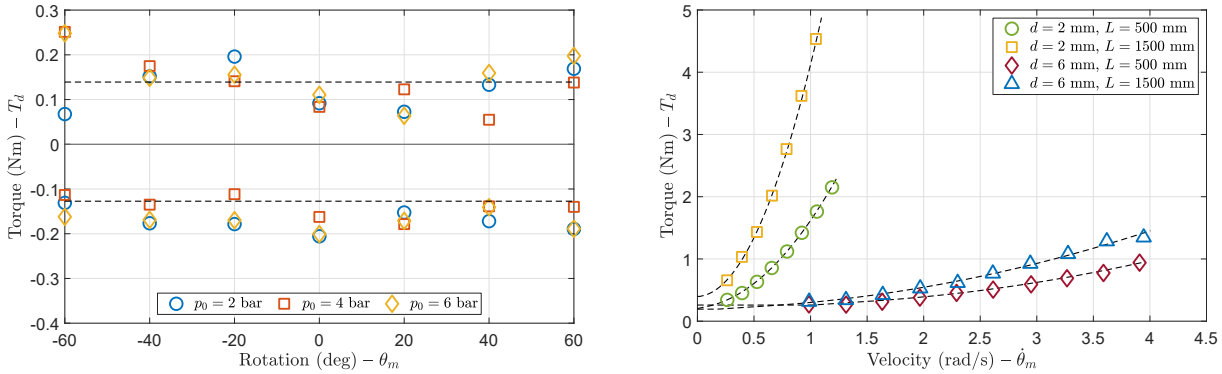

Figure 2.8: Static and viscous friction characterisation. *Left:* Static friction of the complete actuation system measured at different angular positions and pressurization levels (colored markers); the black dashed lines represent the static friction of the motor alone. *Right:* viscous forces measurements performed with different inner diameter d and length L of the hoses. Coloured markers represent the measurements and the black dashed lines represent quadratic fittings of the data.

close over the entire range of the experimental operating conditions. Moreover, the relationship between output torque T_o and differential pressure Δp is confirmed linear. The analysis will be extended to the dynamic domain in Chapter 3, and a closed-loop torque control will be designed exploiting T_p feedback.

Transmission stiffness is characterized in Fig. 2.7 (right): a value of 200 Nm/rad (3.51 Nm/deg) is measured. This is a promising result considering that the distance between the motor and the robot joint is 1.5 m; indeed, high transmission stiffness is critical to achieve large control bandwidth in closed loop when the torque measurement takes place in distal position, allowing large control gains without provoking robot instability (see Appendix A).

In the second set of tests, the output link is removed and the output joint is set free to rotate; this configuration is used to characterise static and viscous friction. The measurement of static friction is shown in Fig. 2.8 (left). A feedforward torque ramp with low slope T_d is commanded to the motor, while rotation θ_o is measured at the output side; static friction (colored marks in the picture) is defined as the minimum torque T_d needed to detect a rotation of 0.5 deg at the output joint. This experiment, performed in positive and negative directions, is repeated at

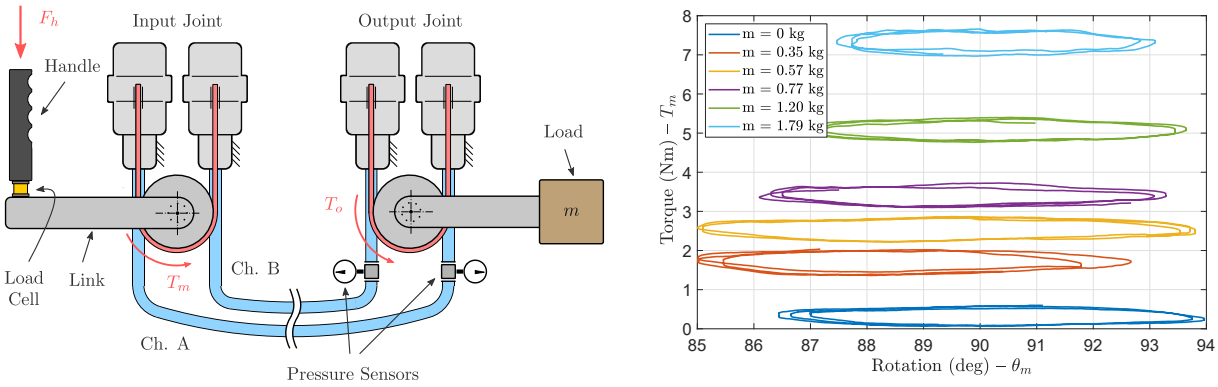

Figure 2.9: *Left:* Scheme of the experimental test-bench used for manually operate the transmission by means of the sensorized input handle. Different load levels can be settled by modifying the external mass m. *Right:* measurement of the user effort, i.e. input torque T_m, to move the transmission input along a reference periodic trajectory with an amplitude of $\approx 5°$ at different load levels.

different angular positions and different pressurization levels. Results reveal that static friction is reasonably independent of the pressurization level and rather uniform over the entire range of motion, with an average value of 0.15 Nm and a maximum value of 0.24 Nm. As a relevant result, the maximum value of static friction detected during experiments is 0.96% of the maximum rated torque of the transmission (25 Nm). Moreover, the static friction of the entire actuation system is comparable to the friction level measured while repeating the test using the electric motor alone (black dashed lines), meaning that the frictional contribution attributed to the transmission is small.

Viscous friction is measured in Fig. 2.8 (right). The output joint is again free to rotate and the motor is position-controlled along constant velocity trajectories with velocities in the range of 0.2–4 rad/s. Experiments analyse the influence of hoses inner diameter d and length L. First, results show that the selection of small hose diameter generates high viscous losses; viscous friction generated for $d = 2$ mm is higher by about one order of magnitude than friction generated for $d = 6$ mm; selecting large hose diameters is preferable. Moreover, the dependence of viscous forces on the hose length L reveals weaker at large hose diameter d, meaning that, most probably, forces are mainly generated by concentrated losses at those flow regimes. In contrast, the distributed losses become more relevant at small hose diameter d, resulting in a stronger dependence of the viscous force on the hose length L. Experiments are repeated at different pressurization levels, however results are not shown because, as expected from theory, fluid incompressibility makes viscous forces independent of the pressurization level.

Finally, one last experiment is performed by disconnecting the electric motor in order to highlight the pure transmission response, preventing measurements to be affected by motor characteristics, such as friction or residual cogging torque. In this configuration, depicted in Fig. 2.9 (left), a second link, equipped with a sensorized handle, is connected at the input side to allow the user to manually operate the transmission. The user imposes slow sinusoidal trajectories with amplitude of $\approx 5°$, while the load cell placed below the handle measures the force applied by the user hand F_h. Velocities are in the range ± 0.2 rad/s. The test is repeated several times for different loading levels by modifying the external mass m from 0 kg to 1.8 kg. Fig. 2.9 (right) shows the measurement of the input torque T_m ($= bF_h$) with respect to link

rotation θ_m: a maximum damping torque of 0.27 ± 0.08 Nm is perceived at the user hand (corresponding to a force of 0.675 ± 0.2 N), with an overall behaviour rather independent of the applied load. This test proves that the response of the floating-bonnet cylinders is independent of the different levels of internal pressure that external loads induce: therefore external loads do not affect the transmission transparency. RDHTs solve the common problem of many existing transmission systems where internal friction depends on the external load, which determines modeling and control complexity. In bowden-cable transmissions, for example, the axial force generated on the steel cables to transmit torques determines how much the cable is pushed against its polymeric sheath, thus creating a dependence between transmitted forces and internal friction.

2.6 Discussion

This chapter presented the design and the experimental characterisation of a **R**olling **D**iaphragm **H**ydrostatic **T**ransmission (RDHT) for robot actuation based on novel low-friction floating-bonnet cylinders. The transmission enables the remote positioning of direct drive electric motors away from the robotic arm, generating a highly-dynamical, lightweight structure with additional features of excellent efficiency and virtually-zero static friction. An accurate design process laid the foundation for the development of a new generation of remotely-actuated robots. The proposed design brings together a number of positive attributes, such as low mass, high specific torque and power, ease in control, absence of leakages, absence of backlash, lubricant-free (water can be used as working fluid) and wear-free operation, undemanding manufacturing tolerances. Moreover the resulting system is low-cost. An integrated robotic joint was developed and the overall transmission system was tested. Each joint provide a rotation range of $140°$ and a maximum rated torque of 25 Nm, meeting the minimum requirements of rehabilitation exoskeletons, collaborative robots and similar lightweight robotic applications. Moreover, an extremely low static friction level of 0.24 Nm was measured (0.96% of the maximum rated torque), and the properties of torque reflection proved uniform over the entire range of motion and independent of the applied load, which is not the case of many common cable-based transmission systems. These results prove hydrostatic transmissions suitable for developing many applications. Generating lightweight structures and overcoming velocity and backdrivability limitations of standard highly geared actuators enable the design of a novel generation of robots that exceeds productivity and manipulation capabilities of industrial manipulators, while providing interaction features comparable to those of co-bots, yet without requiring the use of sophisticated force sensors. RDHTs could also simplify the design of robotic arms with very large workspaces. Finally, the design of exoskeletons is another promising application. The high specific torque of each joint allows the design of compact, ergonomic and lightweight devices capable of supporting users' arms and legs; the accurate torque generation would produce enhanced torque rendering for remote manipulation or rehabilitation. Compared to other existing cable-based solutions, hydrostatic transmissions are not integrated in the structure design and the length of the links can be easily adapted to different users. Moreover the low-cost feature would contribute to spread the robotic rehabilitation therapy.

Chapter 3

Smith-predictor-based torque control

3.1 Overview

This chapter proposes a novel torque-control strategy for hydrosatic transmissions based on pressure measurement feedback. Among many strong potentials of **R**olling **D**iaphragm **H**ydrostatic **T**ransmissions (RDHTs), a rather unexplored path is their use for the actuation of high-bandwidth human-robot interaction (HRI). Indeed, existing HRI approaches mostly rely on standard robotic technologies combined with cautious impedance control laws conservatively guaranteeing stability for any contact condition (see, e.g., [65–67] and references therein). A first step towards this end is certainly to investigate the currently unexplored challenge of providing a high-bandwidth non-oscillatory torque response despite the underdamped oscillatory behavior typically generated by the low friction RDHT devices. This goal inevitably requires some form of feedback control loop to artificially inject damping in the actuator dynamics. Feedback control has been used to this end in [68] when using Series-Elastic Actuators (SEA), which also offer an intrinsic compliant behavior. The corresponding control solutions, however, when applied to RDHT systems, whose dynamics is quite different due to the presence of fluid lines, revealed to be experimentally less effective than the Smith-predictor-based solution proposed in this chapter. An appealing feature of the RDHT architecture, already mentioned in [47], is that the torque feedback measurement can be conveniently implemented by a differential pressure measurement on the fluid lines, a cost-effective paradigm validated experimentally in [53]. The measurement positioning along the fluid lines poses an interesting trade-off between accuracy and stabilizability wherein a proximal placement, closer to the actuator (colocation), is more stable but less accurate, and a distal placement is more accurate but exhibits increased dynamical effects. This chapter reaches beyond the preliminary results of [53] by exploiting the high-performance RDHT device developed in Chapter 2, which is an ideal testbed not only for validating the high-bandwidth high-transparency RDHT torque transmission paradigm, but also for investigating the maximum performance limits that one can reasonably expect from RDHTs. The considerably low friction characterizing the experimental device poses nontrivial control design challenges, because of the highly oscillatory open-loop response. The proposed techniques apply to general low-friction RDHT architectures.

The contributions of this chapter are listed next: Sect. 3.2 confirms the high accuracy of the torque feedback based on distal pressure measurement by using an extra ground truth load-cell sensor for validation purposes. Sect. 3.3, through extensive experimentation with different

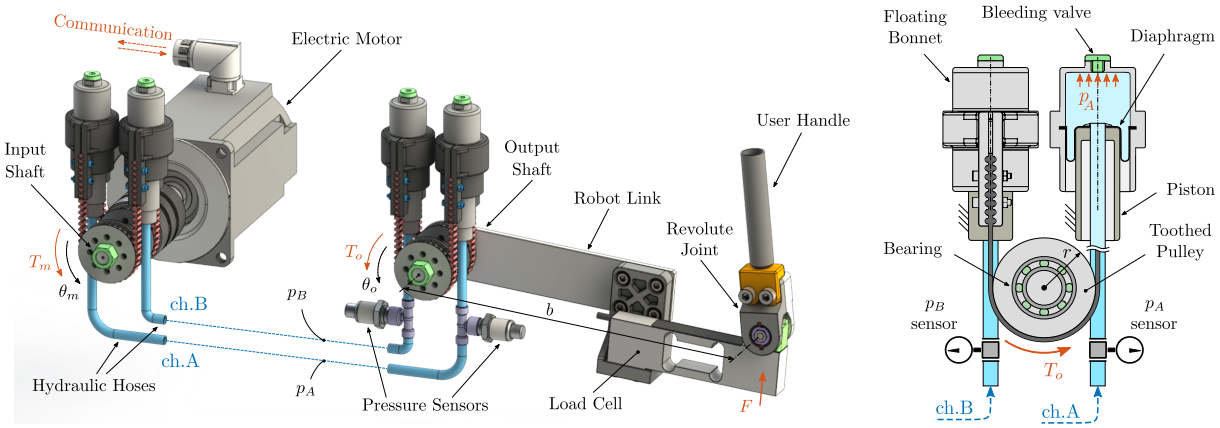

Figure 3.1: Rolling diaphragm hydrostatic transmission. *Left*: setup allowing the human user to interact with the actuation system through the handle; alternatively, the handle can be removed and the load cell fixed to the ground. *Right*: scheme of the working principle of the output joint.

hose lengths, describes the characterisation the dynamic response of the open-loop transmission, along with a linearity analysis. A parametric linear dynamical model for the open-loop system is proposed and identified for all of the considered hose lengths, comprising a combination of a second-order underdamped response and a time delay, and achieving a desirable trade-off between complexity and accuracy (alternative existing models, for example, comprise a larger number of states [53]). Sect. 3.4 proposes and experimentally validates a parametric feedback control design strategy based on a Smith-predictor [69] together with a dynamic controller automatically tuned to achieve arbitrary user selected closed-loop natural frequency and damping ratio; the closed loop then reaches almost the same natural frequency as the open-loop plant, in spite of the large amount of artificial damping introduced by the control scheme. Finally, Sect. 3.5 provides an encouraging preliminary illustration of the advantages arising from the proposed controlled torque transmission device in human robot interaction by simple tasks performed by a human operator.

3.2 Hydrostatic Transmission

3.2.1 Experimental Test-Bench

Based on the test-bench developed in the Chapter 2, Fig. 3.1 (left) shows the experimental RDHT actuation system used in this chapter to develop and test the pressure-based closed-loop control. The electric motor on the left, connected to the input shaft of the transmission, provides the actuation torque T_m. Two hydraulic hoses (channels A and B) couple the rotation of input and output shafts. Two pressure sensors are placed at the end of the hoses, close to the output shaft, where a robot link is connected. A load cell is located at the end of the link to measure the actual force F exchanged between the actuation mechanism and an external element, possibly comprising interactions with the surrounding environment or with a user holding the handle; the actual output torque $T_o = bF$ is calculated accordingly. The measurement output of the pressure sensors is regarded as a low-cost indirect torque measurement, and is used in this work for identification and feedback purposes. On the other hand, the more sophisticated load

cell is the ground truth measurement providing the exact delivered output torque.
Fig. 3.1 (right) details how the pressure-torque transformation takes place at the output end of the transmission (the same transformation occurs at the input side). Two cylinders are coupled in an antagonistic configuration by the timing belt routed around the output toothed pulley. The cylinders apply a force proportional to their internal pressure on their respective belt branches: when the two pressures (denoted by p_A and p_B) coincide, the two cylinders are balanced and no torque is generated on the pulley; when the two pressures are different, the cylinders are no longer balanced, and thus a net torque T_p is generated according to the algebraic relation

$$T_p = A_e r \Delta p, \tag{3.1}$$

where constant A_e is the effective area of the cylinders, constant r is the pulley radius, and variable $\Delta p = p_A - p_B$ is the pressure difference between channels A and B. Since the elements connecting the cylinders and the pulley (i.e. the membrane, belts and bearings) are a source of reasonably low friction and hysteresis, then the torque acting on the robot arm can be approximated to be the same as the torque associated with the pressure difference, namely $T_o \approx T_p$. The accuracy of this assumption decays at high velocities because of viscous and resonant effects.
Refer to Sect. 2.4.2 for details about commercial components used to implement the test-bench.

3.2.2 Goal: Pressure-Feedback Torque Control

The objective of Chapter 3 is here explained; a linear model for the transmission system and a novel torque setpoint stabilization control law, using a distal pressure measurement feedback signal along the fluid transmission, are proposed.
Pursuing high-quality interaction, the higher-accuracy lower-stability collocation of pressure sensors close to the output joint is chosen, instead of the less desirable results that can be achieved exploiting a proximal sensors placement [53]; the challenge is therefore obtaining large torque-bandwidth while guaranteeing stability. The long term purpose of our research activity is the design of a simple and versatile control architecture for human-machine interaction. As a first step towards this end, this chapter focuses on stabilizing a force setpoint for the end-effector. The control design requirements can be summarized as follows:

- Ensure stable closed-loop force setpoint regulation;
- Achieve a low steady-state error;
- Provide a sufficiently damped transient response;
- Provide a large closed-loop bandwidth.

Referring again to the scheme in Fig. 3.1, the feedback controller should compensate for the disturbances acting “before” the pressure sensing point, such as the viscous friction distributed along the fluid channels, the internal friction of the electrical motor and of the input shaft bearings, the hysteresis of the input membranes, and the motor torque ripple. On the other hand, disturbances injected “after” the sensing point cannot be compensated for. For this reason, the floating-bonnet layout of the cylinders used in Chapter 2 is an ideal solution due to the minimal

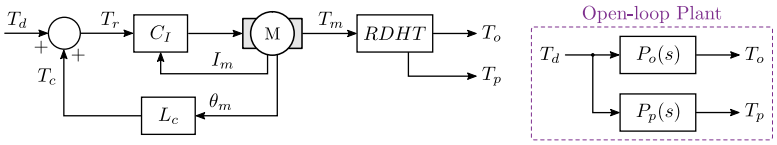

Figure 3.2: Scheme of the open-loop plant and its equivalent frequency-domain model.

friction losses, thereby minimizing these downstream disturbances: a fact that is confirmed in the experimental results of Sect. 3.5.
As a final remark, the force control law is designed under a *worst-case* condition (from the stability viewpoint), represented by clamping the end effector at a fixed position, so as to interact with an infinitely stiff environment [70]. The designed control law is subsequently tested in a scenario where a human operator interacts with the transmission end-effector through a handle; enhanced actuation features of the closed-loop system can be proved in a real-life application scenario.
All the open-loop and closed-loop experiments shown in this chapter are performed with a fixed sampling frequency of 1 kHz.

3.3 Modeling and Identification

With reference to Fig. 3.2, the overall dynamical system standing between the desired torque signal T_d and output measurements T_p and T_o, is called *open loop*; the first output T_p is obtained from the pressure sensors, and the second one, T_o, obtained from the load cell. A transfer function is associated to each output, namely $P_p(s)$ from T_d to T_p (involved in the control design) and $P_o(s)$ from T_d to T_o (used as ground truth validation). Fig. 3.2 shows that the open loop not only pertains to the hardware itself (the motor "M" and the transmission "$RDHT$"), but also includes the current controller C_I executed by the motor driver and a feedback compensation term T_c used to reduce the effect of the cogging torque produced by the electric motor. The cogging-torque compensation waveform T_c is stored as a look-up table, "L_c", and evaluated based on the measured motor angle θ_m (see Appendix B for more details).

This section presents the experimental characterisation of the open-loop transfer functions $P_p(s)$ and $P_o(s)$, and the identification of $P_p(s)$, used as a starting point to design a model-based torque controller in Sect. 3.4. The experiments are repeated for three different lengths L of the hydraulic hoses, since the influence of the hose lengths is a key parameter when the proposed architecture is employed to relocate the actuators of different joints in a robotic system, from those close to the robot base to those placed at distant links. A linearity analysis is also presented.

3.3.1 Open-loop Characterisation

The identification experiments are performed by clamping the output link to the ground by means of the load cell located at the end effector (the output handle shown in Fig. 3.1 is removed in this case). For this test, the input signal T_d is selected as a linear chirp with frequency ranging from 0 to 100 Hz, while the responses of two outputs, T_p and T_o, are simultaneously acquired.

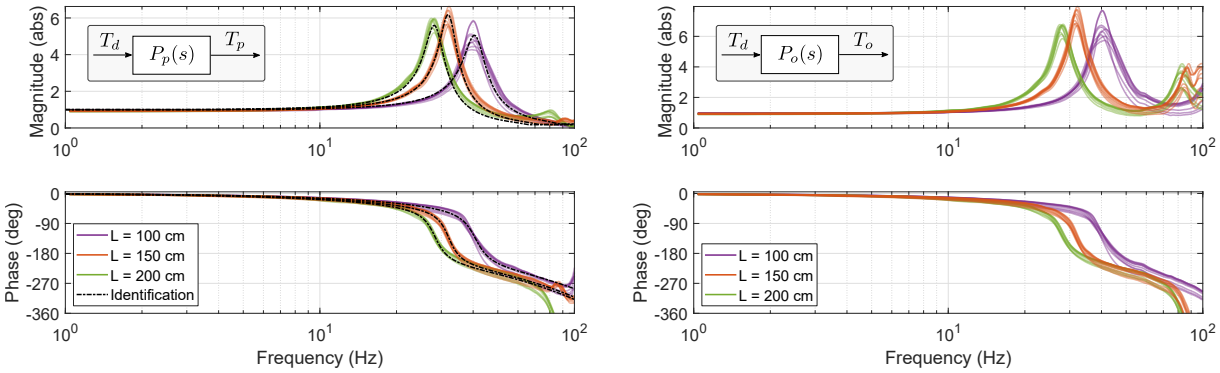

Figure 3.3: Experimental frequency responses of the open-loop plant. *Left*: transfer function $P_p(s)$ from T_d to T_p. *Right*: transfer function $P_o(s)$ from T_d to T_o. The experiments are performed using 3 different lengths of the hydraulic hoses ($L = 100, 150, 200$ cm). Each color represents a family of linearity experiments, where the test is repeated by setting different values for the input bias (0, 0.5 and 1 Nm) and amplitude (0.35, 0.5 and 0.75 Nm). The dashed-dotted black lines in the left plot represent the identified transfer functions for each one of the considered configurations.

Fig. 3.3 shows the experimental open-loop transfer functions $P_p(s)$ and $P_o(s)$, collected for three different lengths of the hydraulic hoses, namely $L = 100$ cm (in purple), $L = 150$ cm (in red), and $L = 200$ cm (in green). The colored curves actually represent a family of experiments, where the identification test has been repeated by setting different values for the input bias (0, 0.5 and 1 Nm) and amplitude (0.35, 0.5 and 0.75 Nm).

The resulting curves confirm the linearity of the dynamics for both measurement outputs. The magnitude of both transfer functions is well placed around 1 in the range 0–10 Hz, thereby showing good correspondence between the desired torque T_d (the input) and the delivered torque T_p or T_o (the outputs). Above 10 Hz, the dynamic transparency of the transmission is degraded by the first resonance peak, located in the range 25–40 Hz, depending on the hose lengths. As the length L increases, some compliance (mainly due to distributed deformation of the hoses wall) emerges, and the resonance peak takes place at lower frequencies. Since the mechanical dissipative effects are minimized through the adoption of low-friction floating-bonnets, the resonance peak is only lightly damped. A second resonance peak is also visible by the load cell, $P_o(s)$, above 80 Hz, which is hardly visible from the pressure sensors measurement. Looking at the phases of the red and green curves, it seems that the location of the pressure sensor plays a role (perhaps from a zero-pole cancellation) for the absence of this peak in $P_p(s)$, probably due to further dynamic effects taking place between the pressure sensors and the load cell. Since these high frequency peaks are hardly observable from the pressure sensors, they will affect the high-frequency output performance without being involved in the closed-loop stability considerations.

Finally, it is possible to observe that both phase plots exhibit the typical exponential shape (a linear shape in logarithmic scale) characterizing a pure time-delay phenomenon, which should be taken into account in the considered dynamical model. The source of this time delay, discussed in the next section, is a combination of software processing/sampling effects and possible unmodelled high-frequency dynamics. Moreover, the phase plot of $P_p(s)$ and $P_o(s)$ have similar values, testifying that the same time delay affects both the pressure and the load-cell outputs.

3.3.2 Dynamics Parameters Identification

The analysis carried out in the previous section suggests that a linear second-order model with unit gain and a pure time-delay τ can appropriately describe the plant $P_p(s)$. In particular, the reference model

$$P_p(s) = P_p^0(s)e^{-\tau s} = \frac{\omega^2}{s^2 + 2\xi\omega s + \omega^2}e^{-\tau s} \tag{3.2}$$

is selected, where $P_p^0(s)$ is a delay-free second order dynamics and $e^{-\tau s}$ provides the pure time-delay component. The parameters in (3.2) can be identified via standard practices, by minimizing the standard deviation of the difference between the experimental data and the analytical model in the frequency domain. The dashed black lines in Fig. 3.3 show the response of the identified model (3.2) for each one of the three considered hose lengths. The identified parameters are reported in Tab. 3.1. These parameters, which well match the experimental data in all of the analyzed configurations, appear to be acceptable given the low damping of the system and the value of time delay, which increases with the length of the hoses. Tab. 3.1 suggests that the time delay is composed of a constant software contribution and a physical component stemming from the unmodelled and/or high-frequency dynamic effects. To avoid overloading the presentation, the next sections focus on the configuration corresponding to $L = 150$ cm because the other ones, with the corresponding identified parameters from Tab. 3.1, lead to analogous results.

Table 3.1: Dynamical Parameters Identification.

Configuration	ω (Hz)	ξ (-)	τ (ms)
$L = 100$ cm	40.86	0.0994	3.10
$L = 150$ cm	32.02	0.0831	3.75
$L = 200$ cm	28.35	0.0898	3.94

3.4 Torque control

3.4.1 Controller design

To achieve the design goals summarized in Sect. 3.2.2, the Smith-predictor-based control scheme represented in Fig. 3.4 is adopted. The open-loop plant (or simply "Plant" as indicated in the figure), is the transfer function $P_p(s)$ modeled in Sect. 3.3 as a cascade connection of $P_p^0(s)$ and $e^{-\tau s}$, according to (3.2). In order to deal with the time delay, we first select a feedback controller $C(s)$ designed by only focusing on the delay-free transfer function $P_p^0(s)$, and then augment the

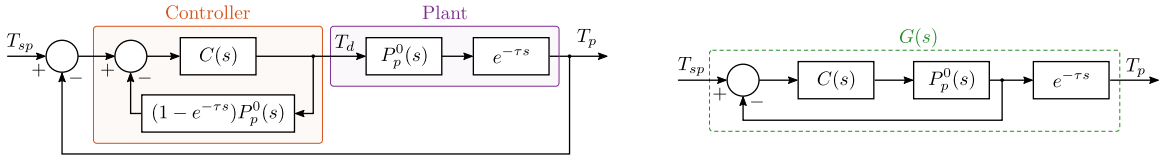

Figure 3.4: Closed-loop torque control scheme. *Left*: actual Smith-predictor-based control scheme. *Right*: equivalent closed-loop block diagram.

scheme with a classical Smith predictor [69], corresponding to the incremental transfer function $(1 - e^{-\tau s})\, P_p^0(s)$. The overall scheme is well represented in Fig. 3.4 (left) and corresponds to the control law

$$T_d(s) = \frac{C(s)}{1 + C(s)\,(1 - e^{-\tau s})\, P_p^0(s)} (T_{\mathsf{sp}}(s) - T_p(s)), \tag{3.3}$$

where $T_{\mathsf{sp}}(s)$ denotes the torque setpoint, and the input to the controller is the setpoint regulation error $T_{\mathsf{sp}}(s) - T_p(s)$. Due to the special structure of the Smith predictor, the block diagram in Fig. 3.4 (left) can be proved to be equivalent to the one in Fig. 3.4 (right). As a result of the Smith predictor, the time delay τ is removed from the feedback loop and does not play any role in the stability analysis, thereby greatly simplifying the stability and performance-oriented control design. The equivalent closed-loop transfer function from the closed-loop setpoint reference $T_{\mathsf{sp}}(s)$ to the measurement output $T_p(s)$, denoted as $G(s)$, can be computed as follows:

$$G(s) = \frac{T_d(s)}{T_{\mathsf{sp}}(s)} = \frac{P_p^0(s)C(s)}{1 + P_p^0(s)C(s)} e^{-\tau s}. \tag{3.4}$$

The closed-loop transfer function (3.4), clearly indicates that $C(s)$ can be designed depending on $P_p^0(s)$ only, without needing to account for the time delay.
The particular structure of $P_p^0(s)$ in (3.2) suggests a possible candidate $C(s)$ in the form of a filtered PID, as follows:

$$C(s) = k_p + \frac{k_i}{s} + \frac{k_d s}{T_f s + 1}. \tag{3.5}$$

The low-pass filter time constant T_f is introduced to reduce the noise amplification effects of the derivative action, and is considered as a free design parameter alongside gains k_p, k_i, and k_d. For mathematical convenience, (3.5) is rewritten in the following alternative form:

$$C(s) = \frac{\bar{k}_d s^2 + \bar{k}_p s + \bar{k}_i}{s\,(T_f s + 1)} = \bar{k}_d \frac{s^2 + \frac{\bar{k}_p}{\bar{k}_d} s + \frac{\bar{k}_i}{\bar{k}_d}}{s\,(T_f s + 1)}, \tag{3.6}$$

with $\bar{k}_p = k_p + k_i T_f$, $\bar{k}_i = k_i$, and $\bar{k}_d = k_d + k_p T_f$. These three gains can be conveniently selected to ensure a cancellation between the denominator of $P_p^0(s)$ in (3.2) and the numerator of the right expression in (3.6). Then, by choosing all the coefficients as

$$\bar{k}_p = \frac{\xi \omega_t}{\xi_t \omega},\ \bar{k}_i = \frac{\omega_t}{2\xi_t},\ \bar{k}_d = \frac{\omega_t}{2\xi_t \omega^2},\ T_f = \frac{1}{2\xi_t \omega_t}, \tag{3.7}$$

where ξ_t and ω_t are free design parameters (the "target" parameters), the fourth order closed-loop transfer function in (3.4) exhibits stable zero-pole cancellations and corresponds to

$$G(s) = G_t(s) = \frac{\omega_t^2}{s^2 + 2\xi_t \omega_t s + \omega_t^2} e^{-\tau s}, \tag{3.8}$$

which is appealing from the tuning viewpoint. Indeed, with this controller selection, the closed-loop system behaves like a delayed second order transfer function with unitary static gain. The resulting natural frequency ω_t and damping coefficient ξ_t can be freely chosen by the designer, while the delay τ coincides with the open-loop one.

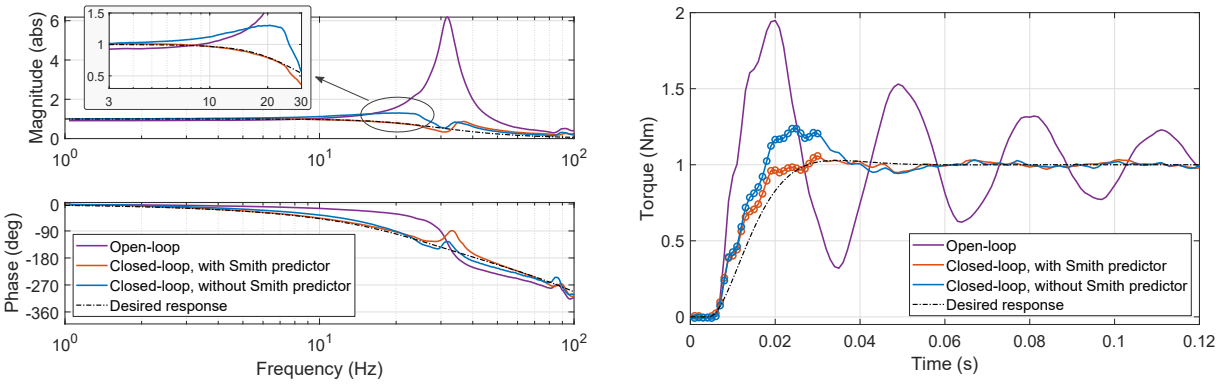

Figure 3.5: Effect of the Smith Predictor. The purple line corresponds to the open-loop response; the blue and the red lines correspond to the closed-loop system, but only in the second case the filtered PID controller is augmented with the Smith predictor architecture; the dashed-dotted black line is the target closed-loop response $G_t(s)$ in (3.8). *Left*: frequency response from setpoint torque T_{sp} to the measurement T_p (from T_d to T_p in the open-loop case). *Right*: step response of torque T_p measured by the pressure sensors; the circles show the first 30 samples after the step command was executed.

3.4.2 Torque Control Experiments

This section assesses the effectiveness of the proposed control architecture by testing the closed-loop torque-control response $G(s)$, corresponding to (3.4), which simplifies to (3.8) due to the special selection of the PID controller parameters (3.7) leading to a stable zero-pole cancellation. The controller tuning examined in this section corresponds to the design parameters selection $\xi_t = \sqrt{2}/2 \approx 0.7$, critically damped, and $\omega_t = 25$ Hz (resulting in controller parameters: $\bar{k}_p = 0.0918$, $\bar{k}_i = 111.07$, $\bar{k}_d = 0.0027$, $T_f = 0.0045$). The critical damping value provides a theoretical overshoot of 4%, a phase margin of 65 degrees, and no resonance, thus it is particularly attractive for the achievement of the specifications reported in Sect. 3.2.2.

In this set of experiments the output link is again fixed to the ground by means of the load cell (same experimental configuration used for the identification of Sect. 3.3.1). Fig. 3.5 shows the closed-loop frequency response (left) and step response (right). The target response, $G_t(s)$ in (3.8), is represented by dashed-dotted black lines in both plots. The experimental responses are generated both with (solid red line) and without (solid blue line) the Smith predictor (the latter architecture considers only $C(s)$ as the feedback controller, according to Fig. 3.4 (top)). By comparing the plots, the effectiveness of our PID tuning and the benefits provided by the Smith predictor architecture can be readily observed; the resonance peak is effectively attenuated, and a close match between the target and the experimental frequency responses is achieved up to 25 Hz, Fig. 3.5 (left). The frequency response also shows that some mismatch occurs in the zero-pole cancellation strategy, which testify that some accuracy limitations of the linear model arise around the resonance, possibly due to some nonlinear and unmodeled dynamics. Additionally, the step responses in Fig. 3.5 (right) illustrate the improvement obtained by the feedback action , as compared to the oscillatory open-loop response. Note also that, as predicted by (3.8), the open-loop and closed-loop responses have the same time delay with respect to the initial instant $t = 0$ s of the step.

Finally, Figs. 3.6 and 3.7 show that the proposed control architecture allows shaping a large variety of target closed-loop transfer functions $G_t(s)$ in (3.8). In particular, parameter ω_t, related to the closed-loop bandwidth, can be increased from low values up to values approaching the

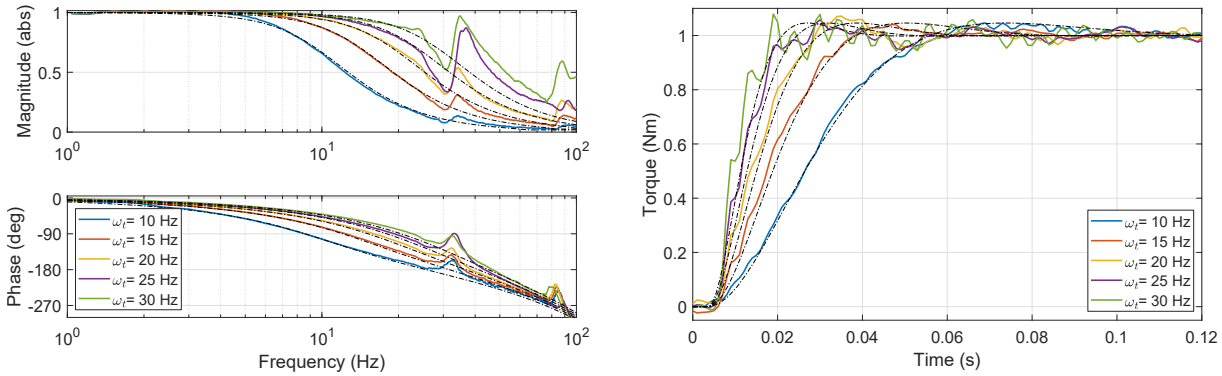

Figure 3.6: Closed-loop response for different choices of parameter ω_t in the range $10 - 30$ Hz and fixed damping coefficient $\xi_t = \sqrt{2}/2 \approx 0.7$. Dashed-dotted black lines represent the target responses corresponding to $G_t(s)$ in (3.8). *Left*: frequency response. *Right*: step response.

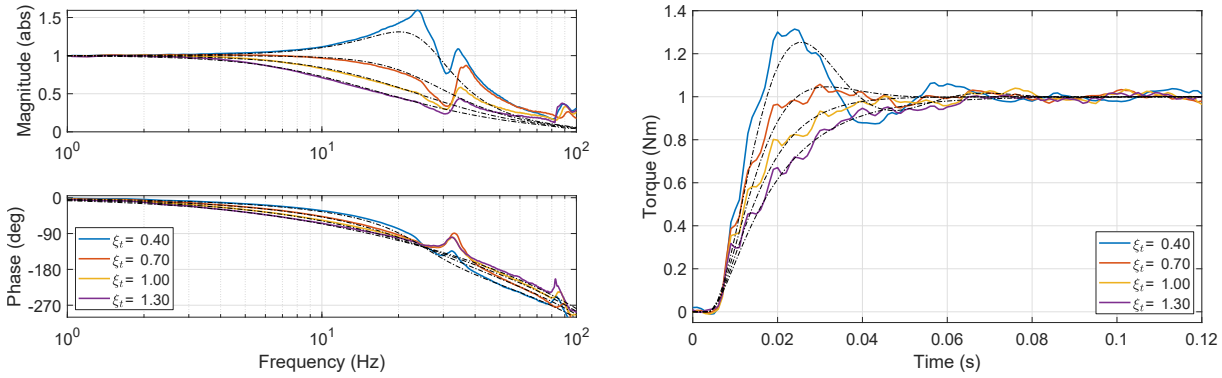

Figure 3.7: Closed-loop response for different choices of parameter ξ_t in the range $0.4 - 1.3$ and fixed natural frequency $\omega_t = 25$ Hz. Dashed-dotted black lines represent the target responses corresponding to $G_t(s)$ in (3.8). *Left*: frequency response. *Right*: step response.

natural frequency of the plant $P_p(s)$ (despite the significant artificial damping injected to remove the undesired open-loop oscillations). Even if the closed loop remains stable for $\omega_t = 30$ Hz in Fig. 3.6, some vibrations occur, so we can reasonably regard $\omega_t = 25$ Hz as the maximum achievable closed-loop natural frequency. Fig. 3.7 shows that the damping ratio ξ_t can also be easily adjusted to reduce the lightly damped open-loop response, ranging from under-damped to over-damped. Each selection produces an experimental response close to the target one given by (3.8) (dashed-dotted black lines).

3.5 Human-Robot-Interaction

As a first step towards control of interacting hydrostatic transmissions, the proposed force controller ($\xi_t = \sqrt{2}/2$, $\omega_t = 25$ Hz) is evaluated in an experimental human-robot-interaction setting. In this case, the output link is free to move, while the user interacts with the system via the handle located at the end-effector.

The first experiment, shown in Fig. 3.8, investigates how the interaction with the human user affects the frequency response of the controller designed under the condition of nominal inter-

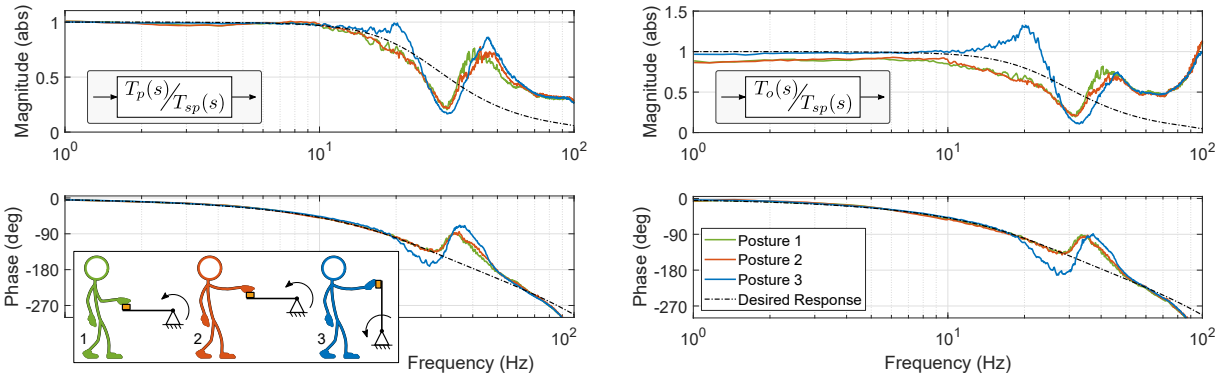

Figure 3.8: Closed-loop frequency response in case of interaction with a human user. Different postures of the user body are considered: In posture 1 (green) the user elbow is bent and the forearm is parallel to the robot link; in posture 2 (red) the user arm is straight and parallel to the robot link; in posture 3 (blue) the user arm is straight and perpendicular to the robot link.

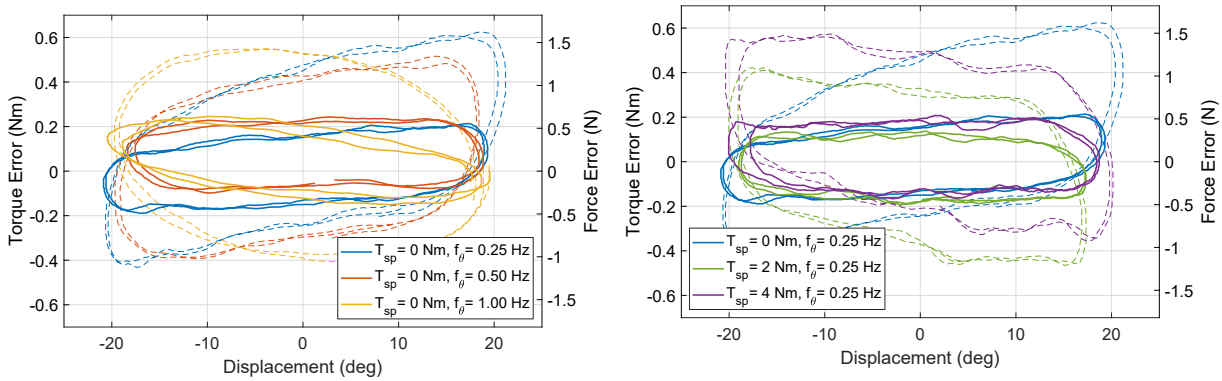

Figure 3.9: Backdrivability test. Torque error $T_o - T_{\text{sp}}$ measured by the load cell with a sinusoidal displacement of the output link with amplitude $20°$, and different displacement frequency f_θ and torque setpoint T_{sp} values. Closed-loop (solid lines) and open-loop (dashed lines) tests are compared.

action with a rigid environment. A linear chirp setpoint T_{sp} with frequency sweeping from 0 to 100 Hz and an amplitude of 0.5 Nm was used as the set-point for the control system, while the user held the output handle in a fixed position. Several postures of the human body were considered in order to range over a variety of impedance values that the human body may produce. As a result, the tracking of the pressure reference is almost unaffected by the presence of the human body (left plot), and the overall plant remains stable even in the presence of the output impedance variation. The tests involving postures 1 and 2 reveal that, despite the accurate pressure tracking, the torque measured at the interaction point has a lower amplitude than expected, i.e. $|P_o(s)| < 1$ over the entire low-frequency domain. This effect can be justified by noticing that the displacement at the output is no longer negligible due to the compliance of the human arm, and therefore larger friction sources located between the pressure sensing point and the robot link induce $|T_o| < |T_p|$, as discussed at the end of Section 3.2.2. In posture 3 the operator arm offers a stiffer constraint to the robot arm motion, thus, a smaller displacement takes place and, consequently, a better matching between T_p and T_o is achieved, i.e. $|P_o(s)| \approx 1$. This posture, however, slightly interferes with the resonance attenuation as confirmed by repeated experiments.

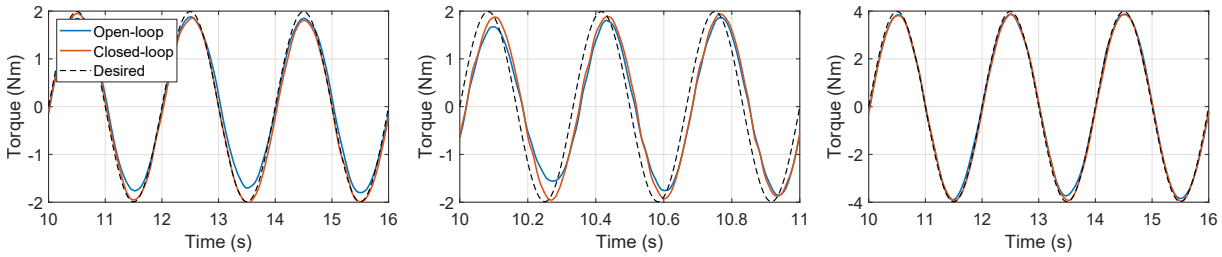

Figure 3.10: Measurement of output T_o in sinusoidal torque-setpoint $T_{\text{sp}} = A_{\text{sp}} \sin(f_{\text{sp}} t)$ tracking tests. The robot link is held in a fixed position $\theta_o = 0°$ by the user. The response of open-loop (blue line) and closed-loop (red line) tests are compared. *Left*: setpoint amplitude $A_{\text{sp}} = 2$ Nm, setpoint frequency $f_{\text{sp}} = 0.5$ Hz. *Center*: increased setpoint frequency, $f_{\text{sp}} = 3$ Hz. *Right*: increased setpoint amplitude, $A_{\text{sp}} = 4$ Nm.

The closed-loop low-frequency behavior is further investigated in the next set of experiments. Backdrivability tests were performed by imposing constant torque setpoints, while the user freely moved the output handle on an oscillatory trajectory of amplitude $\approx 20°$. Fig. 3.9 shows the evolution of the output torque error $T_o - T_{\text{sp}}$ (as measured by the ground truth load cell) as a function of the displacement angle in two scenarios. At the left, the setpoint $T_{\text{sp}} = 0$ Nm is associated with different displacement frequencies, specifically $f_\theta = 0.25, 0.5$ and 1 Hz. At the right, different torque setpoints $T_{\text{sp}} = 0, 2$ and 4 Nm are associated with the frequency $f_\theta = 0.25$ Hz (so that the blue curves coincide). The two figures report both the open-loop (dashed lines) and the closed-loop (solid lines) responses. In all of the considered cases, the control system reduces the maximum value of the torque needed to backdrive the system (namely, the torque error) in the range of ± 0.2 Nm, thus reducing it by a factor of ≈ 3 as compared to the open loop. The y-axis scale on the right of both figures reports the corresponding force error at the user hand.

Finally, Fig. 3.10 assesses the tracking of a sinusoidal torque setpoint $T_{sp} = A_{\text{sp}} \sin(f_{\text{sp}} t)$, while the user holds the robot arm in a fixed position. Several values of the amplitude A_{sp} and frequencies f_{sp} are tested. At very low frequency (left plot) the controller action effectively compensates for the friction distributed along the fluid lines as well as for the disturbances located at the motor side, so that the desired torque amplitude is restored at the output. The tracking error does not appear to increase with higher setpoint amplitudes (right plot), thus preserving the quality of the torque rendering under a large range of load conditions. As expected by the Smith predictor architecture, at higher frequencies (central plot) the effect of the time delay τ is still visible, but the desired amplitude is significantly restored.

3.6 Discussion

This chapter investigated the maximum performance limits that one can reasonably expect from RDHTs. Setpoint torque regulation on an RDHT actuation system was addressed via suitable modeling and feedback control techniques, using a cost-effective solution exploiting an indirect pressure difference measurement. The peculiar structure of the controller based on a Smith predictor was selected to pursue enhanced performance by properly handling the pure time delay revealed in the identification experiments. The origin of the time delay was attributed to a combination of software/communication effects and to unmodelled high-frequency dynamics. Besides

extending the complexity of the model to a higher number of degrees of freedom or selecting a control PC that allows higher sampling and communication frequencies, an interesting future development is the attenuation of the mechanical source of time delay. Effective strategies might consist in reducing the intrinsic elasticity of the transmission, possibly improving the bleeding procedure of the hydraulic lines, as well as selecting rolling diaphragms with different reinforcement fabric or substituting the belts with other flexible transmission elements. The selection of stiffer hoses, which might produce the larger influence, might be prevented by the need of easily routing the hoses through the structure and joints of the manipulator. However, the experimental results confirm the effectiveness of the proposed torque control system both in grounded end-effector configuration and in human-robot-interaction tests; the oscillatory response of the transmission is effectively attenuated, the settling time of the feedback output is reduced by 95%, and the closed-loop torque bandwidth reaches almost the same natural frequency as the open-loop plant, yet without exhibiting any overshoot at the resonance. The low-friction feature of our floating-bonnet layout reduces the backdrivability torque by almost one order of magnitude as compared to existing RDHT robotic architectures of similar size [55]. Future work comprises providing improved setpoint regulation via adaptive versions of the Smith-predictor-based feedback, in addition to studying the stability of the human-robot-interaction paradigm.

Chapter 4

Lightweight Robotic Arm for Safe Human-Robot Interaction

4.1 Overview

This chapter offers the overall assessment of the design approach proposed in this thesis for the construction of human-friendly robotic arms. The prototype of a 2-dof lightweight force-controllable robotic arm based on rolling diaphragm hydrostatic transmissions is built. A comprehensive assessment of the performance that can be achieved by means of remote hydrostatic actuation is offered.

4.2 RDHT Lightweight Arm

Fig. 4.1 (left) shows the lightweight robotic arm developed in this work. It consists of a 2-DOF planar manipulator, in which rolling diaphragm hydrostatic transmissions allow remotizing the electric motors of each joint. Motors are therefore placed at the robot base. Hydrostatic transmissions are conceived as modular elements, so that the same design and dimensions are used for all the joints of the robot. The end-effector is equipped with an handle that allows the interaction with a human user during experiments (see Sect. 4.4), in order to assess robot safety and transparency features. A load cell measures the interaction force $F = [F_x, F_y]^T$ at the handle connection for validation purposes, without being involved in the force control. Each transmission system, connecting the j-th robotic joint ($j = 1$ referring to "shoulder" joint, $j = 2$ referring to "elbow" joint) and the j-th motor, is composed of two fluid lines equally pressurized at resting condition, i.e., $p_{Aj} = p_{Bj} = p_0$. When a positive torque T_{mj} is generated by the j-th motor, the pressurization level of the two fluid lines is perturbed with respect to p_0, increasing p_{Aj} and decreasing p_{Bj}. As a result, a differential pressure $\Delta p_j = p_{Aj} - p_{Bj}$ is generated. Δp_j propagates through the fluid lines up to the robotic joint, where two output cylinders convert it back into torque T_{rj} applied at the joint axis. Under ideal conditions, we have $T_{rj} \approx T_{mj}$. This assumption, however, decays when the working conditions are far from the static case, possibly due to viscous friction and dynamical effects, which arise at high operating frequency. Improved accuracy is therefore pursued by sensing the transmitted torque T_{rj} by means of pressure sensors placed at distal location, i.e., in the vicinity of the robot joint, and closing a low-level torque

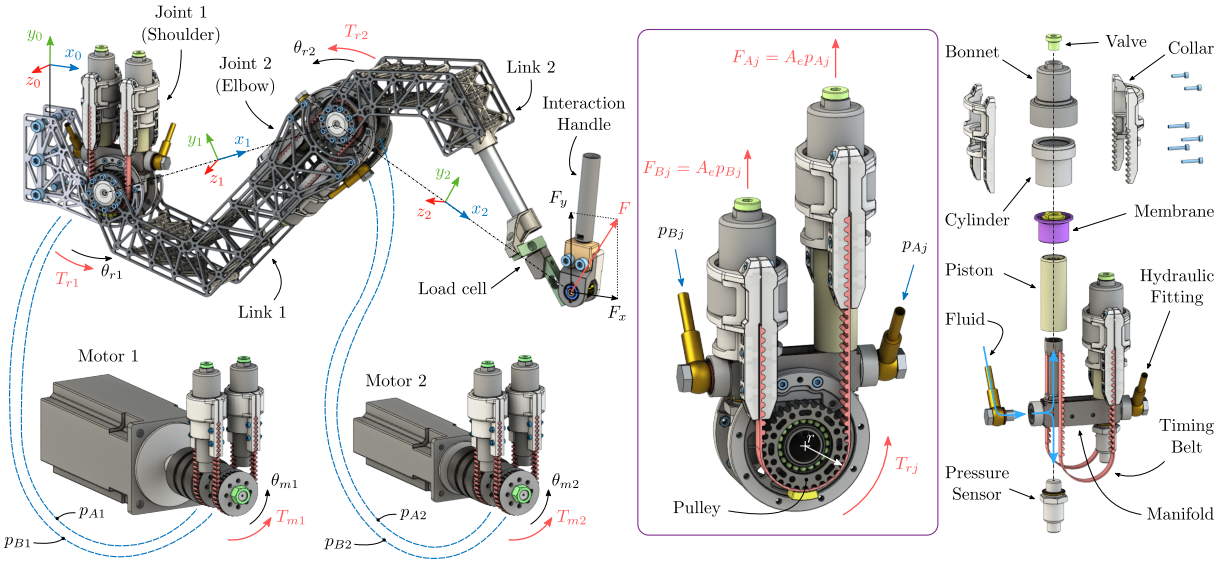

Figure 4.1: Experimental prototype of the lightweight robotic arm. *Left:* overall system; blue dashed lines represent the hydraulic hoses. *Center:* Integrated robotic joint based on rolling diaphragm hydrostatic cylinders with floating-bonnet layout. *Right:* Detailed view of the robotic joint, describing constructive details and the internal distribution of the fluid.

feedback loop at joint level based on this measurement, as justified in Chapter 3.

Fig. 4.1 (center) proposes the novel design of the hydrostatic robotic joint, and helps to better visualize the pressure-to-torque transformation that takes place at the robot axes (the same transformation takes place at the input side, being the transmission symmetric). Two cylinders are coupled in an antagonistic configuration by two timing belts, which are routed around two output toothed pulleys. Each cylinder produces a linear force, proportional to its internal pressure and equivalent area A_e, on its corresponding belt branches:

$$F_{Aj} = A_e p_{Aj}, \quad F_{Bj} = A_e p_{Bj}. \tag{4.1}$$

When pressures p_{Aj} and p_{Bj} coincide, the two cylinders are balanced and no torque is generated on the pulley. When the two pressures are different, instead, a net torque is generated as follows:

$$T_{rj} = r(F_{Aj} - F_{Bj}) = r A_e \Delta p_j, \tag{4.2}$$

where constant r is the pulley radius.

When filled with incompressible fluids, e.g., water, the transmissions achieve high stiffness and synchronous motion between motor and joint rotation, i.e., $\theta_{rj} \approx \theta_{mj}$. In practice, some compliance exists along the hydraulic channels due to the presence of dissolved air and to the elasticity of hoses, belts, and diaphragms. Therefore, this approximated kinematic relation among angles holds as long as the transmitted torque is reasonably small, and the operating condition is significantly far from the resonance frequency.

4.2.1 Integrated Joint and Robotic Arm Details

Fig. 4.1 (center) and (right) show the novel architecture of the integrated robotic joint proposed in this work. The joint has an angular range of $140°$, weighs 700 g, and generates a maximum rated

torque of 25 Nm. The "manifold" connects pistons, pressure sensors, and hydraulic hoses in a compact shape. This element has both structural and hydraulic properties. It undergoes the reaction forces of the two pistons, pushed by the fluid pressure, and the shaft, pulled by the tension forces of the belts. On the other hand, the manifold internal shape distributes the fluid coming from the hydraulic hoses to cylinders and pressure sensors. Moreover, pressure sensors can be placed in close proximity of the cylinder chambers: this is crucial for minimizing the presence of dissipation and compliance sources between sensors and cylinders, therefore maximising the sensing bandwidth and accuracy. Sensing accuracy and mechanical transparency are further enhanced by using rolling diaphragm cylinders with floating-bonnet layout Chapter 2, which prevent sliding and static friction. Cylinders are equipped with a *OA-106-145* rolling diaphragm from DiaCom Corp., characterized by an effective area $A_e = 510$ mm^2, a cylinder diameter $d_c = 27$ mm, a stroke $s_c = 56.8$ mm, and a 20 bar maximum working pressure. Timing belts are routed around two output toothed pulleys, with a $r = 23.9$ mm primitive radius. Joint rotation θ_{rj} is measured by means of a RM08D01-12 magnetic relative encoder from RLS (4096 cpr resolution), while fluid pressures p_{Aj} and p_{Bj} are measured by means of two 3100x pressure sensors from Gems Sensors (16 bar maximum pressure measurement and 0.04 bar accuracy). The hydraulic hoses, characterised by a flexible coating of Kevlar fibers, have length of 1 m and internal diameter of 5 mm; distilled water is used as working fluid. Direct-drive AM8043 (4.90 Nm rated torque, 28.0 Nm peak torque) and AM8053 (14.9 Nm rated torque, 53.1 Nm peak torque) motors from Beckhoff are used for elbow and shoulder joint actuation, respectively. Both motors are equipped with a 24 bit (20 bit per revolution) multi-turn absolute encoder, which measure $\theta_m j$. The control unit consists in a CX51 Beckhoff Embedded-PC based on a TwinCAT real-time communication protocol. Experiments are performed with a fixed sampling rate of 2 kHz.

4.3 System Modeling And Control

This section presents a dynamical model of the robot-transmission ensemble, aimed at highlighting the essential structure of robotic arms actuated by means of hydrostatic transmissions, Fig. 4.2 (left). On top of this description, a model-based low-level torque controller relying on pressure feedback is designed, Fig. 4.2 (right); the low-level controller is then nested in a high-level interactive controller that modulates virtual stiffness and damping response of the robot in the operational space, adjusting human-robot-interaction features, Fig. 4.5.

4.3.1 Open-loop System: Modeling and Control

The left and right pictures in Fig. 4.2 offer a parallel between the physical modeling of the manipulator and the block-diagram description of the system dynamics and control structures. The vector-valued quantity $\theta_r = [\theta_{r1}, \theta_{r2}]^T$ defines the angular position of the two robot joints and, therefore, the posture of the arm. Parameters m_{rj} and J_{rj} describe the mass and inertial properties of the links. $P_e = [P_{ex}, P_{ey}]^T$ defines the end-effector position in the workspace and $F = [F_x, F_y]^T$ defines the force applied by the robot on the surrounding environment at position P_e. Each joint is connected to the corresponding motor by means of a hydrostatic transmission system with stiffness k_{mj}. The electric motors are characterised by moment of inertia J_{mj}, and generate actuation torques $T_m = [T_{m1}, T_{m2}]^T$.

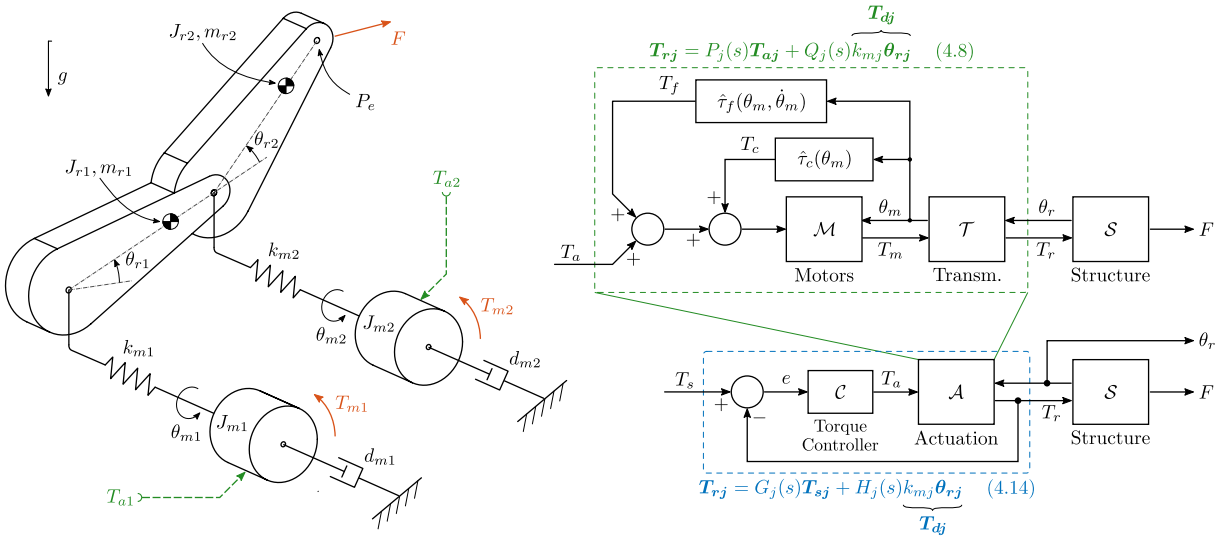

Figure 4.2: *Left:* model of the pre-compensated robotic arm according to (4.3). Notice that d_{m1} and d_{m2} indicate the residual damping after applying compensation T_f. *Right:* block-diagram representation of the precompensated plant (in green) and the low-level torque-control scheme (in blue).

The physical system is described by the three main blocks in Fig. 4.2 (top-right): block $\mathcal{M}$ contains the dynamics of the motors (it also incorporates the current controller executed by the motor drivers), block $\mathcal{T}$ represents the transmission system in terms of spring and damping elements, and block $\mathcal{S}$ describes the dynamics of the arm structure. The motors are rigidly connected to the transmission inputs, while the output side of the transmissions is rigidly connected to the links of the arm. These interconnections can be described as force-position feedback, where the coupling between $\mathcal{M}$ and $\mathcal{T}$ is described by quantities $T_m = [T_{m1}, T_{m2}]^T$ and $\theta_m = [\theta_{m1}, \theta_{m2}]^T$, while the coupling between $\mathcal{T}$ and $\mathcal{S}$ is described by quantities $T_r = [T_{r1}, T_{r2}]^T$ and $\theta_r = [\theta_{r1}, \theta_{r2}]^T$. Here, T_{mj} are the torques generated by the motors and T_{rj} are the joint torques measured by means of the pressure sensors. Quantities θ_{mj} and θ_{rj} correspond instead to the motor and joint rotation angles, respectively.

Despite the high open-loop transparency, the torque generation and transmission are affected by plausible disturbance torques: the motors $\mathcal{M}$ are subject to the cogging torque generated by the stator-rotor magnetic interaction and the transmissions $\mathcal{T}$ are affected by the viscous friction produced along the fluid lines. The disturbance torques can be characterized and then compensated by means of the feedback actions T_c and T_f (see Sect. 4.6), ensuring that T_{rj} (nominally) coincide with the commanded torques T_{aj}.

After applying compensations T_c and T_f, the equation of motion of the system can be expressed as follows:

$$\begin{bmatrix} M_m & 0 \\ 0 & M_r(\theta_r) \end{bmatrix} \begin{bmatrix} \ddot{\theta}_m \\ \ddot{\theta}_r \end{bmatrix} + \begin{bmatrix} D_m & 0 \\ 0 & D_r \end{bmatrix} \begin{bmatrix} \dot{\theta}_m \\ \dot{\theta}_r \end{bmatrix} + \begin{bmatrix} K_m & -K_m \\ -K_m & K_m \end{bmatrix} \begin{bmatrix} \theta_m \\ \theta_r \end{bmatrix} + \begin{bmatrix} 0 \\ C_r(\theta_r, \dot{\theta}_r)\dot{\theta}_r + G_r(\theta_r) \end{bmatrix} = \\ = \begin{bmatrix} I \\ 0 \end{bmatrix} T_a + \begin{bmatrix} 0 \\ J^T(\theta_r) \end{bmatrix} F, \tag{4.3}$$

where M_m and $M_r(\theta_r)$ are the inertia matrices associated with the motors and the robot, D_m and D_r are the corresponding damping matrices, and K_m is the stiffness matrix associated with

the coupling. Matrices $C_r(\theta_r, \dot{\theta}_r)\dot{\theta}_r$ and $G_r(\theta_r)$ collect the Coriolis and gravity effects, and J is the Jacobian matrix of the robot arm. Subscripts "m" and "r" refer to the motor unit, namely $\mathcal{M}$ and $\mathcal{T}$, and robotic structure $\mathcal{S}$, respectively.

4.3.2 Torque Dynamics Analysis

We introduce the following change of coordinates (which is always well-defined, since $K_m > 0$):

$$\begin{bmatrix} T_r \\ \theta_r \end{bmatrix} = \begin{bmatrix} K_m & -K_m \\ 0 & I \end{bmatrix} \begin{bmatrix} \theta_m \\ \theta_r \end{bmatrix}. \tag{4.4}$$

and, by replacing (4.4) in (4.3), we obtain:

$$\begin{bmatrix} M_m K_m^{-1} & M_m \\ 0 & M_r(\theta_r) \end{bmatrix} \begin{bmatrix} \ddot{T}_r \\ \ddot{\theta}_r \end{bmatrix} + \begin{bmatrix} D_m K_m^{-1} & D_m \\ 0 & D_r \end{bmatrix} \begin{bmatrix} \dot{T}_r \\ \dot{\theta}_r \end{bmatrix} + \begin{bmatrix} I & 0 \\ -I & 0 \end{bmatrix} \begin{bmatrix} T_r \\ \theta_r \end{bmatrix} + \begin{bmatrix} 0 \\ C_r(\theta_r, \dot{\theta}_r)\dot{\theta}_r + G_r(\theta_r) \end{bmatrix} = \\ = \begin{bmatrix} I \\ 0 \end{bmatrix} T_a + \begin{bmatrix} 0 \\ J^T(\theta_r) \end{bmatrix} F. \tag{4.5}$$

The transmitted torque T_r appears explicitly as state variable in the transformed model (4.5). Extracting the differential equations corresponding to T_{rj} in scalar form (for $j = 1, 2$), we get:

$$\frac{J_{mj}}{k_{mj}} \ddot{T}_{rj} + \frac{d_{mj}}{k_{mj}} \dot{T}_{rj} + T_{rj} = T_{aj} - J_{mj} \ddot{\theta}_{rj} - d_{mj} \dot{\theta}_{rj}. \tag{4.6}$$

From the point of view of equation (4.6), T_{aj} is a control input and T_{rj} is the corresponding system output, while rotation θ_{rj} acts as a disturbance on the relationship between T_{aj} and T_{rj}. The impact of such disturbance θ_{rj} is negligible at low rotational speeds (note that $T_{aj} = T_{rj}$ for $\theta_{rj} = const$), and becomes more meaningful as the operation speed increases. To better quantify the effects of disturbance θ_{rj} on the transmitted torque dynamics, a scaled disturbance torque T_{dj} is defined according to

$$T_{dj} = k_{mj} \theta_{rj}, \tag{4.7}$$

so that control input, output, and disturbance are dimensionally equivalent (i.e. they all correspond to torques). By replacing (4.7) in (4.6), taking the Laplace transform (bold letters indicate variables in the Laplace domain, i.e. $\boldsymbol{x} := \mathcal{L}[x(t)]$), and solving for variable $\boldsymbol{T_{rj}}$, we get:

$$\boldsymbol{T_{rj}} = \frac{\omega_j^2}{s^2 + 2\xi_j \omega_j s + \omega_j^2} \boldsymbol{T_{aj}} - \frac{s(s + 2\xi_j \omega_j)}{s^2 + 2\xi_j \omega_j s + \omega_j^2} \boldsymbol{T_{dj}} = P_j(s) \boldsymbol{T_{aj}} + Q_j(s) \boldsymbol{T_{dj}}, \tag{4.8}$$

where $\omega_j^2 = k_{mj}/J_{mj}$ and $\xi_j = c_{mj}/(2J_{mj}\omega_j)$ represent the natural frequency and the modal damping of the second-order transfer function from $\boldsymbol{T_{aj}}$ to $\boldsymbol{T_{rj}}$. We refer to (4.8), depicted in green in Fig. 4.2 (top-right), as *open loop* response, since it describes the system behavior when no torque feedback is applied. Fig. 4.3 (left) shows the experimental identification of transfer function $P_j(s)$, and Fig. 4.3 (center) shows the comparison between $P_j(s)$ and $Q_j(s)$ in the frequency domain for both of the hydrostatic transmissions. By replacing $s = j\omega$ in (4.8) and evaluating the low-frequency limit case, we obtain:

$$\boldsymbol{T_{rj}} \approx \boldsymbol{T_{aj}} - j \left(2\xi_j \frac{\omega}{\omega_j} \right) \boldsymbol{T_{dj}}. \tag{4.9}$$

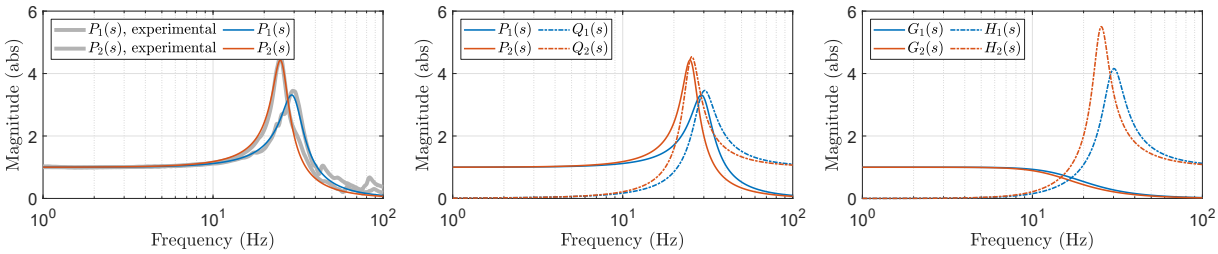

Figure 4.3: Response of shoulder and elbow transmissions in the frequency domain. *Left:* experimental identification of the open-loop transfer functions $P_j(s)$ (4.8). Experimental data are produced by fixing the end-effector to the ground and commanding T_{aj} in the form of chirp functions. The identified dynamical parameters correspond to $\xi_1 = 0.15$, $\omega_1 = 29.7$ Hz, $\xi_2 = 0.11$ and $\omega_2 = 25.2$ Hz. *Center:* analytical analysis of the open-loop transfer functions $P_j(s)$ and $Q_j(s)$. *Right:* analytical analysis of the closed-loop transfer functions $G_j(s)$ and $H_j(s)$, corresponding to the following selection of free design parameters: $\xi_{t1} = \sqrt{2}/2$, $\omega_{t1} = 16$ Hz, $\xi_{t2} = \sqrt{2}/2$ and $\omega_{t2} = 14$ Hz (imposing $G_j(s)$ critically damped)

Equation (4.9) reveals that the transmitted torque T_{rj} closely follows T_{aj} as long as the robot operates at relatively low frequencies with respect to the open-loop natural frequency ω_j. The dynamic disturbances T_{dj}, due to coupling between motor and structure, become non negligible as the driving speed increases.

4.3.3 Low-level Closed-loop Torque Control

Since the open loop values of ξ_j and ω_j may lead to unsatisfactory under-damped dynamic performance, the response of system (4.8) is further shaped by means of feedback control. To this end, the low-level closed-loop torque controller based on pressure feedback and proposed in Chapter 3 is applied; it is represented in Fig. 4.2 (bottom-right). The transfer function from T_{sj} (setpoint) to T_{rj} can be arbitrarily shaped by the designer. Afterwards, we investigate the influence of disturbance T_{dj} on such a closed-loop architecture.
The closed-loop torque controller $\mathcal{C}$ is built,

$$\mathcal{C} = \begin{bmatrix} C_1(s) & 0 \\ 0 & C_2(s) \end{bmatrix}, \tag{4.10}$$

in order to act independently on each transmission line as:

$$\boldsymbol{T_{aj}} = C_j(s)\boldsymbol{e_j} = C_j(s)\left(\boldsymbol{T_{sj}} - \boldsymbol{T_{rj}}\right). \tag{4.11}$$

The structure of $P_j(s)$ in (4.8) suggests to choose $C_j(s)$ in the form of filtered PIDs:

$$C(s) = k_{pj} + \frac{k_{ij}}{s} + \frac{k_{dj}s}{\tau_{dj}s + 1} = \frac{\bar{k}_{dj}s^2 + \bar{k}_{pj}s + \bar{k}_{ij}}{s\left(\tau_{dj}s + 1\right)} \tag{4.12}$$

with $\bar{k}_{dj} = k_{dj} + k_{pj}\tau_{dj}$, $\bar{k}_{pj} = k_{pj} + k_{ij}\tau_{dj}$ and $\bar{k}_{ij} = k_{ij}$. Controller coefficients are chosen according to:

$$\bar{k}_{pj} = \frac{\xi_j\omega_{tj}}{\xi_{tj}\omega_j}, \bar{k}_{ij} = \frac{\omega_{tj}}{2\xi_{tj}}, \bar{k}_{dj} = \frac{\omega_{tj}}{2\xi_{tj}\omega_j^2}, \tau_{dj} = \frac{1}{2\xi_{tj}\omega_{tj}}, \tag{4.13}$$

where the free design parameters ξ_{tj} and ω_{tj} can be arbitrarily set to define the modal damping and natural frequency of the closed loop. By replacing (4.11) – (4.13) in (4.8), we obtain:

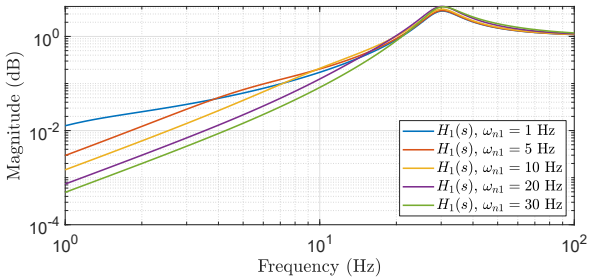

Figure 4.4: Parametric analysis of transfer function $H_1(s)$ with respect of different choices of parameter ω_{t1}. Parameter ξ_{t1} is always assumed equal to $\sqrt{2}/2$ to achieve critically-damped response. The plant corresponds to identification parameters $\xi_1 = 0.15$, $\omega_1 = 29.7$ Hz. The analysis of joint 2 would show same trends and it is not represented in the picture.

$$\begin{aligned} \boldsymbol{T_{rj}} = & \frac{\omega_{tj}^2}{s^2 + 2\xi_{tj}\omega_{tj}s + \omega_{tj}^2}\boldsymbol{T_{sj}} - \frac{s^2(s + 2\xi_j\omega_j)(s + 2\xi_{tj}\omega_{tj})}{(s^2 + 2\xi_j\omega_j s + \omega_j^2)(s^2 + 2\xi_{tj}\omega_{tj}s + \omega_{tj}^2)}\boldsymbol{T_{dj}} \\ = & \; G_j(s)\boldsymbol{T_{sj}} + H_j(s)\boldsymbol{T_{dj}} \end{aligned} \tag{4.14}$$

meaning that the proposed controller permits to replace the second-order open-loop dynamics $P_j(s)$, described by coefficients ω_j and ξ_j, with the target second-order closed-loop dynamics $G_j(s)$ corresponding to coefficients ω_{tj} and ξ_{tj} freely selected by the designer. In this case, the effect of disturbance T_{dj} is described by the transfer function $H_j(s)$. We refer to (4.14) as *closed loop* since it describes the system response when the low-level torque controller is applied; it is depicted in blue in Fig. 4.2 (bottom-right) and represented in Fig. 4.3 (right) in the frequency domain. By considering again the low-frequency limit case of (4.14), we obtain:

$$\boldsymbol{T_{rj}} \approx \boldsymbol{T_{sj}} + \left(2\xi_j\frac{\omega}{\omega_j}\right)\left(2\xi_{tj}\frac{\omega}{\omega_{tj}}\right)\boldsymbol{T_{dj}}. \tag{4.15}$$

The comparison of (4.15) and (4.9) empirically shows that the disturbance effect produced by large rotation speeds can be further attenuated with respect to the open-loop case by increasing the closed-loop bandwidth ω_{tj}; this can be visualized in the parametric analysis of $H_j(s)$ in Fig. 4.4. From (4.13), choosing large ω_{tj} results in high control gains. In practice, the control gains cannot be chosen arbitrarily large due to stability reasons (e.g., as a result of neglected high-frequency dynamics).

More generally, (4.14) implies that T_{rj} tightly follows T_{sj} as long as magnitude of $G_j(j\omega)$ approaches the unit value and magnitude of $H_j(j\omega)$ is small, namely:

$$|G_j(j\omega)| > 0.95 \quad \text{and} \quad |H_j(j\omega)| < 0.05. \tag{4.16}$$

Transfer functions $G_j(s)$ and $H_j(s)$ are shown in Fig. 4.3 for real values of model coefficients and control gains, proving that robot and transmission (together with motors) dynamic decoupling (4.16) holds in the range 0–6 Hz.

In this range, the arm $\mathcal{S}$ can be actually controlled by neglecting motors and transmission dynamics, holding $T_{rj} \approx T_{sj}$. When this appoximation holds true, the differential equation for θ_r appearing in (4.5) can be rewritten as follows

$$M_r(\theta_r)\ddot{\theta}_r + D_r\dot{\theta}_r + C_r(\theta_r, \dot{\theta}_r)\dot{\theta}_r + G_r(\theta_r) = T_s + J^T(\theta_r)F. \tag{4.17}$$

In equation (4.17) T_s plays the same role of the generalized joint torque in conventional robot control schemes, and thus it can be used to directly control the robot motion.

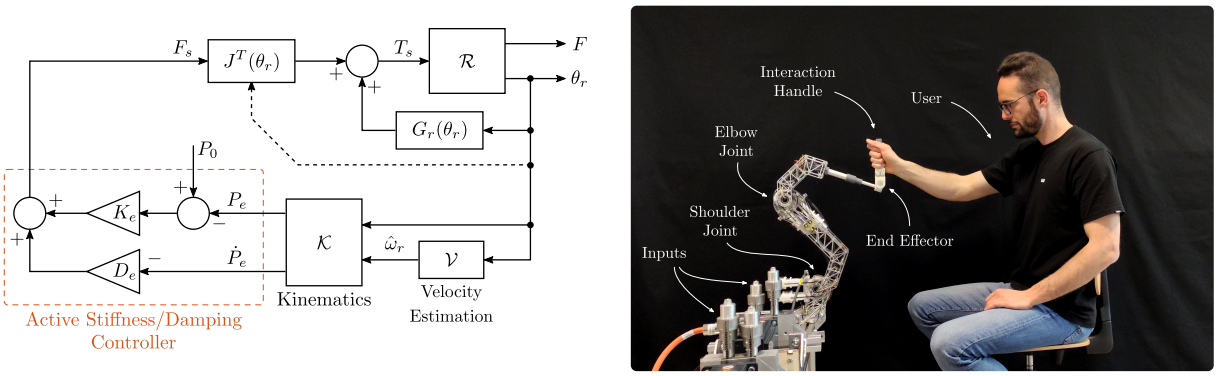

Figure 4.5: *Left:* High-level control scheme for active stiffness/damping modulation in the operational space. *Right:* experimental setup (notice that the robot base is rotated by 90° in the photo in order to offer a clearer view of the setup, but all the tests are performed in the nominal configuration represented in Fig. 4.1)

4.3.4 High-level Interactive Controller

This section develops a high-level feedback control law which aims at modulating the interaction behavior of the robot at the end-effector power port $F - \dot{P}_e$. To this end, we consider the robot dynamics with pressure feedback loops under the assumption that the inner controllers have been tuned such that (4.17) holds true in the low-frequency range of interest for typical human-robot-interaction tasks. The high-level controller, represented in Fig. 4.5, is implemented by choosing T_s in the form of an operating space PD with gravity compensation:

$$T_s = G_r(\theta_r) - J^T(\theta_r)\left(K_e(P_e(\theta_r) - P_0) + D_e J(\theta_r)\dot{\theta}_r\right). \tag{4.18}$$

Quantities K_e and D_e are virtual stiffness and damping matrices in the operating space, given by

$$K_e = \begin{bmatrix} k_{ex} & 0 \\ 0 & k_{ey} \end{bmatrix} > 0, \quad D_e = \begin{bmatrix} d_{ex} & 0 \\ 0 & d_{ey} \end{bmatrix} > 0, \tag{4.19}$$

while $P_0 = [P_{0x}, P_{0y}]^T$ defines a virtual equilibrium position of the end-effector. The current end-effector position $P_e(\theta_r)$ is obtained through direct kinematics, while $\dot{\theta}_r$ is estimated through measurements of θ_r by means of high-pass filters, i.e.,

$$\begin{cases} \dot{x} = K_f(\theta_r - x) \\ \hat{\omega}_r = K_f(\theta_r - x) \end{cases} \tag{4.20}$$

where $\hat{\omega}_r$ is an estimate of $\dot{\theta}_r$, x is an internal state variable of the filter, and

$$K_f = \begin{bmatrix} k_{f1} & 0 \\ 0 & k_{f2} \end{bmatrix} > 0 \tag{4.21}$$

defines the filter cut-off frequencies (experimental settings: $k_{f1} = k_{f2} = 50$). By replacing (4.18) into (4.17), the high-level closed loop dynamics is given as follows:

$$M_r(\theta_r)\ddot{\theta}_r + D_r\dot{\theta}_r + J^T(\theta_r)D_e J(\theta_r)\dot{\theta}_r + C_r(\theta_r, \dot{\theta}_r)\dot{\theta}_r + J^T(\theta_r)K_e\left(P_e(\theta_r) - P_0\right) = J^T(\theta_r)F. \tag{4.22}$$

It is readily observed that, at steady state, (4.22) implies

$$J^T(\theta_r)K_e\left(P_e(\theta_r) - P_0\right) = J^T(\theta_r)F. \tag{4.23}$$

In non-singular configurations (i.e., $J(\theta_r)$ is full rank), (4.23) implies

$$K_e\left(P_e(\theta_r) - P_0\right) = F, \tag{4.24}$$

which represents a linear elastic characteristics in the operating space. Quantities K_e and P_0 can then be interpreted as a virtual stiffness and contact-free end-effector position in the operating space, respectively.
An attractive feature of control law (4.18) is that the closed-loop system (4.22) is passive at the end-effector port $F - \dot{P}_e$ [71]. This is proved by considering the following storage function:

$$H(\theta_r, \dot{\theta}_r) = \frac{1}{2}\dot{\theta}_r^T M_r(\theta_r)\dot{\theta}_r + \frac{1}{2}(P(\theta_r) - P_0)^T K_e\left(P(\theta_r) - P_0\right). \tag{4.25}$$

Differentiating (4.25) along trajectories of (4.22), and recalling the skew-symmetry of matrix $\dot{M}_r(\theta_r) - 2C_r(\theta_r, \dot{\theta}_r)$, we obtain

$$\begin{aligned} \dot{H} &= -\dot{\theta}_r^T D_r \dot{\theta}_r - \dot{\theta}_r^T J^T(\theta_r) D_e J(\theta_r)\dot{\theta}_r + \dot{\theta}_r^T J^T(\theta_r)F \\ &= -\dot{\theta}_r^T D_r \dot{\theta}_r - \dot{P}_e^T D_e \dot{P}_e + \dot{P}_e^T F \\ &\leq \dot{P}_e^T F, \end{aligned} \tag{4.26}$$

which is indeed the well-known passivity inequality. The above discussed passivity property allows us to state that the manipulator will remain stable whenever its end-effector interact with any external passive system. This property makes the developed architecture particularly suitable for safe interaction control with unstructured systems and environments. In addition, (4.25) clearly reveals that D_e permits to directly modulate the damping in the operating space.

4.4 Experiments

This section assesses the effectiveness of the overall design strategy proposed for interactive machines, which results from a combined development of specific mechanical and control design paradigms. Pursuing the objective of creating a human-friendly robotic arm, all the experiments are performed in a human-robot-interaction context, where the human user operates the robot through the end-effector handle. Experiments compare the open-loop (4.8) and the closed-loop response (4.14) of the system.

4.4.1 Sine Tracking

First, the force tracking accuracy is assessed; the human user holds the handle in a fixed position and, bypassing the active compliance controller, a desired force F_s is commanded according to (4.27)

$$F_s = \begin{bmatrix} 0 \\ A sin\left(2\pi f t\right) \end{bmatrix} \tag{4.27}$$

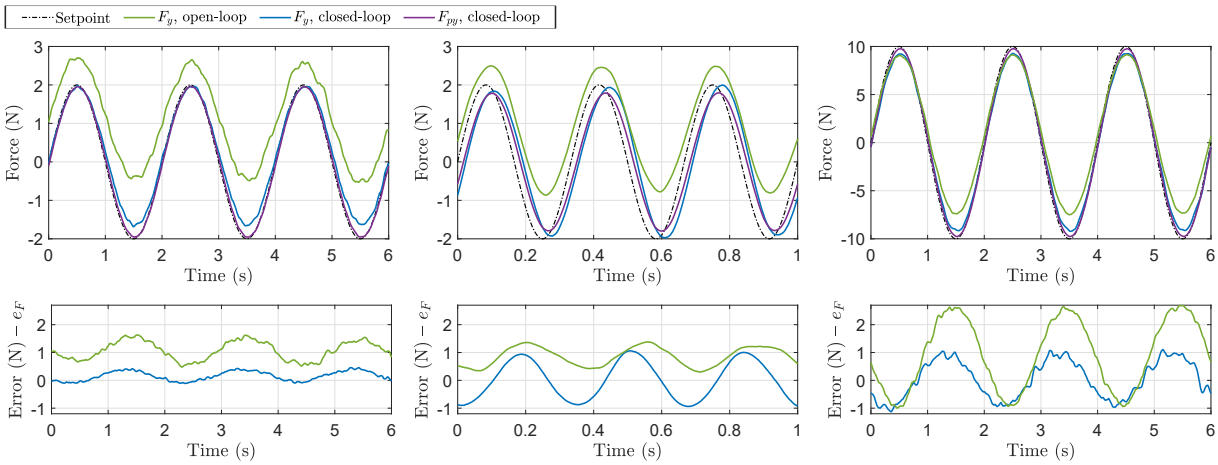

Figure 4.6: Sine tracking experiment. The human user holds the handle in a fixed position and a sinusoidal reference is tracked at the end effector along the y direction (dashed-dotted black line). The green line and the blue line represent the load cell measurement in the open loop and in the closed loop, respectively. The purple line represents the output force measured by means of the pressure sensors in the closed loop case. *Left:* low-amplitude low-frequency test ($A = 2$ N, $\omega = 0.25$ Hz); *Center:* repetition with increased setpoint frequency ($A = 2$ N, $\omega = 3$ Hz); *Right:* repetition with increased setpoint frequency ($A = 10$ N, $\omega = 0.25$ Hz).

where constant A is the setpoint amplitude and constant f is the setpoint frequency. Results are shown in Fig. 4.6. The left plots compare the measurement of outputs F_y produced by the open loop (green line) and the closed loop (blue line) in a low-aplitude ($A = 2$ N) and low-frequelcy ($f = 0.25$ Hz) test. The open-loop tracking error, which reaches a maximum value of 1.6 N in the open loop, is consistently reduced in the closed loop (max. 0.45 N), where the action of the low-level controller removes the residual bias (possibly due to some imperfections and/or residual spring-rate effect in the rolling diaphragms), and ensures a closer match with the setpoint (dashed-dotted black line). The plot also shows the "internal" measurement of the output force $\hat{F}_y$ by means of the pressure sensors (purple line) in the case of the closed loop: this quantity closely matches the setpoint and is always close to the actual output force measured by means of the load cell. Similar conclusions can be drawn when repeating the test with higher setpoint frequency ($f = 3$ Hz), Fig. 4.6 (center), and with higher setpoint amplitude ($A = 10$ N), Fig. 4.6 (right), testifying that the accuracy of the robot is preserved for faster velocities and higher loads.

4.4.2 Backdrivability

The response of the robot is further investigated by means of backdrivability tests. Differently from previous experiments, large displacements are taken into account. Virtual damping D_e and virtual stiffness K_e are set to zero, and the user imposes a displacement at the end-effector along predetermined trajectories: in particular, as shown in Fig. 4.7 (left), vertical and horizontal trajectories with an amplitude of 150 mm are performed about different nominal postures of the manipulator in order to investigate how the behaviour of the robot varies according to displacement direction and arm posture. Fig. 4.7 (center) and Fig. 4.7 (top-right) show the measurements of the output components F_x and F_y during low-velocity displacements along y and x directions, respectively: in each plot, colors are used to relate the force measurements to the correspond-

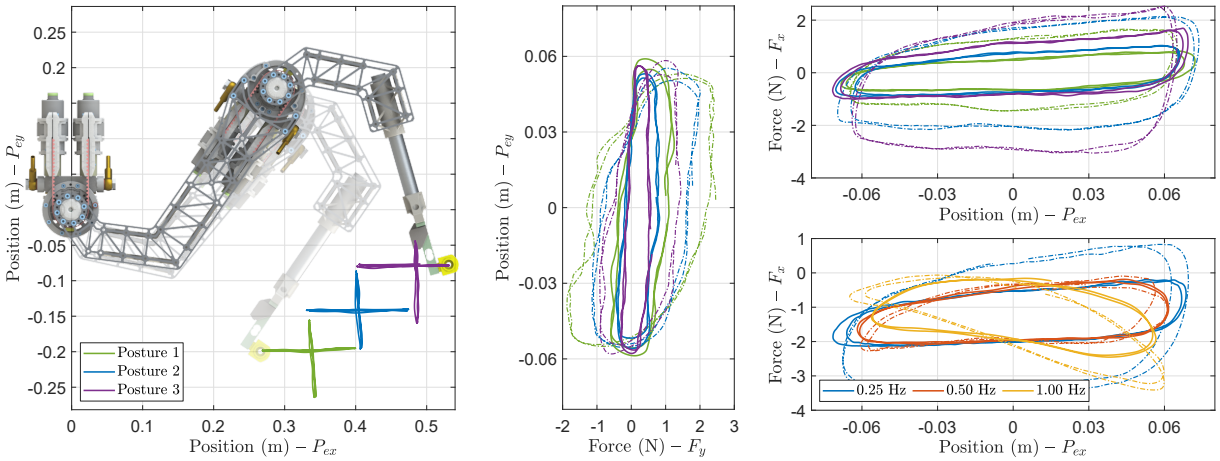

Figure 4.7: Backdrivability test. F_a is set to zero, while the user imposes a displacement at the end-effector (150 mm amplitude and 0.25 Hz frequency) along the x and y directions. Different colors refer to different nominal postures of the robot, while different line styles refer to the control configuration (solid lines for closed loop, dashed lines for open loop). *Left:* vertical and horizontal trajectories performed about 3 different reference postures; *Center*: force F_y measured during vertical displacements; *Top-right*: force F_x measured during horizontal displacements; *Bottom-right*: the horizontal test about posture 2 is repeated with different frequencies.

ing trajectory , while the line style is used to distinguish among open-loop (dashed lines) and closed-loop (solid lines) responses. The mean values of position measurements are removed in Fig. 4.7 (center) and Fig. 4.7 (right) in order to overlap plots that are actually located in different positions of the workspace. The effect of the low-level controller is again clearly visible in these tests, making the closed loop more accurate and transparent than the open loop, thus reducing the effort required the user to backdrive the robot in all the experiments: compared to the open loop, the maximum effort is reduced from 3 N to 1.6 N (worst case values); moreover, measurements performed in the closed-loop configuration are more repeatable. It is also interesting to notice the influence of the arm posture on the overall response of the robot: when the arm is extended (purple posture) the highest accuracy is obtained in displacements performed along the y direction, see the central plot, while the highest accuracy along the x direction is obtained when the arm is contracted (green posture), see the top-right plot (in this case the purple measurement actually corresponds to the worse performance). This confirms the known fact that a planar arm loses controllability along the direction perpendicular to the arm itself when fully extended, while controllability along that direction is restored as much as the elbow joint bends. Finally, Fig. 4.7 (bottom-right) describes how backdrivability properties extend to higher velocities: additional tests about posture 2 are performed by increasing the displacement frequency at each repetition, ranging from 0.25 Hz to 1 Hz. The maximum effort required to backdrive the robot does not show a clear dependence on the velocity in the current experimental conditions and, in general, the closed loop measurements are again more repeatable than the open loop ones. This set of high-speed tests (characterised by an end-effector maximum velocity of 0.42 m/s and an elbow-joint maximum velocity of 1.64 rad/s) probably highlights the most relevant difference between the proposed architecture, i.e. remote direct drive motorization, and common industrial highly-geared robotic arms, being capable of easily preserving accuracy and transparency features at high velocities.

Alongside accuracy and transparency features, the proposed architecture proves also power-

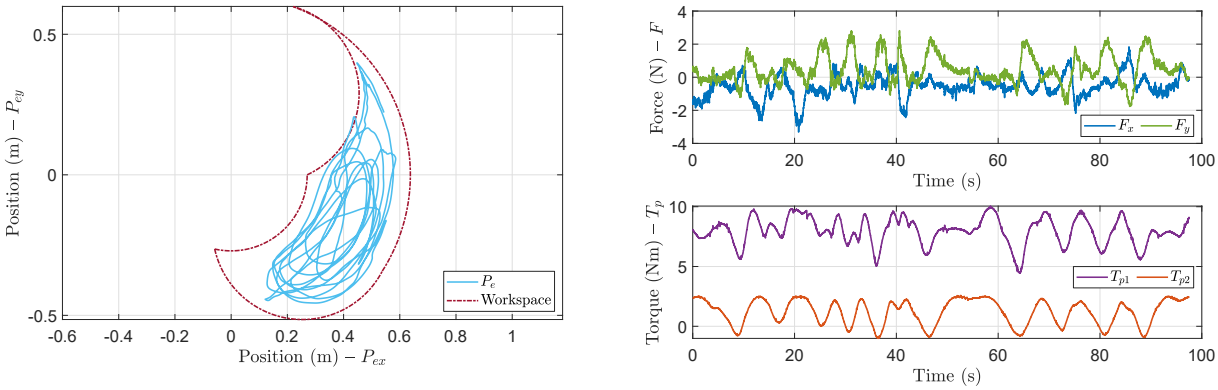

Figure 4.8: Backdrivability test with an additional 1.5 kg payload fixed close to the end-effector. *Left*: trajecotry imposed at the end-effector by the user (light-blue line) covering a wide surface of the reachable workspace (dashed-dotted red line); *Top-right*: end-effector force components F_x and F_y measured by the load-cell; *Bottom-right:* shoulder-joint torque profile.

ful by performing a further backdrivability test with a payload of 1.5 kg applied in proximity of the end effector, Fig. 4.8 (the weight of the additional payload is compensated by a τ_g action specifically designed for this experiment). The user imposed an arbitrary trajectory at the end effector, Fig. 4.8 (left), covering almost the entire extension of the operational workspace. The interaction force measured at the user hand, Fig. 4.8 (top-right), maintain within the expected limit values measured in previous standard backdrivability experiments, never requiring the user an effort higher than 3 N to backdrive the robot. The response is reasonably transparent and uniform over the entire workspace even when the transmission is heavily loaded: in particular, Fig. 4.8 (bottom-right) shows the torque profile of the two joints recorded during the experiment, revealing a mean working torque of ~ 8 Nm and a peak torque of 10 Nm at the shoulder joint. These values are smaller than the maximum torque that the transmission can provide, however testing the structural limits of the robot is beyond the purpose of this work, and this test is considered representative enough of the gentle-yet-powerful design paradigm.

4.4.3 Active Stiffness and Damping

Finally, the overall control architecture is tested in a complex human-robot-interaction test, requiring the robot to display virtual impedance, by opposing to the movement of the user hand with viscous or elastic resistances, Fig. 4.9 (left) and Fig. 4.9 (right) respectively. Different damping and stiffness coefficients are specified along the x and y axes in order to challenge the robot and obtain a sufficiently general description of the overall performance: the viscous action in the first test is defined by parameters $k_{ex} = k_{ey} = 0$ N/m, $d_{ex} = 0$ Ns/m and $d_{ey} = 20$ Ns/m, while the elastic resistance in the second test is defined by parameters $d_{ex} = d_{ey} = 0$ Nm/s, $k_{ex} = 160$ N/m and $k_{ey} = 80$ N/m. Both of the tests show similar tracking errors (bottom plots) along the x and y axis, proving the tracking accuracy independent of the different loads acting along the two directions; this result might not be easily achieved by existing lightweight robots actuated by transmission systems based on different technologies. Consistently with results of Fig. 4.7, a maximum error of 2.7 N is measured in the first test, and a maximum error of 2.5 N is measured in the second one.

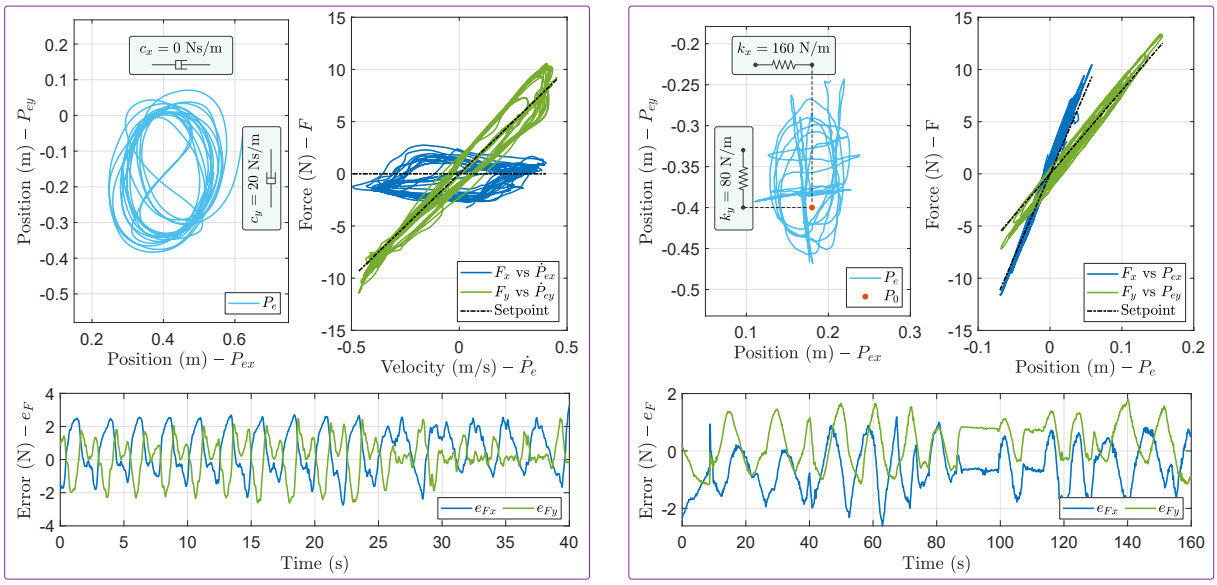

Figure 4.9: Human-robot-interaction test: the user imposes arbitrary trajectories at the end-effector (light blu lines) while the robot opposes to the motion of the user hand by applying (*Left*) a viscous action and (*Right*) an elastic resistance (the red point indicates the virtual equilibrium position P_0). Different damping/stiffness coefficients are chosen along the x and y axis: $d_{ex} = 0$ Ns/m and $d_{ey} = 20$ Ns/m in the first test, while of $k_{ex} = 160$ N/m and $k_{ey} = 80$ N/m in the second test. In both of the plots, the *top-left* picture shows the hand trajectory; the *top-right* picture plots the components of both the force reference F_a and the actual interaction force F with respect to the corresponding displacement/velocity component; the *bottom* picture show the components of the force tracking error $e_F = F_a - F$

4.5 Discussion

This chapter addresses simultaneous development of novel mechanical and control approaches for human-friendly robotic arms. Hydrostatic transmissions based on low-friction rolling diaphragm cylinders allow remote positioning of the electric actuators for creating lightweight robotic arms with enhanced dynamical properties. A simple controller based on pressure feedback and second-order dynamics identification ensures stable closed-loop force setpoint regulation, arm and transmission dynamics decoupling up to 6 Hz, and structural resonance attenuation. The closed loop increases backdrivability and force tracking accuracy in a variety of experimental conditions; the maximum backdriving force at the end effector is measured equal to 3 N in open loop and 1.6 N in closed loop. The lightweight robotic arm has proven also powerful in a collaborative manipulation experiment by helping the user to carry a payload of 1.5 kg across its entire workspace, while maintaining unchanged interaction transparency features; the shoulder joint has been loaded up to 10 Nm. Unchanged backdrivability quality has been confirmed in heavy load tasks, proving that frictional and dynamical properties of hydrostatic transmissions are independent of the applied load; this is a big advantage with respect to existing cable-based transmissions or similar solutions. Complex human-machine-interaction tasks involving the simulation of virtual stiffness and damping coefficients have been accomplished with force errors lower than 3 N.

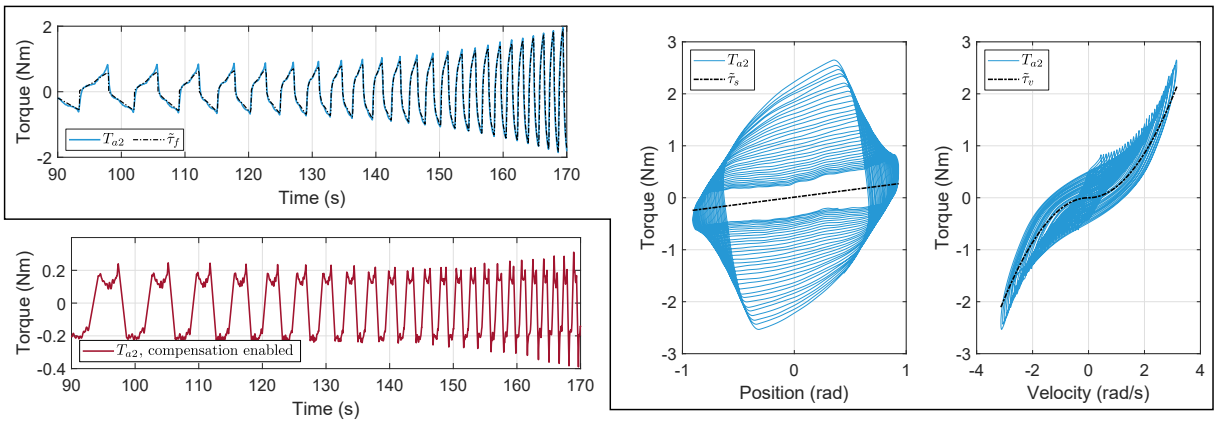

Figure 4.10: Measurement of the viscous friction generated by the hydrostatic transmission of the elbow joint. This experiment is performed by position-controlling the motor along constant-velocity trajectories with a rotation range of $-65° \leq \theta_m \leq 65°$ and measuring the commanded torque T_{a2}. The velocity is increased at each repetition from 0.1 rad/s to 3 rad/s. *Top-left:* measurement and identification of torque T_{a2} without viscous compensation. The same measurement is represented with respect to *(center)* the motor position and *(right)* the motor velocity. *Bottom-left:* measurement of torque T_{a2} during a repetition of the experiment with active viscous compensation.

4.6 APPENDIX: Friction Compensation

This section studies the friction that affects the subsystem composed of the electric motor and the hydrostatic transmission; the cogging torque compensation is active and the output side of the transmission is detached from the robotic arm. Results are discussed in the case of elbow-joint actuation line; the actuation line of the shoulder joint gives comparable results.

The motor is position-controlled along constant-velocity trajectories spanning the entire rotation range of the transmission, $-65° \leq \theta_m \leq 65°$; the velocity is increased at each repetition from 0.1 rad/s to 3 rad/s. With reference to the control scheme represented in Fig. 4.2 (right), the commanded torque T_a required to follow the trajectory is shown by the blue line in Fig. 4.10 (top-left). At low speeds, small jumps when reversing the rotation direction reveal the presence of a constant frictional contribution, while the linear trend over constant-velocity strokes highlights some weak spring-rate effect generated by the membranes. At higher velocities, instead, the viscous quadratic contribution becomes predominant. The commanded torque is also plotted with respect to the angular position, Fig. 4.10 (center), and to the angular velocity, Fig. 4.10 (right), for a better visualisation. This combination of effects is characterised by fitting the model (4.28) to the experimental data.

$$\begin{aligned}\tilde{\tau}_f(\theta_m, \dot{\theta}_m) = \tilde{\tau}_v(\dot{\theta}_m) + \tilde{\tau}_s(\theta_m) + \tilde{\tau}_u(\dot{\theta}_m) = \\ = c_f|\dot{\theta}_m|\dot{\theta}_m + s_f(\theta_m - \theta_f) + b_f\mathbf{sign}(\dot{\theta}_m)\end{aligned} \tag{4.28}$$

The model includes the quadratic viscous contribution $\tilde{\tau}_v$, the spring-rate contribution $\tilde{\tau}_s$, and the constant contribution $\tilde{\tau}_u$. The fitting result (corresponding to the selection of the free parameters: $c_f = 0.21$ Nm s^2/rad^2, $s_f = 0.28$ Nm/rad, $\theta_f = 0.047$ rad, $b_f = 0.28$ Nm) is shown by the black dashed lines in Fig. 4.10. An effective compensation of the friction torque $\tilde{\tau}_f$ is achieved by adding the term T_f, defined as follows, to the torque reference commanded to the motor driver

(see again the control scheme in Fig. 4.2)

$$T_f = k_v\tilde{\tau}_v + k_s\tilde{\tau}_s + k_u\begin{cases} \omega\dot{\theta}_m & |\omega\dot{\theta}_m| \leq |\tilde{\tau}_u| \\ \tilde{\tau}_u & else \end{cases}, \tag{4.29}$$

where the piecewise function prevents the intermittent activation of the $\tilde{\tau}_u$ compensation term for small velocity fluctuations measured by the encoder, and gains k_v, k_s, and k_u assume values in the interval $(0, 1)$, and are tuned in order to modulate the compensation action. Results in Fig. 4.10 (bottom-left) show that the torque input T_a needed to track the same characterisation trajectory after applying the friction compensation; the strategy reveals effective, especially at high velocities.

Chapter 5

Series Elastic Ankle Actuation for Hopping Legged Robot

Lightweight legs and intrinsic series-elastic compliance have proven to be the key features for robust and energy-efficient locomotion in legged robots. In animals series-elastic actuation of distal limbs is achieved by muscle-tendon units and their locomotion capabilities emphasize the importance of lightweight, compact and compliant legs. So far no designs are available that feature all characteristics of a perfect distal legged locomotion actuator; a low-weight and low-inertia design, with high mechanical efficiency, no stick and sliding friction, low mechanical complexity, high-power output while being easy to mount. Ideally, such an actuator can be controlled directly and without mechanical cross-coupling, for example remotely. With this goal in mind, a low-friction lightweight Series ELastic Diaphragm distal Actuator (SELDA) is proposed to meet many, although not all, of the above requirements. A bioinspired robot leg that features a SELDA-actuated foot segment is developed, implemented and characterised. Two leg configurations are compared and controlled in agile forward hopping by a central pattern generator. By tuning SELDA's activation timing, the robot's hopping height is adjusted by 11% and its forward velocity by 14%, even with comparatively low power injection to the distal joint.

5.1 Overview

In this chapter a legged robot with distal actuation is developed and characterised; the ankle actuator is placed into the robot's trunk, while power is transmitted remotely, efficiently, and in an uncoupled manner. Placing heavy actuators close to the trunk leads to low-mass and low-inertia legs, which are well suited for agile and dynamic locomotion, and simplifies legged robot control [73]. Control and design complexity increase in robotic legs that feature more than two actuated segments, where the actuation is transferred over multiple joints. Multi-joint transmission can be achieved with cable (tendon), chain, and belt systems [74–76], but simple configurations lead to mechanical coupling, where the output of one motor affects the movement of several, in-between connected joints. Decoupling mechanisms are either based on sensory feedback and kinematic control or complex mechanical solutions [74, 77]. Fully-remote actuation bypasses joints by transmitting power directly into the target location; Bowden cable and fluidic transmissions (hydraulic or pneumatic) are two common examples [78]. Power transfer is well

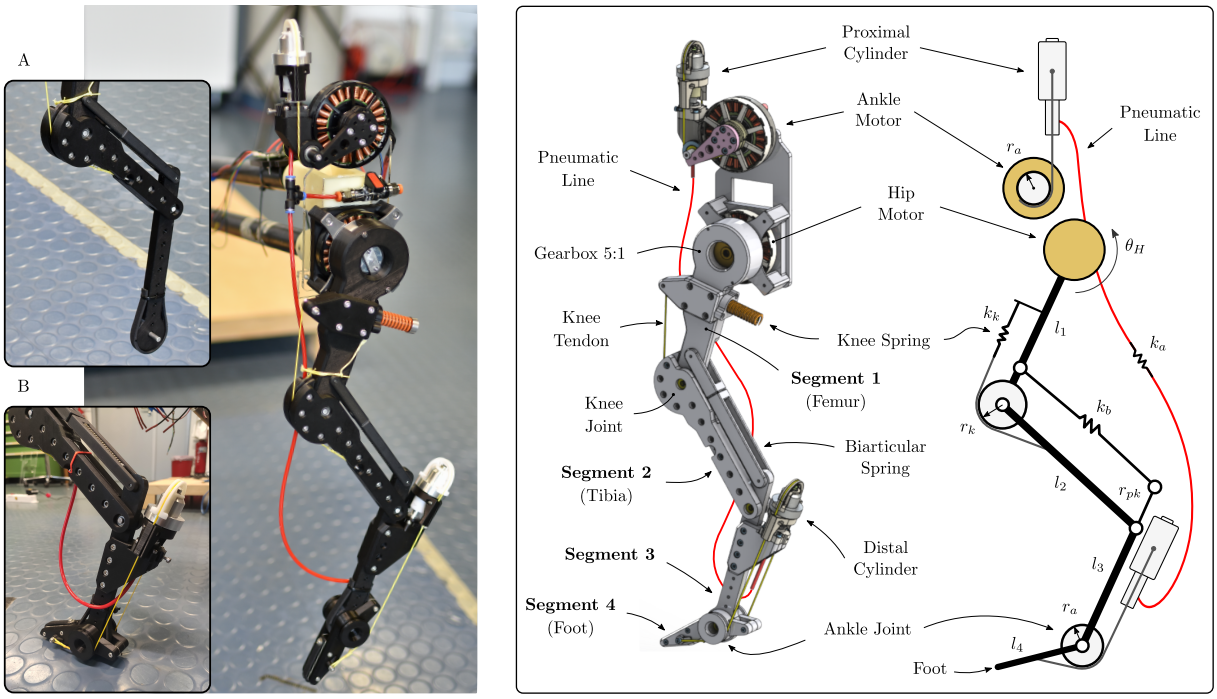

Figure 5.1: *Left:* Experimental prototype of the bio-inspired leg and details of the two configurations compared in this work. *Configuration-A:* traditional bio-inspired layout [72]. *Configuration-B:* novel configuration with 'foot' segment remotely actuated by a compliant pneumatic transmission. *Right:* schematic drawings of the experimental prototype.

tested in case of Bowden cables, especially for lower frequency applications [79], however, high friction between the core cable and outer sheath leads to power losses that are prohibitive for locomotion frequencies above $f = 3\,\text{Hz}$. Alternatively, industrial hydraulic actuators have been used in legged robots [80, 81]. Hydraulic actuators determine a compromise between their maximum working pressure and the fit between the seal, the piston, and the cylinder. High output force and power can be produced with high input pressure, but high-pressure actuation requires tight seal fits that increase friction and power losses. Conversely, low-friction cylinders generally reduce maximum working pressure [82, 83]. Rolling diaphragm transmissions have the potential for remote and non-coupled actuation of distal joints of robotic legs, providing high efficiency, stiffness and backdrivability features. Their mechanical transparency allows precise torque control and determines a suitable base for advanced controller design. This favourable set of characteristics make hydrostatic transmissions a suitable technology for the remote actuation of lightweight robotic legs.

Animals show agile, robust, and energy-efficient locomotion based on series elastically actuated structures embedded in their multi-segment legs. Notably, the distal muscle-tendon structures tend to store more elastic energy than proximal structures [84]. This motivates the development ankle actuation systems, which allow building robotic legs that mimic the behaviour of animal legs. In robots, distal leg joint actuation is often avoided. Combining high ankle output power and series elastic features is possible [85, 86], but powerful geared electric motors come with high mass and they are energetically costly to be accelerated and decelerated through leg swing. Mechanical wobbling in the transition between swing and stance phases also complicates sensing and control [87]. Pneumatic artificial muscles (PAMs) are well-working, lightweight examples

Table 5.1: Robot design parameters.

Parameters	Symbol	Value
Robot mass (configuration A)	m_A	1.05 kg
Robot mass (configuration B)	m_B	1.20 kg
Leg resting length	l_0	408 mm
Segment 1 length	l_1	150 mm
Segment 2 length	l_2	150 mm
Segment 3 length	l_3	140 mm
Segment 4 length	l_4	70 mm
Knee spring pulley radius	r_k	30 mm
Bi-articular insertion radius	r_{pk}	32 mm
Ankle pulley radius	r_a	15 mm
Knee spring stiffness	k_k	10.9 N/mm
Bi-articular spring stiffness	k_{b}	9.8 N/mm
Ankle stiffness (air spring)	k_a	0.2 Nm/rad

for remote actuation with high force and power output [88]. However, they are actuated against the strain of their rubber-like bladder actuator, which decreases efficiency and increases control complexity [89].

In this chapter, a **S**eries **EL**astic **D**iaphragm for distal **A**ctuation (SELDA) is developed. SELDA is inspired by the omnipresent series elastic actuation (SEA), especially in the distal animal leg [90]. The SELDA system aims to develop hardware for agile legged hopping that is easy to control, is uncoupled from neighboring joint's movements and loads, is easy and flexible to mount, features a remote motor placement and a distal power output, is distally lightweight, inherently compliant, and mechanically efficient. A lightweight bio-inspired leg with a remotely actuated foot segment is built and experimentally characterised. The foot's actuator is placed in the robot's torso and its torque is reflected at the foot joint using a pneumatic rolling-diaphragm transmission, with compliance characteristics well suited for legged hopping. Results also present a comparison of hopping performances between different leg configurations, Fig. 5.1 (left): configuration-A is a leg without a foot segment, similar to previous work [72], while configuration-B is a leg with a foot segment, actuated by SELDA.

5.2 Robot Design

The robot leg with its SELDA-actuated ankle is presented in Fig. 5.1. It weighs 1.2 kg and it features two electric motors located in the robot torso. The hip motor is the main actuation of the robot and it drives the femur segment through a 5:1 gearbox, swinging the leg forward and backward. The ankle motor is connected to the proximal cylinder of the SELDA system that transmits the actuation input to the distal cylinder by compressing the air in the pneumatic line; the distal cylinder then actuates the ankle joint. The SELDA ankle actuator is expected to input mechanical power both during forward and vertical motion. The leg features four segments; segments 1, 2 and 3 are arranged in a bio-inspired pantograph configuration (similar to [72]),

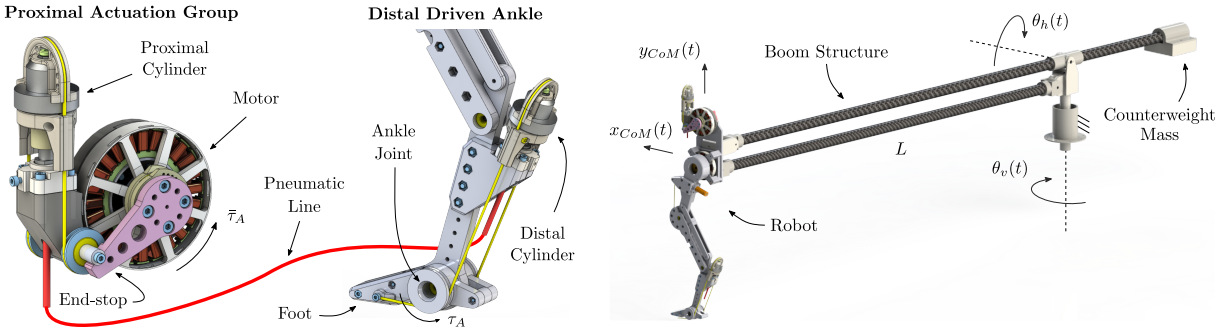

Figure 5.2: *Left:* CAD picture of the SELDA rolling diaphragm transmission actuating the ankle joint remotely. *Right:* experimental configuration for hopping experiments in which the leg is mounted on the boom.

while segment 4 is the remotely-actuated foot used for enhanced control of the interaction with the ground. The pantograph is fully passive and its stiffness properties are defined by knee and biarticular springs: the knee spring, with stiffness k_k, extends the segment 2 by acting on the knee cam, while the biarticular spring, with stiffness k_b, acts over two joints. Also the ankle joint is characterised by intrinsic stiffness k_a, determined by the compliance of the air volume; k_a is the series-elastic stiffness between ankle motor and ankle joint. Intrinsic elasticity make the compliant under-actuated robot leg storing elastic energy during deceleration and releasing it in the form of kinetic energy while accelerating the robot in the second half of stance phase. Robot design parameters are listed in Tab. 5.1.
In this work, the robot leg is minimally instrumented so as to prove robust locomotion by means of simple control with feedforward reference trajectories; only positions and torques of the two actuators are sensed by the motor drivers. Moreover, the minimally-instrumented setup allows comparing leg configurations and their locomotion patterns fairly.

5.2.1 Diaphragm pneumatic transmission

The proposed concept of pneumatic transmission is employed to implement a series elastic diaphragm for distal actuation (SELDA) which integrates the functionalities of remote actuation and series-elastic actuation in a single lightweight, efficient and compact device. A detailed scheme of the SELDA system is offered in Fig. 5.2 (left). Efficient and transparent torque reflection is achieved by using virtually frictionless pneumatic cylinders based on DM3-20-20 rolling diaphragms by Fujikura Composites (268.8 mm^2 effective area, 24 mm full stroke, 20 mm cylinder radius). Positive torques $\bar{\tau}_A$ generated by the motor cause the proximal cylinder to compress and the air pressure to increase. The pressure propagates through the pneumatic line and pushes the distal cylinder in the direction of expansion; a positive torque τ_A is therefore generated at the ankle joint, making the foot tip pushing the ground. The coupling between cylinder displacement and joint or motor rotation is implemented with tendons made of dyneema running on pulleys with radius $r_a = 20$ mm. An angular rotation range of $90°$ is then established at the motor and at the ankle. To minimize weight, the SELDA layout takes advantage of the asymmetrical torque requirements of locomotion at the ankle joint: large torques are required in the direction of the push off (positive direction of rotation in the picture), and very small torques are required to flex the foot during the swing phase. According to this consideration, the proposed SELDA system is conceived as a single-acting device, able of transmitting forces to the ground in the direction

of the push-off only. The retraction of the foot is not implemented and it is actuated passively during the touch-down phase as result of the robot inertia landing on the ground. This requires a single pneumatic cylinder placed in distal position, where mass reduction is critical; one single cylinder is also placed in the proximal actuation group.
The desired value of transmission stiffness of the SELDA system is achieved by pre-pressurizing the air volume; in this work, an initial pressure $p_0 = 0.1$ MPa is selected. When the system is at rest (foot completely extended and inactive motor), the transmission applies an offset torque of 0.4 Nm at ankle and motor axes due to its pre-pressurization, while it reacts to the rotation of its ends (motor and ankle axes) as a spring of stiffness k_a (experimentally characterised in Sect. 5.3). The mechanism is designed to generate a foot-tip force in the range from 7 N (passive configuration) to 14 N (active configuration, proximal cylinder fully compressed) at the end of the stance phase (flexed foot) and a force in the range 5 N to 10 N during push-off (extended foot). The range of forces achievable by the SELDA system well explain our intention to obtain an under-dimensioned ankle actuation by limiting the ankle's cam size: the foot is not supposed to sustain the weight of the robot, which lean on the heel during stance phase, as many runners do in nature, but it is required to alter the timing of the energy transfer to ground during push-off. The foot is the last segment to lift off the ground and even small forces exchanged during this phase are expected to effectively alter the jumping dynamics, observing changes in forward speed and hopping height.

5.2.2 Bio-inspired leg design and details

The pneumatic tendon-like transmission is implemented in a bio-inspired complaint robotic leg. Inspired from [72], this leg includes four segments and three passive elastic elements that mimic the compliant behavior of mammalian quadruped's leg. The hip and the ankle joints are actuated by means of brushless motors (model NM7005 KV115 by *T-Motor*, with 1.3 Nm maximum rated torque). The hip motor is equipped with a 5:1 planetary gearbox (model RS3505S, *Matex*). The motor positions are measured by rotary encoders (model AEAT8800-Q24, *Broadcom*, 12 bit)). We use open-source drivers (Micro-Driver, [91]) for motor control, current sensing, and encoder reading. The Micro-Driver board is capable of dual motor Field Oriented Control (FOC) at 10 kHz. We implemented our controller on a single board computer (3B+, *Raspberry Pi Foundation*) with control frequency of 1 kHz. The proximal module for ankle actuation is mounted above the hip and it is connected to the distal diaphragm cylinder through a 5 mm polyurethane pneumatic hose. The knee joint is coupled to the knee spring (model SWS14.5-45, *MISUMI*, $k_\mathrm{k} = 10.9\,\mathrm{N/mm}$) that extends the knee to resting angle of $\alpha_0 = 130°$. In parallel to the shank segment, a spring-loaded (model UBB10-60, *MISUMI*, $k_\mathrm{b} = 9.8\,\mathrm{N/mm}$) biarticular segment replicates a pantograph kinematics. This segment replicates the lower leg muscle-tendon apparatus of gastrocnemius muscle and Achilles tendon. Details of design parameters can be found in Tab. 5.1.

The hip of the robot is mounted to the boom structure, Fig. 5.2 (right), which allows the robot to jump along a circular path over long distances. The boom prevents torso rotation, eliminating the need for trunk pitch control. The length of the boom rods L is 1.55 m determining a travelled distance of 9.73 m over one entire revolution. We connected a counterweight at the opposite end of the boom that balances the own mass of the boom, so that the robot does not undergo

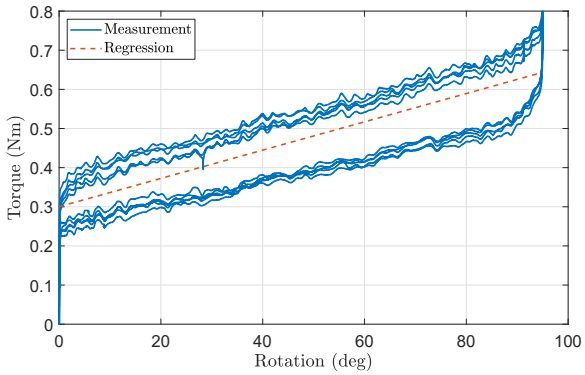

Figure 5.3: Stiffness characterization of the SELDA system. The y-axis measures the torque manually applied at the proximal rotation axis and the x-axis measures the corresponding rotation. The output side is fixed. Estimated stiffness of 0.15 Nm/rad from the proximal cylinder side.

additional weight. The boom rotation angles θ_h and θ_v are measured by two rotary encoders (model 102-V, *AMT*, 11 bit). The position of the robot center of mass (CoM) x_{CoM} and y_{CoM} are evaluated as function of θ_h and θ_v angles.

5.3 Transmission Stiffness Characterization

The air spring feature of the transmission adds compliance to the distal joint. Compliance is therefore characterized in terms of transmission stiffness in Fig. 5.3. The transmission is pre-pressurized to 0.1 MPa, the foot is consequently fully extended, and a full-stroke rotation is applied to the motor. We manually rotated the rotor with an instrumented lever arm equipped with a load cell (model 3133_0, *Phidgets*) at its extremity for accurately measuring the applied torque. We measured a transmission stiffness of 0.2 Nm/rad. Notice that the initial jump in the plot indicated the torque needed to counteract the torque produced by the pre-pressurization p_0.

5.4 Hopping Experiments

This section describes the hopping experiments. Sect. 5.4.1 described the experimental configuration chosen for gait analysis; Sect. 5.4.2 compares the performance of the leg with and without the distal segment, i.e. configurations-A and -B in Fig. 5.1 respectively; Sect. 5.4.3 presents our first investigation of the effect of distal actuation, mainly focusing on the kinematic effects in terms of gait velocity, step length and step height. A typical gait obtained during the experiments with SELDA system is shown in Fig. 5.4.

5.4.1 Experimental Configuration

The robot response is characterized in case of simple control strategies in order to emphasize intrinsic self-stabilizing response through compliant design. The hip joint is position controlled along a sinusoidal trajectory:

$$\hat{\theta}_H = Asin(2\pi f) \tag{5.1}$$

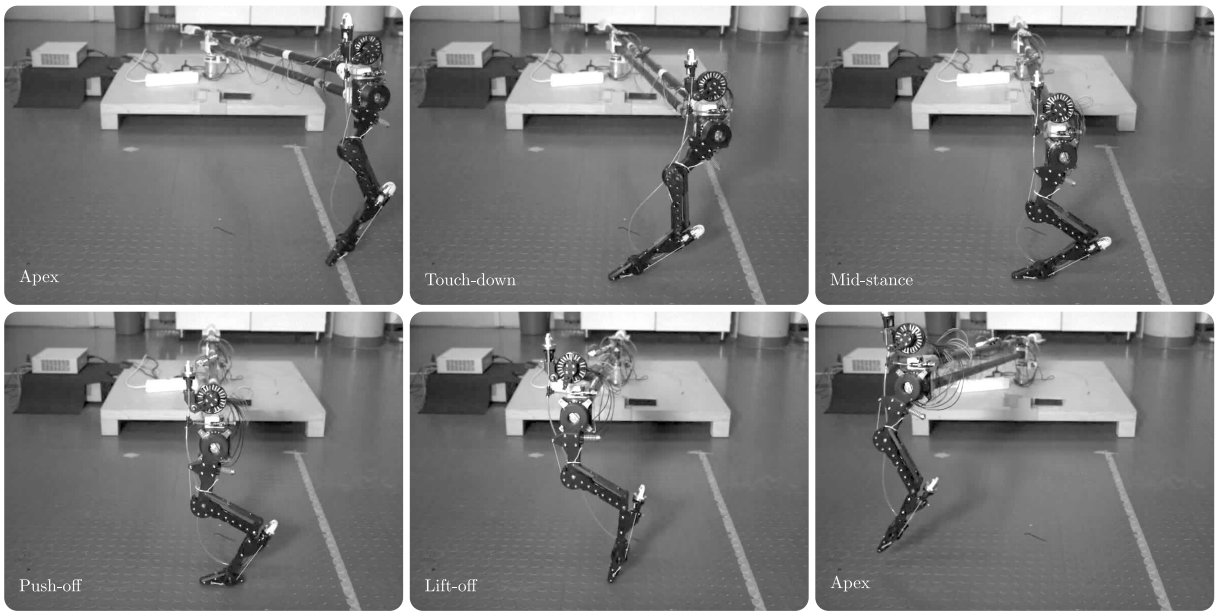

Figure 5.4: Gait cycle snapshots from apex to apex, taken from high-speed video footage. A *delay* was programmed to trigger push-off actuation. Step cycle time ($T = 1/f$, f is frequency) is 606 ms, or around 1.65 Hz hopping frequency.

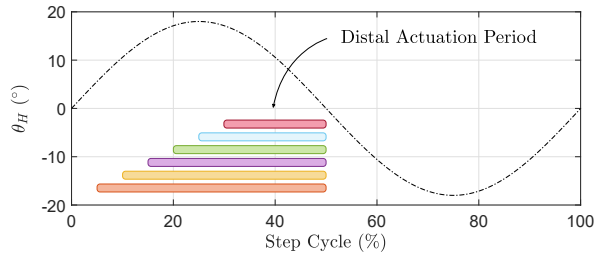

Figure 5.5: Distal actuation timing with respect to the hip reference trajectory (black dashed line). The colored rectangles indicate the period of distal actuation. Different initial timing t_T values are considered: $t_T = 5, 10, 15, 20, 25, 30\%$ of the step cycle; distal actuation is then ended at 50 % of the step cycle, during the swing phase. According to scheme in Fig. 5.1, positive angles indicate a leg position behind the vertical axis.

where constant A is the hip trajectory amplitude and constant f defines the hopping frequency. Hip oscillation amplitude $A = 18°$ and locomotion frequency f = 1.65 Hz are common for all of our experiments. Note that the chosen parameter set is likely not optimal for both configurations; we expect that each configuration has its dynamics. Nevertheless, we keep the parameter common for a consistent comparison between leg configurations. An example hip trajectory is shown in Fig. 5.5. The trajectory tracking is performed through a PD controller:

$$\tau_H = k_p e(t) + k_d \dot{e}(t) \tag{5.2}$$

where τ_h is the commanded torque to the hip joint and variable $e(t)$ is the tracking error $e(t) = \hat{\theta}_H - \theta_H$. The controller Eq. (5.2) behaves like a virtual spring-damper element acting between the reference trajectory $\hat{\theta}_h$ and the hip joint with stiffness value k_p and damping coefficient k_d. Parameters $k_p = 40$ and $k_d = 0.35$ are fixed for all experiments.

To investigates the influence of the distal actuation, we focus on the actuation timing of the foot segment during the step cycle. A step torque reference of 1 Nm is commanded to the ankle

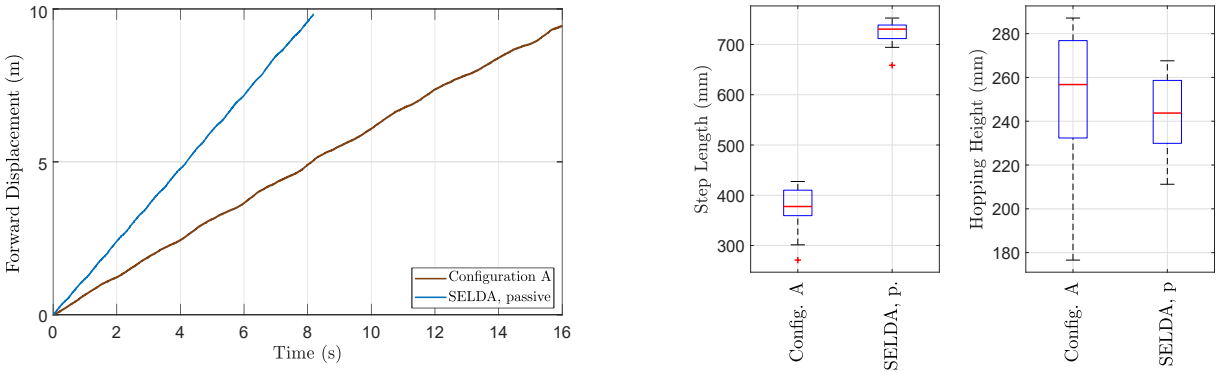

Figure 5.6: Performance comparison between configurations-A and -B, (Fig. 5.1); in this experiment the distal segment is not actuated and the pneumatic transmission behaves like an air spring. *Left* time taken to travel a complete turn around the boom. *Center:* statistical analysis of the maximum step height over one full boom revolution. *Right:* statistical analysis of the step length over an entire revolution.

motor: the initial actuation instant varies in the range 5 % to 30 % of the step cycle, as shown by the colored bars in Fig. 5.5; the ankle actuation is then ended at 50% of the step cycle, during the swing phase when the leg is not in contact with the ground. The compliance feature of the pneumatic transmission allows driving a simple step torque-reference to the ankle motor so that we can focus on analyzing the influence of actuation timing only.

5.4.2 Analysis of Passive Foot

In this section, leg configuration-B is tested in passive mode, i.e., without activating the ankle motor, and its performance is compared to configuration-A in order to assess the benefits of the additional compliant foot. Fig. 5.6 shows this comparison evaluated on data sets corresponding to a complete revolution of the circular trajectory around the boom. The top plot shows that the distance of 9.7 m is travelled in 15.7 s by robot configuration-A and in 8.1 s by the configuration-B in SELDA passive mode.In this experiment, SELDA increases the forward velocity $\dot{x}_{CoM}$ from 0.62 m/s to 1.20 m/s; an almost two-fold increase. The higher-speed locomotion is also visible in terms of step length, Fig. 5.6 (bottom-left), which increases of 93 % from 378 mm to 730 mm. The foot slightly affects the robot's maximum hopping height (Fig. 5.6, bottom-right), but it leads to a more repeatable hopping height and more stable hopping motion.

5.4.3 Analysis of Active Foot

This section investigates the effect of the SELDA activation timing, also in comparison with the passive foot configuration. The initial timing t_T of the ankle actuation varies in the range 5 % to 30 % of the step cycle; a timing of 5 % means that the ankle is actuated right after the touch-down, while a timing of 30 % means that the ankle is actuated right before the lift-off. Fig. 5.7 (left) shows that, in general, the center-of-mass velocity $\dot{x}_{CoM}$ can be increased by activating the ankle after mid-stance, while it is slowed down by actuating the ankle before mid-stance. In particular, the active SELDA achieves the highest forward velocity of 1.30 m/s with an actuation timing of $t_T = 20\,\%$ versus a speed of $\dot{x}_{CoM} = 1.20$ m/s for the passive SELDA. The lowest performance is observed with an actuation timing of $t_T = 15\,\%$ leading to an average forward

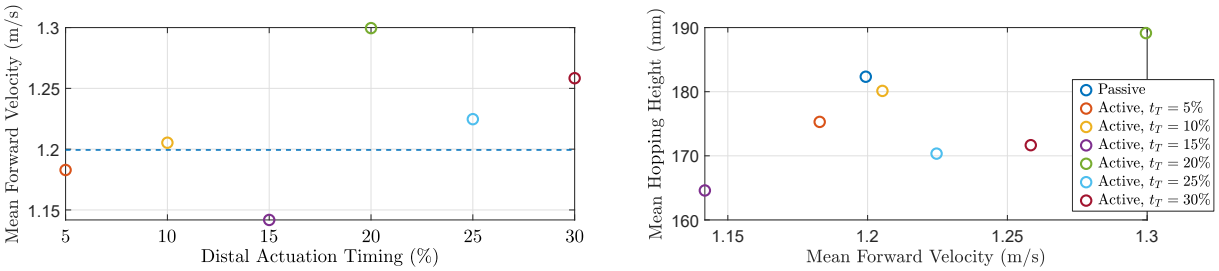

Figure 5.7: Investigation of the effect of different distal actuation timing t_T. *Left:* mean velocity of the center of mass achieved for different values of timing t_T. *Right:* mean step height with respect to mean forward velocity. Step height is the difference between the highest and the lowest vertical position of the robot's center of mass at each step. Mean values refer to the dataset corresponding to one full revolution around the boom (9.7 m travelled distance) during steady state locomotion.

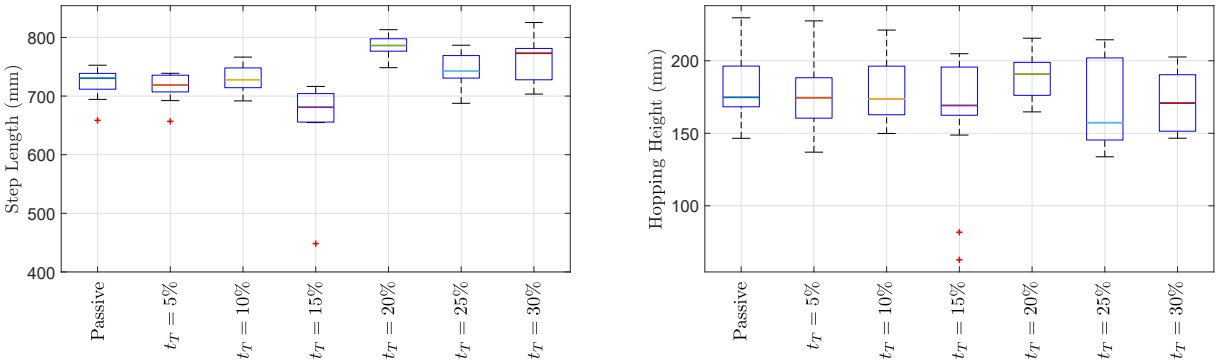

Figure 5.8: Box plot statistical representation of the influence of distal actuation timing t_T on step length and maximum step height. The dataset of this analysis corresponds to samples collected during one full revolution around the boom in steady state gait. The minimum number of steps for one revolution is 13.

speed of $\dot{x}_{CoM} = 1.14\,\mathrm{m/s}$. Fig. 5.7 (right) illustrates the energy transfer between hopping height and forward velocity $\dot{x}_{CoM}$. Hopping height is calculated at each step as the difference between the highest and the lowest vertical position y_{CoM} reached by the robot's center of mass. By tuning the activation timing, we can effectively adjust the hopping height by 11 % and the forward velocity by 14 %. Note that our diaphragm actuation produces a torque of (≈1 Nm) from the motor side, which also compensates for the internal pressure of the pneumatic line. Albeit the limited actuator output torque, we observe that locomotion speed and hopping height are effectively altered (Fig. 5.7, left and right).

We quantify the activation timing effect with step length and hopping height over steps (Fig. 5.8). Narrow bands in the box plot indicates more stable hopping gait. We observed period-2 hopping in some experiments, which expand the confidence internal in the plot. If gait parameters such as frequency and amplitude are tuned to match the robot's own dynamic, we expect to further reduce variation of step length and hopping height between steps.

5.5 Discussion

This chapter proposes distal actuation of the foot segment in a bio-inspired hopping robot with a compliant rolling diaphragm pneumatic transmission. Diaphragm actuation has appealing fea-

tures of lightweight, low-friction, high efficiency, and truly remote actuation. Self-stabilizing gaits are found with comparatively simple, open-loop position control. Results show that the addition of the foot segment improves the locomotion performance of the robot, already in its passive elastic mode, with an increase in forward velocity of 93 %. With the actuated foot, actuation timing effectively influences the hopping gait. By tuning the ankle actuation timing from 5 % to 30 % of the gait cycle, results reveal 11 % change in hopping height and 14 % in forward velocity, with its currently under-dimensioned actuator. Based on these first results, future developments will focus on providing the proximal cylinder with an antagonistic action to reduce the actuation effort that is required to balance the hose's internal pressure. An additional gearbox mounted to the ankle motor will increase output torque at reduced electrical power requirements. Note that the proposed experiments are not based on optimal control strategies and SELDA system may potentially achieve higher performances. Gait patterns will be optimized for energy-efficient and agile locomotion, by tuning control parameters and type, and by introducing online feedback.

Chapter 6

Adaptable-Damping Hydrostatic Transmission

This chapter presents a simple yet effective strategy to implement the *adaptable damping* feature in hydrostatic transmissions. The proposed strategy allows the transmission to adjust its damping coefficient in real time from the nominal value of the standard non-adaptable transmission to virtually infinite values, i.e. locked mechanism. This last configuration also illustrates the possibility of implementing a safety braking system. The next sections provide a review of the existing variable damping mechanisms, describe the scheme of the adaptable-damping hydrostatic transmission, and finally discuss some preliminary experimental results. The problem of defining a proper control strategy has not been addressed yet.

6.1 Overview

Traditional stiff and non-backdrivable industrial robots exhibit improved precision, accuracy and bandwidth, but they result inherently unsafe because of their large mechanical impedance. *Mechanical impedance* is the differential dynamic relation that describes the generation of force as function of the displacement: stiffness relates the infinitesimal differences in force and position, while damping relates the infinitesimal differences in force and velocity. These quantities rule the processes of elastic energy storage and irreversible energy dissipation, respectively. Therefore, mechanical impedance describes how the energy is transformed, stored or dissipated in mechanical systems during functioning and interaction.

New classes of compliant robotic actuators have been conceived to mimic the efficiency of biological systems, which, for instance, continuously store and release energy in form of potential elastic energy in muscles and tendons during walking, running and jumping. When a deformable element is present in mechanical systems, this energy flow becomes relevant and it can be exploited to execute efficient and dynamic movements, as well as to safely navigate in unknown environments, where impacts and unexpected contacts may happen.

The possibility of modulating the mechanical impedance of robotic systems offers even more promising and versatile perspectives, where a low-stiffness low-damping setting may be desired when performing fast movements in efficient and safe manner, while a high-stiffness high-damping configuration may be preferable when performing precise positioning tasks, as humans

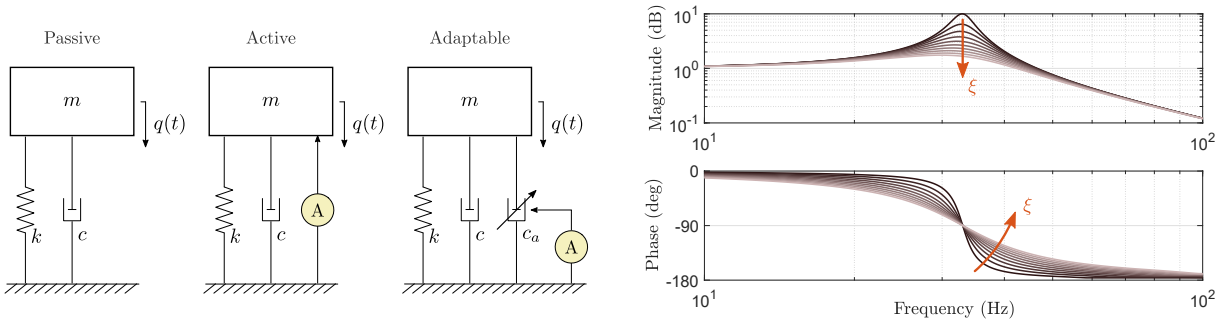

Figure 6.1: *Left:* scheme of passive, active and adaptable physical systems. In passive systems physical impedance is fixed, in the passive system a dissipative action in injected by the actuator A, and in adaptable systems the actuator A adjusts the damping coefficient c_a of the physical damper. *Right:* effect of different values of modal damping on the second order dynamics associated with schemes in Fig. 6.1. The transfer functions are assumed from input to output torques, consistently with nomenclature of Eq. (3.2) in Chapter 3.

do. Moreover, when controlling robotic legs, relatively high damping may be desirable to avoid chattering between foot and unstructured stiff terrain, but its value should be minimized once the ground contact is stable in order to conserve and store energy in elastic elements, so that an efficient walking can be generated [92].
Active impedance actuators, in which traditional stiff hardware (i.e. highly geared electric motors) is used and virtual compliance is simulated through software, has proven versatile for a wide variety of undemanding tasks, but severe weaknesses arise when addressing challenging applications in terms of bandwidth limitation, impossibility to store energy, and stability dependency on the particular load condition (see next section for more details).
Adaptable strategies, instead, achieve variable impedance by actually changing the physical parameters of the system. Novel *Variable Impedance Actuators* (VIA) are rapidly developing in order to create a new generation of robots that can co-operate and co-exist with people, getting closer to human abilities of manipulation and locomotion [16]. A VIA is no more a position source, but it defines an equilibrium position from which the actuator deviates according to the external forces and the mechanical properties of both the surrounding environment and the actuator itself. An adaptive behaviour is not only consequence to control and computation but it arises from the complex physical interaction between the environment and the robot morphology, actuation and sensing properties. Yet, controlling impedance is a well-posed problem in an unstructured interactive scenario, since the controller parameters do not depend on the unknown environment.

6.1.1 Adaptable Damping: Motivations

Even if variable impedance is still an open question, a lot of work has been done in designing variable stiffness mechanisms in literature, while few strategies has been addressed to implement physical variable damping. A reason may consist in the difficulty of obtaining an adaptable source of energy dissipation with a suitable range of generated forces and response linearity. The most commonly adopted strategy to implement variable damping, even in advanced robotic systems where stiffness can be physically adjusted, is still via software, Fig. 6.1 (*active*). This versatile and easy-to-use strategy, defined as *active damping*, has however several drawbacks. Active strategies intrinsically suffers from bandwidth limitations of actuators and software, reveal-

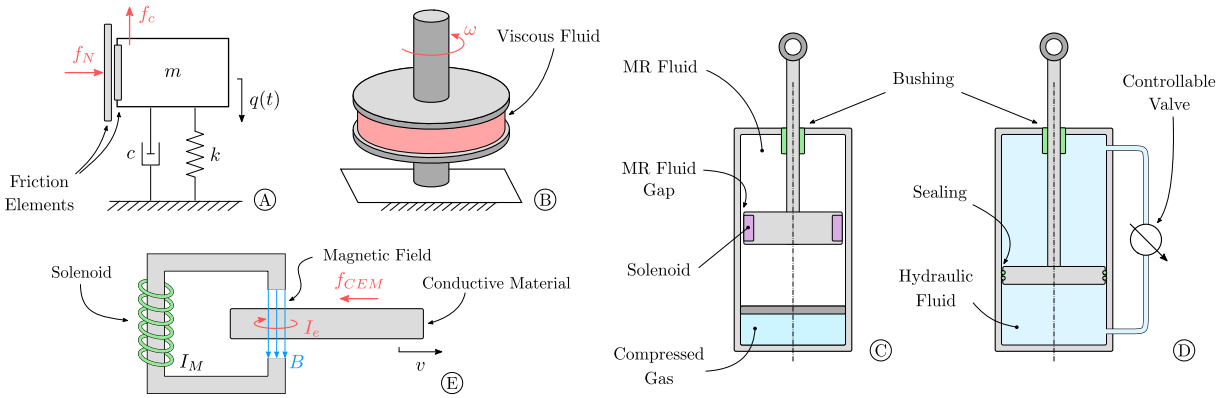

Figure 6.2: Most common adaptable-damping mechanisms. *A*: Friction Dampers (FD); *B*: Linear Fluid Dampers; *C*: Electrorheological (ER) magnetorheological (MR) dampers; *D*: Quadratic Fluid Dampers; *E*: Eddy current dampers.

ing ineffective at frequencies above the closed-loop bandwidth. This also implies that the infinite range of virtual damping coefficients that software can theoretically emulate does not extend to real-life scenarios, where some stability limitations arise. In addition, active control usually requires considerable actuator effort and a substantial energy consumption to produce suitable dissipation forces. A physical damper, instead, exhibits infinite bandwidth and is able to compensate for high frequency oscillations caused by lightweight links, stiff transmission systems, and impacts with surrounding obstacles. When the control action is used to adjust the damping coefficient of a physical damper, the passivity of the dynamical system always holds and instability never takes place, Fig. 6.1 (*adaptable*). Adaptive damping has also interesting influence on the stability limits of closed-loop systems, both torque-controlled and position-controlled ones. This can be illustrated by the frequency response of a simple second-order dynamical system, Fig. 6.1 (right): increasing levels of damping reduce the resonance peak magnitude and also determine a smoother transition in the phase plot. The phase plot of lightly damped systems undergoes sharp phase lag at the resonance frequency, and placing the closed-loop bandwidth of similar systems above the resonance frequency is generally difficult, as testified by the maximum torque-control bandwidth achieved in Chapter 3; also, this is often the case of efficient variable-stiffness actuators conceived for walking robots, where the inherent compliance moves the resonance towards low frequencies and compromises the achievable bandwidth. On the other hand, additional physical damping acts as a phase lead after the resonance frequency and increases the phase margin of the closed loop when feedback control is applied. Thus, adaptable mechanisms can set appropriate levels of damping as function of the operating frequency, including the possibility of setting to zero the dissipative action for efficient cyclic or low-frequency tasks.

The need for disabling the dissipative action is crucial and it certainly represents a difference between adaptable damping and adaptable stiffness; while some level of inherent compliance is accepted in variable stiffness mechanisms, a residual damping action in adaptable damping mechanisms would represent a constant source of dissipation and it would prevent efficient functioning.

Fig. 6.2 shows the most common adaptable-damping mechanisms. Friction dampers (FD), Fig. 6.2 (*A*), achieve dissipation through friction, where the control action modulates the normal

force f_N applied between two sliding parts, placed on the stator and the rotor of the actuator, respectively. As dry friction is of no practical interest, any kind of linear or nonlinear viscous damping can be physically emulated by properly modulating the normal force f_N; this mechanism has the peculiar and useful capability of generating high forces at low velocities. The challenge is therefore the control of friction to obtain the desired viscous response, getting through complex friction models, wear, hysteresis and response irregularities produced by the static friction band [93].

Electrorheological (ER) and magnetorheological (MR) dampers, Fig. 6.2 (*C*), similar to common hydraulic dampers where viscous effects are generated by fluid flowing through a small gap, use particular fluid whose viscosity depends on the electric and magnetic field, respectively; adaptable damping is therefore achieved by modulating the electric of magnetic field. This kind of actuators produce a wide range of damping coefficients but they generally suffer from high hysteresis [93]. MR-dampers have been used in general-purpose high-performance physical interaction robots [94], to avoid chattering between ground and feet of heavy-duty quadrupeds [92], and, in combination with variable stiffness actuators, to generate novel walking strategies for efficient quadrupeds [95]; ER-dampers have been successfully used to build MRI/fMRI compatible medical robots [96] and to increase the position-control precision of traditional industrial robots by suppressing the high-frequency oscillations originated by stiff gearboxes and links [97].

Fluid dynamics dampers, Fig. 6.2 (*D*), are again based on the viscous action produced by fluid flowing through small gaps: standard hydraulic fluid is used and adaptable behaviour is achieved by modulating the area of the gap by means of controllable valves. Such actuators are also called *Quadratic Dampers* because of the quadratic dependency between force and velocity that typically takes place in turbulent flow through small orifices (high Reynolds number). Such a quadratic-response is capable of generating high damping only for large oscillations, but it is typically affected by small-amplitude residual oscillations. This issue is solved by *Linear Dampers*, Fig. 6.2 (*B*), characterised by laminar flow. The damping force is proportional to the speed gradient in the fluid layer and suitable forces are produced also for small-amplitude oscillations or low velocities. The damping coefficient depends on the fluid surface area, the height of the fluid layer and the fluid viscosity; adaptable behaviour is therefore implemented by controlling the surface area [98] or the height of the fluid layer.

Finally, eddy current dampers (ECD), Fig. 6.2 (*E*), generate a viscous damping action proportional to the velocity of a conductive part moving through a magnetic field. The eddy current generation causes the vibration to dissipate through Joule effect, heating the conductor parts [99]. ECDs can be realized with both electromagnets or permanent magnets. The adaptable response is achieved by modulating the intensity of the magnetic field [100] in the first case, and by modifying the geometry of conductor and magnets (i.e. shape or gap) [101, 102] in the second case.

6.2 System Design

This chapter proposes a novel architecture to easily enhance hydrostatic transmissions with the adaptable-damping feature. Hydrostatic transmissions are transparent systems that exhibit inherent highly oscillatory response; hydrostatic technology rapidly gained visibility for its lightness and backdrivability, and the adaptable-damping feature would offer stronger motivations for its

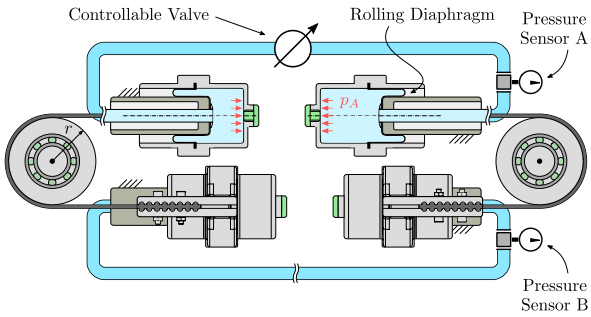

Figure 6.3: Scheme of the adaptable-damping hydrostatic transmission.

application in human-robot-interaction and legged robotic scenarios.
A quadratic damping strategy can be easily implemented in hydrostatic transmissions by simply including a controllable valve in the existing fluid lines, as shown in Fig. 6.3. Even if the previous section highlighted the issue of residual small-amplitude oscillations associated with quadratic damping, the choice of implementing the adaptable behaviour through a controllable valve is justified by simplicity, robustness and cost-effectiveness of the resulting mechanism. Furthermore, the issue of small-amplitude residual oscillations may be considered a marginal problem by the human-robot-interaction point of view, which is the focus of this thesis, and it may be compensated by little control actions that require low actuator effort. Additionally, the controllable valve implements an emergency brake when completely closed, which is a relevant feature for collaborative or medical applications. On the contrary, when the valve is completely open, no additional dissipation source is injected in the system and the nominal response (without any controllable valve) is restored; this is equivalent to disconnecting the adaptable damping source, which is an unsolved problem for many existing adaptable mechanisms. Finally, pursuing lightness of moving parts, the valve is placed in a proximal position, close to the input motor. A distal disposition may offer a better attenuation of the oscillations occurring at the output link when tasks involving wide spatial displacements are assessed, but it increases the arm inertia; this trade-off will be better investigated in the future work.
Given the preliminary nature of the proposed experiments, a controllable valve has not been employed yet, but a simple valve with manual regulation is used instead: by rotating its regulation knob, the user can manually adjust the cross-section of the inner fluid channel. The parameter describing the adjustment state is referred as *aperture* α. The setting $\alpha = 100\%$ denotes fully open valve, i.e. the hose cross-section is not altered, while $\alpha = 0\%$ denotes completely closed valve, i.e. fluid velocity equal to zero and blocked transmission.

6.3 Experiments

In this experimental session the configuration of the test-bench is equal to the one described in Fig. 2.4 and the model description follows the scheme in Fig. 3.2: the output link, as usual connected to the output pulley, is clamped to ground by means of the load cell placed at the end effector. This setting can be schematized according to Fig. 6.1 (*adaptable*), where the control action is not performed by actuator A, but manually by the user before running each experiment. Assuming the valve to produce a linear viscous effect, the damping coefficient is function of the

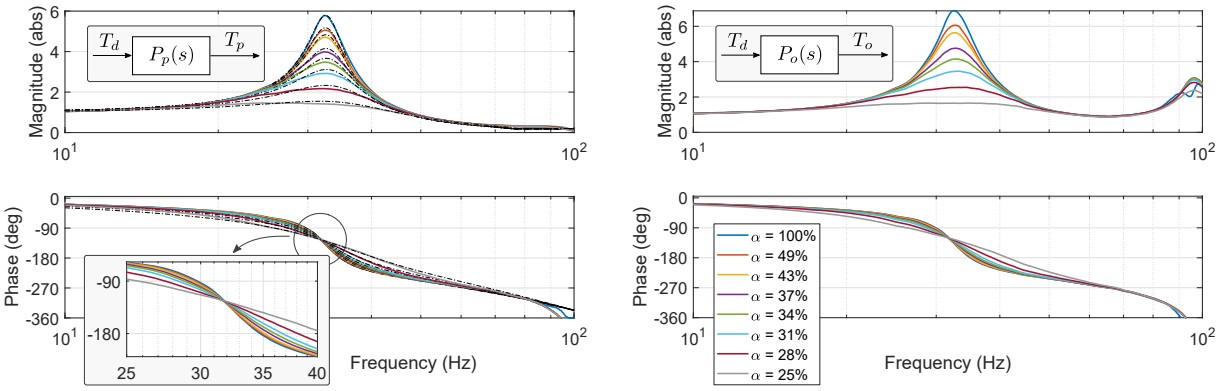

Figure 6.4: Experimental frequency responses of the open-loop plant function of different valve aperture α. *Left*: transfer function $P_p(s)$ from T_d to T_p. *Right*: transfer function $P_o(s)$ from T_d to T_o. The dashed-dotted black lines in the left plot represent the second-order model identification.

valve aperture $c_a = f(\cdot, \alpha)$. In this test, the reference torque signal T_d commanded to the input motor is a linear chirp with frequency ranging from 0 to 100 Hz; the T_p and T_o outputs are simultaneously acquired and the corresponding transfer functions, $P_p(s)$ and $P_o(s)$, are evaluated (refer to Fig. 3.2 for the definition of nomenclature). Experimental results are shown in Fig. 6.4. The effect of the damping action produced by the valve is close to the one expected in Fig. 6.1 (right): as the valve aperture is progressively reduced, the amplitude of the resonance peak is attenuated and the phase lag about the resonance frequency gets smoother both in the $P_p(s)$ and in the $P_o(s)$ transfer functions, meaning that higher dissipation is injected in the system. The dashed lines depict the response of the identified second-order linear model (3.2); notice that parameters $\omega(\alpha)$, $\xi(\alpha)$ and $\tau(\alpha)$ are function of α now. The model closely matches the experimental response for a wide range of damping values, meaning that the linearity assumption is justified for the current experimental conditions, i.e. small displacements. Table 6.1 reports the identified parameters as function of the valve aperture α: the value of the parameter $\xi(\alpha)$ approaches the one measured in Chapter 3 (without valve) when the valve is completely open, and it increases by a factor of 4 for $\alpha = 25\%$. As deducible from the first column of the table, there exist a limited range of aperture α that generates a measurable variation of damping: in particular, the transfer function parameters are almost unaffected the range $\alpha = 50$–100%, while the transmission can be assumed almost blocked in the range $\alpha = 0$–25%. Even if the

Table 6.1: Dynamical identification of model (3.2) for different values of valve aperture α.

α (%)	ω (Hz)	ξ (-)	τ (ms)
100	32.78	**0.0867**	3.4753
49	32.80	**0.0971**	3.4728
43	32.87	**0.1041**	3.4928
37	33.05	**0.1213**	3.5155
34	33.22	**0.1377**	3.5132
31	33.52	**0.1626**	3.5495
28	34.19	**0.2199**	3.6146
25	36.09	**0.3451**	3.8151

action of the valve mainly influences the value of parameter $\xi(\alpha)$, some marginal effects are also produced on parameters $\omega(\alpha)$ and $\tau(\alpha)$.

6.4 Discussion

This chapter presents a simple yet effective strategy to implement *adaptable damping* in hydrostatic transmissions by introducing a controllable valve in the fluid lines. A wide variety of damping coefficients are measured and the additional braking feature is highlighted. As the phase-lead effect after the resonance peak is experimentally visible, further research on this adaptable mechanisms is motivated, being potentially able to extend the bandwidth of closed-loop torque control. In haptic applications a wider variety of virtual impedance can be displayed to the user and residual oscillations of position-controlled tasks can be suppressed.
Future work will imply the use of a proper controllable valve instead of the manually adjustable one. The velocity at which the value of the adaptable damping is required to change, even during collaborative or challenging positioning tasks, is assumed reasonably low and achievable by a simple solenoid valves; sophisticated servo-valves should not be required for this application. Furthermore, once the controllable valve proves appropriate, a suitable control strategy will be developed in order to autonomously modulate the adaptable behaviour during functioning. Frequency-domain experiments will be performed in order to assess closed-loop bandwidth extension; in this scenario, the stability implications of the valve position along the fluid channels will be investigated. Large-displacement tasks involving tracking of challenging trajectories will be also considered; the development of a nonlinear quadratic model of viscous friction might be required.

Chapter 7

Conclusions and Future Work

This thesis offers a comprehensive study of **R**olling **D**iaphragm **H**ydrostatic **T**ransmissions (RDHTs) to remotely actuate a new generation of lightweight, force-controllable robotic arms. Performance and safety requirements that traditionally belong to different families of robots, i.e. industrial and collaborative, are merged together in a unified advanced design paradigm and embedded in smart mechanical structures, without trade-offs. Shaping a proper open-loop response, regardless the applied control, is the key principle that drove the proposed study. Hydrostatic transmissions enable the remote positioning of direct or quasi-direct drive electric motors, taking their mass away from the robotic arm and therefore generating lightweight structures. The low inertia of direct drive actuation and lightweight links, combined with a stiff and transparent transmission of the motors' action to the remote joints, outlines the core of safe robots with low mechanical impedance, high specific power, excellent backdrivability and large force bandwidth. This design paradigm has been made possible by a deep analysis of hydrostatic transmissions and a redefinition of the elements that have a critical role in the torque reflection transparency. Novel low-friction and leakage-free hydraulic cylinders are developed based on rolling diaphragms and a minimally constrained floating-bonnet layout [1, 2]. The proposed design brings together a number of additional positive attributes, such as low mass, high specific torque and power, ease in control, absence of backlash, lubricant-free (water can be used as working fluid) and wear-free operation, and undemanding manufacturing tolerances; moreover the resulting system is low-cost. This result enables the creation of a prototypical modular hydrostatic transmission that provides a rotation range of 140° and generates a maximum rated torque of 25 Nm. Experiments reveal that the static friction of the RDHT-based actuation system is 0.24 Nm, i.e. just 0.96% of the maximum rated torque. According to the design intentions, frictional properties confirmed independent of the applied load, which is a favorable feature inaccessible to the widely-used cable-based transmission systems. Exploiting a low-cost pressure sensing technique, a closed-loop Smith-predictor-based joint torque control is developed to achieve enhanced, uniform properties of torque setpoint regulation over a large range of frequencies [4]. Experiments prove the simple model-based control strategy effective also in guaranteeing safe, high-quality physical Human-Robot Interaction (pHMI). Experimental tests validate the significant advantages of the closed-loop control architecture, reducing the backdriving torque by 67% (0.6 Nm in open loop and 0.2 Nm in closed loop) and the settling time by 95% with respect to the open loop. The open-loop response is still largely acceptable on the whole range of frequencies that characterise realistic scenarios of manipulation and inter-

action. Based on previous mechanical and control developments, a remotely-actuated planar robotic arm with indirect pressure-based torque sensing at joint level is implemented; the operating space of the robot is comparable to that of a human arm. The transparency, backdrivability and controllability properties of open-loop and closed-loop responses smoothly extend to the multi degrees of freedom case. The device proves the power-yet-gentle paradigm by performing a collaborative manipulation task that involves the displacement of a heavy payload over its entire workspace, requiring an extremely low effort of the user. The dynamical properties of the proposed actuation principle are further stressed by developing a miniaturized pneumatic transmission with intrinsic series-elastic properties for the remote actuation of the ankle joint of an agile bio-inspired hopping robotic leg [5]. This highly dynamical system represents the ideal test-bench for investigating advanced locomotion strategies. The hopping robot is characterised in agile forward hopping experiments and the capability of influencing the timing of the energy exchange with the ground during push-off produces relevant effect in the observed gait. Finally, a simple yet effective solution to implement adaptable damping in hydrostatic transmissions is proposed and tested. Adaptable damping brings a series of advanced features such as the stable modulation of interactions (consider haptic interfaces) and impacts, the generation of large dissipative actions with very low actuator effort, the extension of the closed-loop torque bandwidth and the implementation of remote emergency braking systems.

7.1 Future technical developments

Future developments will assess solutions to improve performance and reliability of the hydrostatic transmission to name a few examples. Advanced solutions to further reduce the inertia of the robotic arm will be considered, such as substituting each direct or quasi-direct drive actuator with pairs of smaller electric motors combined in a proximal macro-micro architecture. Suitable combinations providing lower inertia and cost-effective selection of the electric motors will be pursued. Indeed, the hydrostatic transmission provides enough stiffness to reflect both low and high frequency actuation contributions, without requiring the high frequency actuators to be placed close to the joint, as cable-based transmissions do. Also, fatigue testing the floating-bonnet cylinders will provide useful information about the capability of the current design to meet the requirements of industrial and medical applications.

7.2 Possible applications

The design paradigm developed in this thesis may contribute to many different application fields of robotics. First of all, as stressed in previous chapters, simultaneously meeting the requirements of industrial and collaborative robots is quite a novel and attracting capability. Future developments will explore the possibility of instantaneously switching between the two operating modes in real time via software. Absence of leakages, cleanliness of water-based functioning and silent operation (no gearing or pneumatic valves) motivate possible application of RDHT-based devices in medical and cleanroom environments. Moreover, RDHTs may considerably simplify the design of robotic arms with very large workspace for the manipulation of moderate payloads. On the other hand, the use of large membranes can scale this technology towards

heavy-duty applications. Also, passive or semi-active configurations may be devised to help workers in repetitive heavy-duty tasks. Having the actuation block detached from the mobile structure of the robot facilitates the cooling of motors, which would not be easily accessible when located close to the moving joints. Also, sealing the actuation unit, combined with a sensorless configuration of the robotic arm, gives the premise for creating robots capable of operating underwater or in hazardous environments (e.g. according to the European ATEX directives for equipment used in explosive atmospheres).
The lightweight, remote torque transmission may simplify the design of many distal devices, such as robotic grippers, tools and exoskeleton wrists and hands. In general, the development of complete upper and lower limb exoskeletons is a promising application: the high specific torque of each joint and the flexible routing of the hydraulic hoses allow designing compact, ergonomic and lightweight devices capable of supporting users' arms and legs. Accurate controllability would produce enhanced torque rendering for gaming-based rehabilitation and remote manipulation. Compared to other existing cable-based solutions, hydrostatic transmissions are not integrated in the structure of the links, enabling their length to be easily modified to adapt the same device to different users. Moreover, the low-cost feature of RDHTs, alongside modular design, would contribute to make exoskeletons affordable and spread the robotic rehabilitation therapy. Finally, based on the results of this work, novel configurations of agile robotic legs that integrate advanced capabilities such a series-elastic and adaptable-damping features, will be devised.

Appendix A

Dynamic Limitations to Force Control

Certain robot applications depend on the precise interaction forces that the robot exchange with its surrounding environment. The control of interaction forces may be demanded either as a requirement to complete a task or as a response to uncertain contact conditions. It's enough to think to many of the operations required for assembling processes or scenarios in which robots share their workspace with human beings. " Force control" of robots originated from the need of allowing machines to move in unknown environment with compliant behaviour. This term is used to describe the control schemes where the measurement of the interaction force is used to alter the trajectory commands given to the robot. When the end-effector sensed force is the only information used in the controller, the simplest force control strategy is defined, called *explicit force control*, figure A.1. Even if a variety of more complex strategies have been developed, the

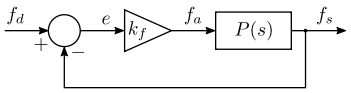

Figure A.1: *Explicit force control* scheme.

explicit force control still represents the fundamental concept behind compliant control. In this chapter, it will be analysed to extract some remarkable results about the coupled mechanical and control design.

A major issue in the development of active compliance robots is the performance limitation inherent in all the existing methods. System response cannot be increased without any bounds, and it is well known that force controlled robot may undergo instability when high performance is pursued. Performance limitations come about in a variety of forms; for example, an end-effector force controlled robot may undergo violent chatter upon contact with a stiff surface. When dynamical problems arise, control gains must be typically reduced until stable behaviour is obtained, resulting in a sluggish closed-loop response. Although the control system is responsible for the instability sometimes, in most of the cases the achievable performance is limited by the dynamical characteristics of the mechanical system, namely *rigid-body bandwidth*, *dynamically noncolocated modes* and *dynamically colocated modes*, [103]. Rigid-body dynamics refers to the ideal performance in absence of any flexibility. Furthermore, real machines always include some form of flexibility: links undergo structural bending or torsion; gear teeth in gearboxes deform; transmission cables or belts stretch; mounting base, workpiece and gripper are not be perfectly rigid; bearings may deform or introduce some play. Even if all of these flexibility sources

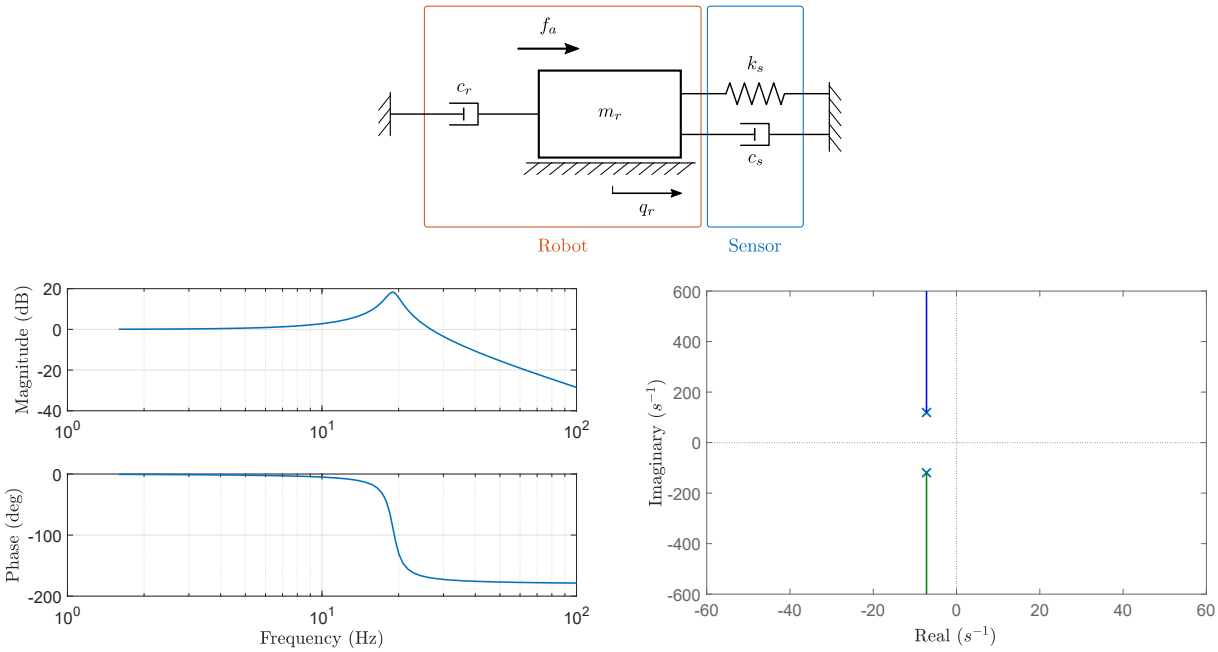

Figure A.2: Rigid-body robot model.

are very different, it was found that only their position in the robot structure is relevant to determine their effect on the overall dynamics. Two cases can be distinguished: when flexibility is placed between the actuator and the force sensor, then noncolocated modes rise; when flexibility is not placed between the actuator and the sensor, then the colocated modes rise. Note that the actuator and the sensor may vibrate out of phase in the first case, while they are constrained to vibrate in phase in the second one.

In this chapter, the impact of typical robot dynamical effects are illustrated using a single robot axes model. Notice that the proposed models will show the robot always in contact with the environment; this highlights how the dynamic coupling between robot, sensor and environment plays a central role when force control is assessed.

Let us first consider the robot axis to be rigid, with no vibrational modes. Even in this simple case, the sensor connects the robot and the environment with some compliance, Fig. A.2. The sensor is characterized by stiffness k_s and damping c_s, while the robot link is characterized by its effective mass m_r. The viscous damper c_r, is chosen to give the appropriate rigid-body mode to the unattached robot, summing up all of the damping effects contained in the mechanism. The actuator is ideal and its force action f_a is directly applied to the robot link. By the control point of view, the output variable of the closed-loop system is the force across the sensor $y = f_s = k_s q_r$, and, once the measured force is fed back to the controller, the closed-loop control action is defined by $u = f_a = K_f(f_d - f_s)$. When feedback is applied, the resulting root locus shows that the closed-loop is unconditionally stable, meaning that the controller gain can be unlimited increased without affecting stability; in fact, K_f can be chosen to give any desirable response characteristics to the system, increasing its natural frequency and never getting to instability. It is interesting to notice that the control loop modifies the force transfer function only in the stiffness

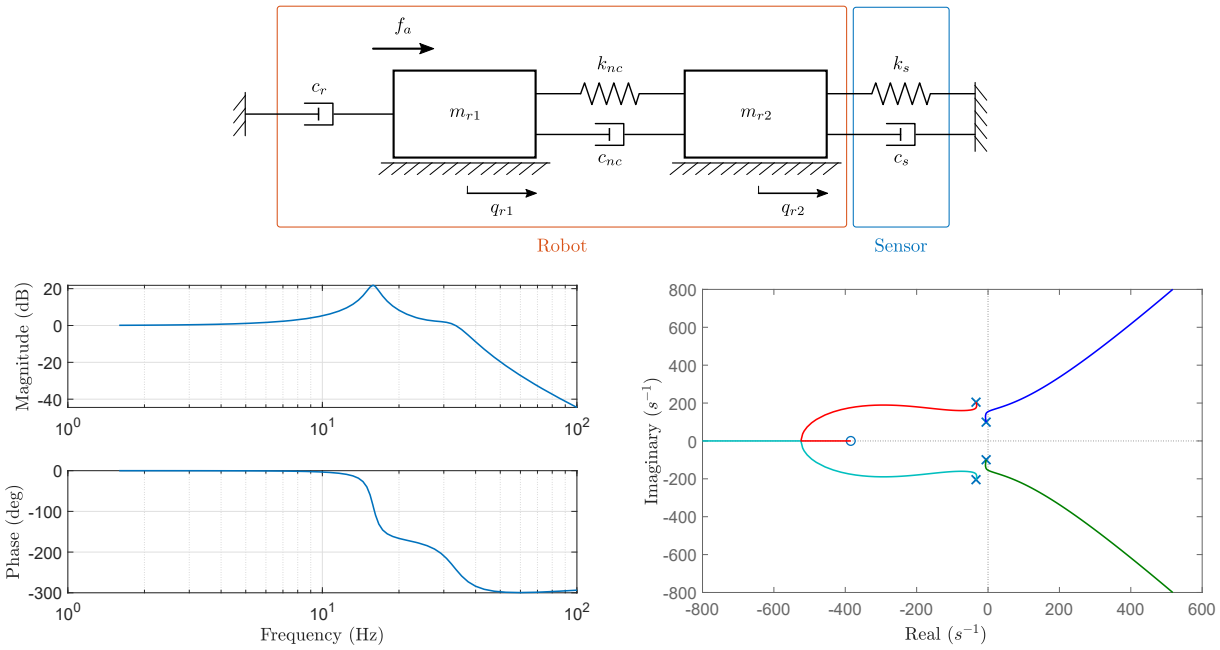

Figure A.3: Robot model with noncolocated modes.

term:

$$P(s) = \frac{f_s(s)}{f_d(s)} = \frac{k_s K_f}{m_r s^2 + (c_r + c_s)s + k_s(1 + K_f)} \tag{A.1}$$

meaning that, in this simple case, the explicit force control actually behaves like a position servo control.

The rigid-body model descriptiveness is clearly limited and instability events are not predicted. Let us now consider the effect of noncolocated modes by adding the first structural resonance mode of the robotic arm, Fig. A.3. The total robot mass is now split between m_{r1} and m_{r2}. Stiffness k_{nc} and damping c_{nc} characterise the first mode of the robot, while damping c_r, as before, governs the rigid-body mode. The Bode plot of the open-loop response is affected by a second natural frequency. In particular, the phase plot reveals that there exist frequencies above which the velocities of the actuator and the sensor will not only be different, but will be completely out of phase. This is the core consideration to keep in mind when looking at the root locus of the closed-loop system: the explicit force control is only conditionally stable, so high closed-loop gains would lead the robot to instability; structural flexibility imposes an upper bound to the robot performance. This means that explicit force control is feasible only if the desired closed-loop bandwidth is lower than the first mode frequency of the robot. Therefore, noncolocation is the stability problem that occurs when a feedback loop is closed using a sensor and an actuator that are physically located at two different points of a flexible structure.
It is now clear why in many applications the force control bandwidth is effectively extended by replacing the wrist force sensor with joint torque sensors and closing a torque loop at joint level, [70]. In this case, the structural flexibility is outside the torque loop and it will only affect the end-effector accuracy, without provoking instability.

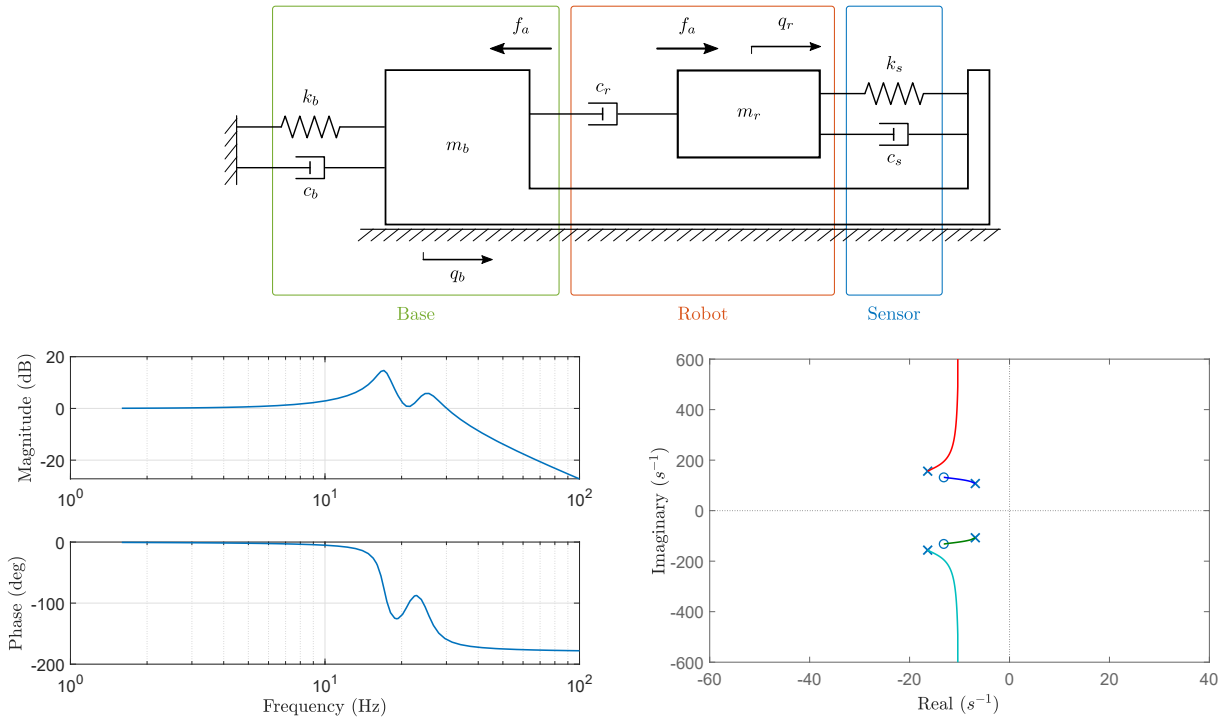

Figure A.4: Robot model with compliant base.

Let us now investigate the effect of colocated modes, starting from base compliance. Industrial robots can be quite massive machines tool and the base on which they are mounted is never perfectly rigid. The base compliance often gives rise to the lowest frequency mode observed in the machine response. Figure A.4 describes the configuration of many industrial robots, for which the workpiece is generally mounted on the robot base plate. m_b, k_b and c_b represent the base mass, stiffness and damping; the robot is considered rigid. Actuator and sensor are attached to the same degree of freedom, so they never vibrate opposite in phase. The Bode plot clearly describes how the base contribution differs from the noncolocated effects: a sharp lead in phase is introduced, quickly followed by a phase lag. This is typical of low-damped structural modes, where a pair of poles are very near to a pair of zeros. As the damping b_b increases, then the pair of poles and zeros will move away from the imaginary axis and they will have less effect on the overall response: increasing the base damping may be quite beneficial. The disturbance intensity is mitigated; after all, the impossibility of acting on the base mass m_b or on the fixation stiffness k_b is quite concrete in many practical cases. Anyway, even if the base compliance adds some visible contribution to the machine response, it is not responsible for system instability.

As previously mentioned, from experimental evidence a force-controlled robot is very likely to become unstable against a stiff environment. This is probably the major issue in force-control implementation. This effect is assessed by modeling the workpiece compliance, Fig. A.5. This model structure is identical to the one used to describe transmission flexibility, but the different placing of the sensor makes a substantial difference. In fact, the typical behaviour of colocated modes is showed again by the Bode and the root locus plots similarly to those associated with the base compliance case. Even in this case instability is not predicted. It can be said that

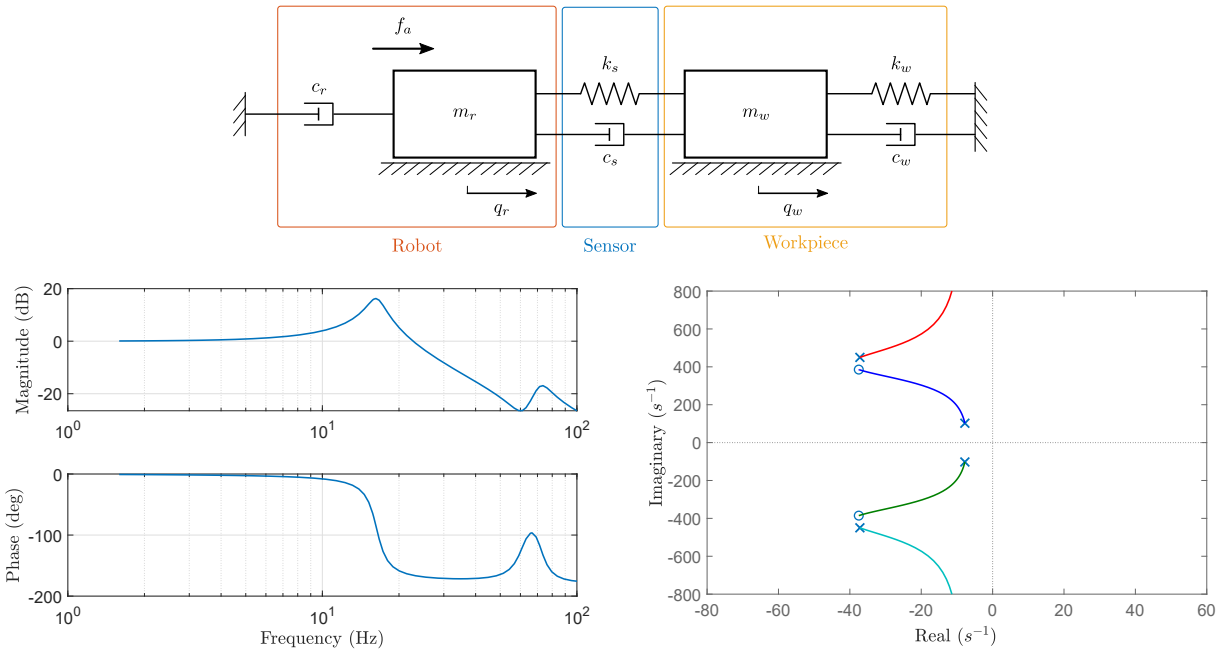

Figure A.5: Robot model with compliant workpiece.

the colocated modes cannot drive the system to instability because they always add the same number of poles and zeros, while noncolocated modes add more poles than zeros.

However experimental observations suggest that the workpiece can significantly affect the system dynamics, identifying a stiff environment as the most destabilizing condition for a force controlled robot. Certainly, if the workpiece were very compliant and extremely light, there could be no force across the sensor, degenerating the closed-loop system to the open-loop case, which of course is stable. The contact instability phenomenon can be explained taking into account the nonideal response of the actuators, [104]. In particular, the real actuators are not ideal torque sources, but they are bandwidth-limited instead, Fig. A.6. Under this condition, the root locus proves that even the rigid-body model is now conditionally stable, experiencing instability for high gains.

The combination of the force sensor contacting a stiff environment can be seen as a series of two elastic elements and it can be schematized as a single spring with high stiffness. Since equation (A.1) tolls us that the physical stiffness and the control gain really have the same effect by the stability point of view, a rigid-body robot touching a stiff environment can actually be seen as a servo position feedback with very high gain; under the assumption of bandwidth limited actuators, this configuration is very likely to be unstable, Fig. A.6. An interesting robustness analysis is developed in [70]. In light of this, increasing the actuator bandwidth means extending the range of gains for which the system is stable; in the absence of actuator limitations, as previously mentioned, the model predicts stability for all gains and all values of model parameters.

The colocated mode associated with workpiece compliance was experimentally observed to be more likely responsible for system instability than the base flexibility. Even if the two events inject a similar contribution in the robot force response, the workpiece mode is generally associated with higher frequencies, where the phase margin of the robotic system is reduced by actuator bandwidth limitations and noncolocated modes. The base mode, on the contrary, is generally

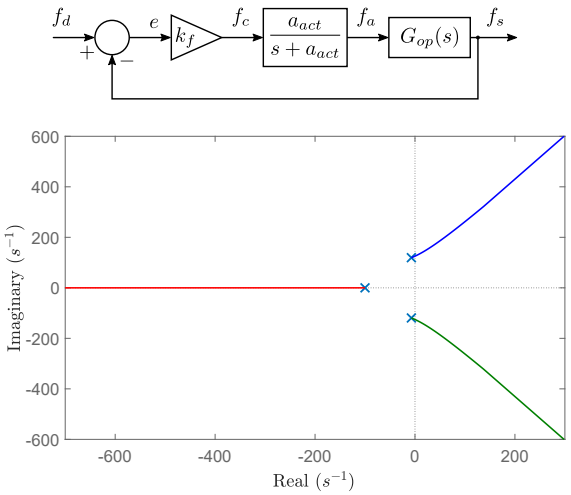

Figure A.6: Model of rigid-body robot with limited bandwidth actuators.

associated with lower frequencies, where the robot response is closer to ideality, and its phase margin is large enough to mitigate the disturbance.
Contact instability does not induce the robot to exponentially diverge in real scenarios, it is more likely to happen as a limit cycle event, referred as *chatter*, where the robot keeps rapidly bouncing on the stiff surface, making and breaking the contact with the workpiece, [104]. Of course this is a nonlinear behaviour that cannot be predicted by the linear models commonly used to design the controller. The stability bounds derived using the linear models should be used to set upper limits on the controller gains, which should then be decreased if limit cycles are observed under operating conditions, [105]. Nonlinear simulations suggest that if the linearized system has sufficient damping, then neglecting the discontinuity is justified, [105].
It may be intuitively thought that the fast chatter oscillations may be suppressed by low-pass filtering the torque command driven to the actuator. However, this configuration really acts like a limitation on the actuator bandwidth, so that the low-pass filter action in the force loop would drive the system to instability even faster, [104]. Low-pass filtering the feedforward reference may produce slightly better results. Among many other possible sources of nonlinearity, it was shown that Coulomb static friction may extend the stability bandwidth, [106], even degrading the accuracy.

A.1 Discussion

This chapter shows how structural and control design are strictly related in robotic applications. The two aspects can never be conceived separately: mechanical designers have to bear in mind the dynamical issues rising from the interaction between control strategy and structural flexibility, when components for robotic applications are designed. The mechanical design of robots depends on where sensors are placed, i.e. links and transmission systems have to shaped maximizing stiffness if they are placed between actuators and sensors. In conclusion, noncolocated modes and limited bandwidth actuators are the main causes of instability for force controlled systems, when high performance is required. In this nonideal scenario, even colocated modes associated with workpiece/environment stiffness became determinant factors for stability. Meth-

ods for extending the stability bandwidth against uncertain and stiff environment include soft covering on the robotic structure or soft grippers, [107], so that the environment appears to be softer to the robot. Also replacing the end-effector force control with local joint torque loops may be beneficial to stability. Anyhow, these precautions unavoidably degrade the robot accuracy.

Appendix B

Cogging Torque Analysis and Compensation

Brushless DC motors are usually considered ideal sources of torque, as the current I flowing through the stator windings generates a proportional torque T_m on the rotor according to the equation:

$$T_m = k_\tau I \tag{B.1}$$

where k_τ is the torque constant of the motor. This assumption is reasonable, but additional nonlinear effects have to be taken into account when low-speed transparency and accurate force display are pursued through direct or quasi-direct drive actuation.

This section describes the strategy applied to the prototypes presented in this work to compensate for the nonlinear disturbances affecting brushless motors. The proposed compensation strategy does not require any additional sensor with respect to those already needed for the servo control of brushless motors, i.e. a current sensor and an absolute encoder, and produces a good low-speed torque display even using standard industrial motors. Results are shown using the Kollmorgen AKM52L brushless motor.

B.1 Introduction to Torque Ripple

Torque ripple is defined as a periodic fluctuation in the torque generated by the electric motor over a complete revolution of the rotor. This undesirable effect can be thought of as a periodic torque component of moderate amplitude that is superimposed to the nominal torque described by (B.1). Basically, a brushless motor does not produce uniform torque over a complete revolution when energized with constant current. At very low speed, torque ripple prevents the motor from rotating smoothly, producing relatively large speed disturbances and even causing the motor to suddenly stop or move in discrete increments. At high speed it may cause velocity fluctuations, vibrations and acoustic noise, but it is generally a less relevant phenomenon since it produces a high-frequency ripple that is filtered out by the rotor inertia.
While torque ripple is the visible and measurable fluctuation of the delivered torque, the physical cause that mainly produces this disturbance is referred as *cogging torque*. It is generated by the pure magnetic attraction between the permanent magnets of the shaft and the ferromagnetic

teeth of the stator, so that, the torque ripple due to the cogging torque corresponds to the force that is needed to break this internal attraction. The cogging torque T_c is a position-dependent fluctuation that will equally repeat at each revolution of the motor according to the shaft angle θ_m relative to the stator teeth position.

$$T_c = f(\theta_m), \quad 0 \leq \theta_m < 2\pi \tag{B.2}$$

The magnets always head to a position of minimum reluctance so, the motor revolution results in a sequence of stable and unstable equilibrium points each time the magnets travel from a teeth to the other. Notice that cogging torque is not current-dependent so it can be experienced even when the motor is not powered and it cannot be measured by a current sensor.
Other effects contribute to the torque ripple: a mismatch of the rotor magnetic field and the stator current waveform may cause some oscillation in the generated torque; *reluctance torque* is a result of the variation in the stator self-inductance due to the rotor magnet saliency; *friction torque* is not always axisymmetric, since the bearings within the motor may contain eccentricities. Notice that effects related to the friction are very distinguishable because they change sign upon a change in motor direction. By the way, these phenomena generally produce negligible torque ripple than the one produced by the cogging torque, so their rigorous characterisation goes beyond the purpose of this work and their compensation is not addressed.

Primary methods for mitigating the effect of cogging torque rely on the mechanical design of the motor. The number of windings or the number of permanent magnets can be increased in order to reduce the variation of the attraction intensity between the stator and the shaft. More sophisticated solutions consist in skewing or shaping the permanent magnets placed on the shaft to make their transition between stator teeth more gradual [108]. Despite good torque ripple reduction can be achieved, these methods are not widely used for industrial purpose yet and some advanced solution can be found only in custom applications. It is possible to use a force sensors to feedback the motor and suppress any form of torque ripple but it may require a sensor more expensive than the motor itself. Therefore, simple and effective position-based compensation methods are widely used to partially reduce the torque ripple of standard industrial motors: these methods rely on the position error or current measurement under position control in order to map the cogging and friction torques [109]. If ripple waveform is known over the motor workspace, (B.2), a controller can suppress the ripple by simply subtracting the ripple component from the desired torque, Fig B.3. This strategy is particularly effective at low speeds, where the frequency of the ripple disturbance is lower than the controller bandwidth.

B.2 Cogging Torque Characterisation

Good torque ripple reduction can be obtained if cogging torque is accurately characterised over a complete revolution of the shaft. We know that the current sensor of the motor cannot sense the cogging torque, but it can measure the delivered torque (i.e. current) needed to counteract cogging torque in properly designed experiments. To this end, the approach applied in this work consists in measuring the absorbed current I while the motor is slowly rotated ($\dot{\theta}_m = 0.05$ rad/s) by a high-gain position control. At each position, the absorbed current is used as indirect measurement of the torque T_m needed to maintain the motor in position (also called "*holding torque*"

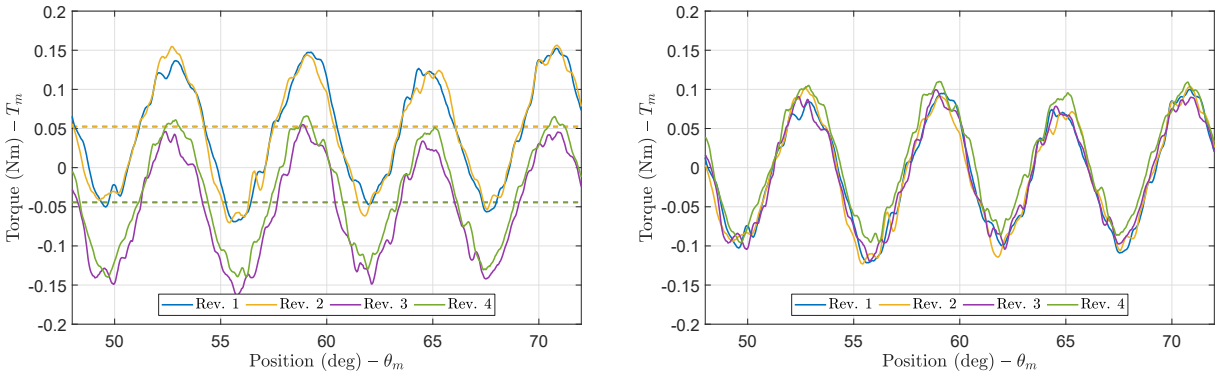

Figure B.1: Measurement of the holding torque. *Left:* torque profiles measured at each revolution; the figure represents the rotation range $45 - 75$ deg. The shaft rotates in positive direction during revolutions 1 and 2, and in negative direction during revolutions 3 and 4. The dashed lines represent the mean value of each torque profile evaluated over a complete revolution. *Right:* measurements of Fig. B.1 (left) after removing the mean values.

in this case), and so to counteract friction and cogging torques. Repeated measurements of T_m are shown in Fig. B.1 (left); the measured waveforms are the clear result of the superposition of the periodic position-dependent cogging component and the constant additive contribution of friction. The friction contribution, corresponding to the mean value of the measured waveforms, is very distinguishable because it changes sign when velocity is reversed. A value of 0.05 Nm was measured for friction torque. Once the friction effect is identified and removed from the measurements, the contribution of the cogging torque can be highlighted, Fig. B.1 (right); the waveform is very repeatable even when the velocity is reversed. Measurement reveal a cogging torque amplitude of 0.1 Nm with 60 oscillations over a complete revolution.

B.3 Waveform Identification

Once the cogging waveform is extracted from the measured signal at each revolution, an unique nominal waveform must be defined in order to be stored in the controller. Two approaches were considered: the first strategy consists in fitting a sinusoidal function to the measured data, while the second one consists in storing the mean value of the torque measured during the four repetitions at each encoder position in a look-up table. These two strategies are compared since they offer opposite features. The sine fitting approach is extremely low demanding by the computational point of view since the sine profile can be easily stored and evaluated online, but the description that it offers is not flexible. Conversely, the look-up table requires memory to be stored and the search algorithm, run at each control loop, is generally time consuming. By the way, this second strategy offers a more versatile description and it is able to adapt to peaks and phase variation due to the irregularities of magnet and winding properties.
The sinusoidal waveform is defined according to (B.3) and its coefficients are evaluated in order to minimize, in a least-square sense, the error between measurements and compensation function $T_c = f(\theta_m)$. Tab. B.1 lists the resulting coefficients.

$$T_c = a\sin(\omega\theta_m + \phi) + b, \quad 0 \leq \theta_m < 2\pi \tag{B.3}$$

The second approach evaluates the mean value of the motor torque measured at each j-th

Simbol	Quantity	Unit	Value
a	amplitude	(Nm)	0.091
ω	frequency	(-)	60.000
ϕ	phase	(rad)	3.020
b	bias	(Nm)	0.000

Table B.1: Last-square optimal coefficients of the cogging torque identification based on a sinusoidal model.

revolution in correspondence of the i-th encoder position, according to:

$$T_c^i = \frac{1}{R}\sum_{j=1}^{R} T_m^{ji}, \quad i = 1..N \tag{B.4}$$

where the T_c^i is the value of the compensation action at encoder position θ_m^i, and T_m^{ji} is the motor torque measured at repetition j and position i. R represents the total number of revolutions performed during the experiment and N is the total number of encoder positions (resolution). A look-up table $L_c(\theta_m) = \{\theta_m^i, T_c^i\}$ is then defined.
The solution of the two identification methods are compared in Fig. B.2 (left) over a small portion of the angular domain. As expected, the sine wave closely matches the measured profiles but it is not able to describe possible irregularities due to the fact that magnets and windings may not be perfectly spaced or shaped. This can be seen in the amplitude fluctuation at $56°$, and in the phase shift during the transition between two consecutive peaks, as happens between $59°$ and $62°$. The look-up table is instead able to adapt to any source of irregularity, and it ensures a zero mean error e_τ at each encoder position by definition, Fig. B.2 (right).

B.4 Compensation Scheme and Results

Both compensation strategies are implemented according to the control scheme in Fig. B.3 (the scheme depicts the calculation of the compensation term T_c by using the look-up table L_c, but it can be easily extended to the case of sine-based compensation). The the motor is controlled

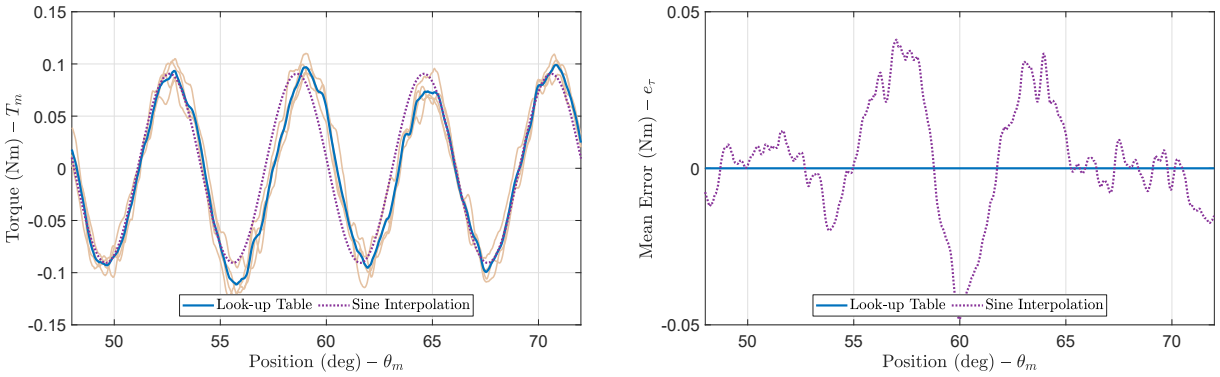

Figure B.2: Holding torque identification. *Left:* identification of the holding torque profile using two different strategies. *Right:* mean error of the two strategies.

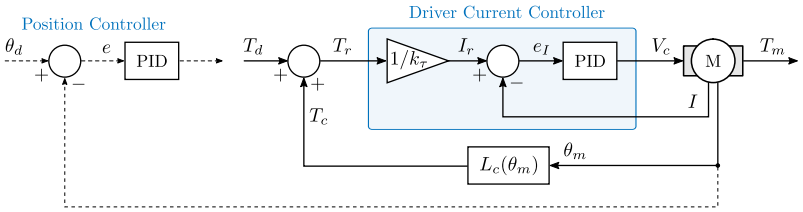

Figure B.3: Control scheme for cogging torque compensation. The desired torque T_d is modified by adding the compensation term T_c, and the modified reference T_r is commanded to the motor driver. T_r is transformed in current reference I_r by multiplying it by $1/k_\tau$; an error signal e_I is provided to the PID controller by subtracting the actual absorbed current I. The PID controller generates the voltage command V_c.

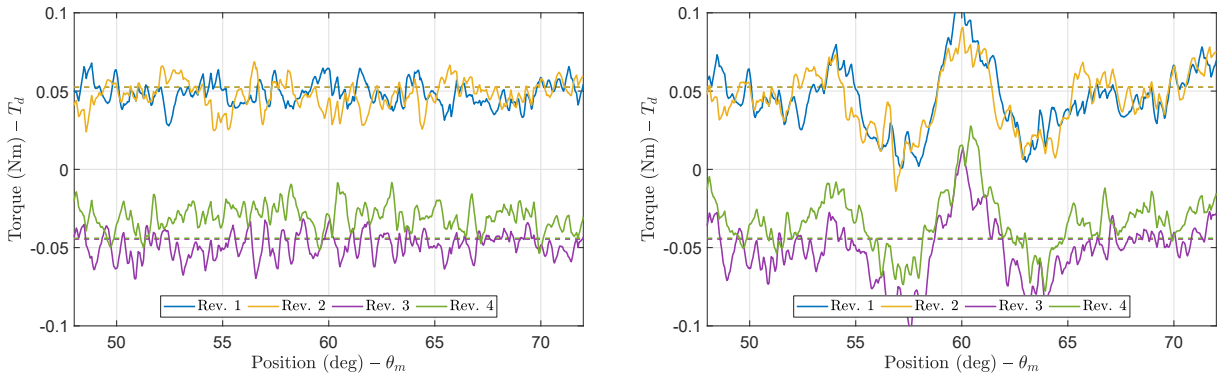

Figure B.4: Measurement of the residual torque ripple with cogging torque compensation active. *Left:* look-up table strategy. *Right:* sinusoidal interpolation strategy.

along the same position trajectory used for characterization purposes in Appendix B.2 and the torque needed to hold the motor in position is evaluated again. Results are shown in Fig. B.4; notice that in this configuration the comparison has to be based on torque T_d. A better reduction of the torque ripple is achieved by the look-up table approach, resulting in lower peak-to-peak fluctuations and in more uniform behaviour. The peak-to-peak variation is reduced by the 78% by the look-up table strategy and by the 52% by the sine-based scheme, Tab. B.2. In conclusion, the proposed strategy has proved successful and the compensation algorithm based on the look-up table $L_c(\theta_m)$ has been used in every experiment performed in this thesis.

Test	Peak-to-peak (Nm)	Reduction $(\%)$
Without compensation	0.255	–
Look-up table	0.057	78
Sinusoidal interpolation	0.123	52

Table B.2: Comparison of the two compensation algorithms. The second column refers to the peak-to-peak amplitude of the holding torque evaluated over a full revolution, while the third column shows the reduction of the peak-to-peak amplitude with respect to the non-compensated test.

Bibliography

[1] Marco Bolignari, Giacomo Moretti, and Marco Fontana. Design and experimental characterisation of a hydrostatic transmission for upper limb exoskeletons. In *2018 IEEE/RSJ International Conference on Intelligent Robots and Systems (IROS)*, pages 2768–2773. IEEE, 2018.

[2] Marco Bolignari and Marco Fontana. Design and experimental characterization of a high performance hydrostatic transmission for robot actuation. *Meccanica*, 55(5):1169–1179, 2020.

[3] ID Sîrbu, G Moretti, G Bortolotti, M Bolignari, S Diré, L Fambri, R Vertechy, and M Fontana. Electrostatic bellow muscle actuators and energy harvesters that stack up. *Science Robotics*, 6(51), 2021.

[4] Marco Bolignari, Gianluca Rizzello, Luca Zaccarian, and Marco Fontana. Smith-predictor-based torque control of a rolling diaphragm hydrostatic transmission. *IEEE Robotics and Automation Letters*, 6(2):2970–2977, 2021.

[5] M. Fontana M. Bolignari, A. Mo and A. Badri-Spröwitz. Diaphragm Ankle Actuation for Efficient Series Elastic Legged Robot Hopping. In *2022 IEEE/RSJ International Conference on Intelligent Robots and Systems (IROS). SUBMITTED.*, 2022.

[6] Haruhiko Asada and Takeo Kanade. Design of direct-drive mechanical arms. 1983.

[7] Haruhiko Asada, Takeo Kanade, and Ichiro Takeyama. Control of a direct-drive arm. 1983.

[8] Pablo López García, Stein Crispel, Elias Saerens, Tom Verstraten, and Dirk Lefeber. Compact gearboxes for modern robotics: A review. *Frontiers in Robotics and AI*, 7:103, 2020.

[9] Antonio Bicchi and Giovanni Tonietti. Fast and" soft-arm" tactics [robot arm design]. *IEEE Robotics & Automation Magazine*, 11(2):22–33, 2004.

[10] Yong-Jae Kim. Design of low inertia manipulator with high stiffness and strength using tension amplifying mechanisms. In *2015 IEEE/RSJ International Conference on Intelligent Robots and Systems (IROS)*, pages 5850–5856. IEEE, 2015.

[11] Michael Zinn, Oussama Khatib, Bernard Roth, and J Kenneth Salisbury. Playing it safe [human-friendly robots]. *IEEE Robotics & Automation Magazine*, 11(2):12–21, 2004.

[12] Dieter Vischer and Oussama Khatib. Design and development of high-performance torque-controlled joints. *IEEE Transactions on robotics and automation*, 11(4):537–544, 1995.

[13] Gerd Hirzinger, A Albu-Schaffer, M Hahnle, Ingo Schaefer, and Norbert Sporer. On a new generation of torque controlled light-weight robots. In *Proceedings 2001 ICRA. IEEE International Conference on Robotics and Automation (Cat. No. 01CH37164)*, volume 4, pages 3356–3363. IEEE, 2001.

[14] Kenneth Salisbury, William Townsend, B Ebrman, and David DiPietro. Preliminary design of a whole-arm manipulation system (wams). In *Proceedings. 1988 IEEE International Conference on Robotics and Automation*, pages 254–260. IEEE, 1988.

[15] Gill A Pratt and Matthew M Williamson. Series elastic actuators. In *Proceedings 1995 IEEE/RSJ International Conference on Intelligent Robots and Systems. Human Robot Interaction and Cooperative Robots*, volume 1, pages 399–406. IEEE, 1995.

[16] B. Vanderborght, A. Albu-Schaeffer, A. Bicchi, E. Burdet, D.G. Caldwell, R. Carloni, M. Catalano, O. Eiberger, W. Friedl, G. Ganesh, M. Garabini, M. Grebenstein, G. Grioli, S. Haddadin, H. Hoppner, A. Jafari, M. Laffranchi, D. Lefeber, F. Petit, S. Stramigioli, N. Tsagarakis, M. Van Damme, R. Van Ham, L.C. Visser, and S. Wolf. Variable impedance actuators: A review. *Robotics and Autonomous Systems*, 61(12):1601–1614, 2013.

[17] CE English and D Russell. Mechanics and stiffness limitations of a variable stiffness actuator for use in prosthetic limbs. *Mechanism and machine theory*, 34(1):7–25, 1999.

[18] Bram Vanderborght, Björn Verrelst, Ronald Van Ham, Michaël Van Damme, Pieter Beyl, and Dirk Lefeber. Development of a compliance controller to reduce energy consumption for bipedal robots. *Autonomous Robots*, 24(4):419–434, 2008.

[19] Giovanni Tonietti, Riccardo Schiavi, and Antonio Bicchi. Design and control of a variable stiffness actuator for safe and fast physical human/robot interaction. In *Proceedings of the 2005 IEEE international conference on robotics and automation*, pages 526–531. IEEE, 2005.

[20] Xiaobo Zhou, Seung-kook Jun, and Venkat Krovi. A cable based active variable stiffness module with decoupled tension. *Journal of Mechanisms and Robotics*, 7(1):011005, 2015.

[21] Shane A Migliore, Edgar A Brown, and Stephen P DeWeerth. Biologically inspired joint stiffness control. In *Proceedings of the 2005 IEEE international conference on robotics and automation*, pages 4508–4513. IEEE, 2005.

[22] Sebastian Wolf and Gerd Hirzinger. A new variable stiffness design: Matching requirements of the next robot generation. In *2008 IEEE International Conference on Robotics and Automation*, pages 1741–1746. IEEE, 2008.

[23] Sebastian Wolf, Oliver Eiberger, and Gerd Hirzinger. The dlr fsj: Energy based design of a variable stiffness joint. In *2011 IEEE International Conference on Robotics and Automation*, pages 5082–5089. IEEE, 2011.

[24] Ludo C Visser, Raffaella Carloni, and Stefano Stramigioli. Energy-efficient variable stiffness actuators. *IEEE transactions on robotics*, 27(5):865–875, 2011.

[25] Amir Jafari, Nikos G Tsagarakis, Bram Vanderborght, and Darwin G Caldwell. A novel actuator with adjustable stiffness (awas). In *2010 IEEE/RSJ International Conference on Intelligent Robots and Systems*, pages 4201–4206. IEEE, 2010.

[26] Ronald Van Ham, Bram Vanderborght, Michaël Van Damme, Björn Verrelst, and Dirk Lefeber. Maccepa, the mechanically adjustable compliance and controllable equilibrium position actuator: Design and implementation in a biped robot. *Robotics and Autonomous Systems*, 55(10):761–768, 2007.

[27] David V Gealy, Stephen McKinley, Brent Yi, Philipp Wu, Phillip R Downey, Greg Balke, Allan Zhao, Menglong Guo, Rachel Thomasson, Anthony Sinclair, et al. Quasi-direct drive for low-cost compliant robotic manipulation. In *2019 International Conference on Robotics and Automation (ICRA)*, pages 437–443. IEEE, 2019.

[28] Christian Hubicki, Jesse Grimes, Mikhail Jones, Daniel Renjewski, Alexander Spröwitz, Andy Abate, and Jonathan Hurst. Atrias: Design and validation of a tether-free 3d-capable spring-mass bipedal robot. *The International Journal of Robotics Research*, 35(12):1497–1521, 2016.

[29] Patrick M Wensing, Albert Wang, Sangok Seok, David Otten, Jeffrey Lang, and Sangbae Kim. Proprioceptive actuator design in the mit cheetah: Impact mitigation and high-bandwidth physical interaction for dynamic legged robots. *Ieee transactions on robotics*, 33(3):509–522, 2017.

[30] Kefei Wen, Tan Sy Nguyen, David Harton, Thierry Laliberté, and Clément Gosselin. A backdrivable kinematically redundant (6+ 3)-degree-of-freedom hybrid parallel robot for intuitive sensorless physical human–robot interaction. *IEEE Transactions on Robotics*, 37 (4):1222–1238, 2020.

[31] Louis-Thomas Schreiber and Clément Gosselin. Schönflies motion parallel robot (spara): a kinematically redundant parallel robot with unlimited rotation capabilities. *IEEE/ASME Transactions on Mechatronics*, 24(5):2273–2281, 2019.

[32] Clément Gosselin and Louis-Thomas Schreiber. Kinematically redundant spatial parallel mechanisms for singularity avoidance and large orientational workspace. *IEEE Transactions on Robotics*, 32(2):286–300, 2016.

[33] Clément Gosselin, Thierry Laliberté, and Audrey Veillette. Singularity-free kinematically redundant planar parallel mechanisms with unlimited rotational capability. *IEEE Transactions on Robotics*, 31(2):457–467, 2015.

[34] Svetlana Grosu, Laura De Rijcke, Victor Grosu, Joost Geeroms, Bram Vanderboght, Dirk Lefeber, and Carlos Rodriguez-Guerrero. Driving robotic exoskeletons using cable-based transmissions: a qualitative analysis and overview. *Applied Mechanics Reviews*, 70(6), 2018.

[35] Andre Schiele, Pierre Letier, Richard Van Der Linde, and Frans Van Der Helm. Bowden cable actuator for force-feedback exoskeletons. In *2006 IEEE/RSJ International Conference on Intelligent Robots and Systems*, pages 3599–3604. IEEE, 2006.

[36] Dongyang Chen, Youngmok Yun, and Ashish D Deshpande. Experimental characterization of bowden cable friction. In *2014 IEEE international conference on robotics and automation (ICRA)*, pages 5927–5933. IEEE, 2014.

[37] Varun Agrawal, William J Peine, and Bin Yao. Modeling of a closed loop cable-conduit transmission system. In *2008 IEEE International Conference on Robotics and Automation*, pages 3407–3412. IEEE, 2008.

[38] Jiting Li, Ruoyin Zheng, Yuru Zhang, and Jianchu Yao. ihandrehab: An interactive hand exoskeleton for active and passive rehabilitation. In *2011 IEEE International Conference on Rehabilitation Robotics*, pages 1–6. IEEE, 2011.

[39] Priyanshu Agarwal, Jonas Fox, Youngmok Yun, Marcia K O'Malley, and Ashish D Deshpande. An index finger exoskeleton with series elastic actuation for rehabilitation: Design, control and performance characterization. *The International Journal of Robotics Research*, 34(14):1747–1772, 2015.

[40] Antonio Frisoli, Fabio Salsedo, Massimo Bergamasco, Bruno Rossi, and Maria C Carboncini. A force-feedback exoskeleton for upper-limb rehabilitation in virtual reality. *Applied Bionics and Biomechanics*, 6(2):115–126, 2009.

[41] Michael Zinn, Bernard Roth, Oussama Khatib, and J Kenneth Salisbury. A new actuation approach for human friendly robot design. *The international journal of robotics research*, 23(4-5):379–398, 2004.

[42] Dongjun Shin, Irene Sardellitti, Yong-Lae Park, Oussama Khatib, and Mark Cutkosky. Design and control of a bio-inspired human-friendly robot. *The International Journal of Robotics Research*, 29(5):571–584, 2010.

[43] Stephen Paul Buerger. *Stable, high-force, low-impedance robotic actuators for human-interactive machines*. PhD thesis, Massachusetts Institute of Technology, 2005.

[44] Arthur Lutz and Irving H Wagman. A rolling diaphragm hydraulic micro-manipulator. *Electroencephalography and Clinical Neurophysiology*, 18(2):184–186, 1965.

[45] G Ganesh, Roger Gassert, Etienne Burdet, and Hannes Bleuler. Dynamics and control of an mri compatible master-slave system with hydrostatic transmission. In *IEEE International Conference on Robotics and Automation, 2004. Proceedings. ICRA'04. 2004*, volume 2, pages 1288–1294. IEEE, 2004.

[46] John P Whitney, Tianyao Chen, John Mars, and Jessica K Hodgins. A hybrid hydrostatic transmission and human-safe haptic telepresence robot. In *2016 IEEE international conference on robotics and automation (ICRA)*, pages 690–695. IEEE, 2016.

[47] John P Whitney, Matthew F Glisson, Eric L Brockmeyer, and Jessica K Hodgins. A low-friction passive fluid transmission and fluid-tendon soft actuator. In *2014 IEEE/RSJ international conference on intelligent robots and systems*, pages 2801–2808. IEEE, 2014.

[48] Sungbin Park, Kyungseo Park, Hwayeong Jeong, Wonseok Shin, and Jung Kim. A safe and rapidly switchable stiffness hydrostatic actuator through valve-controlled air springs. In *2021 IEEE/RSJ International Conference on Intelligent Robots and Systems (IROS)*, pages 9333–9338. IEEE.

[49] Alexander Gruebele, Samuel Frishman, and Mark R Cutkosky. Long-stroke rolling diaphragm actuators for haptic display of forces in teleoperation. *IEEE Robotics and Automation Letters*, 4(2):1478–1484, 2019.

[50] Catherine Véronneau, Jean-Philippe Lucking Bigué, Alexis Lussier-Desbiens, and Jean-Sébastien Plante. A high-bandwidth back-drivable hydrostatic power distribution system for exoskeletons based on magnetorheological clutches. *IEEE Robotics and Automation Letters*, 3(3):2592–2599, 2018.

[51] Charles Khazoom, Catherine Véronneau, Jean-Philippe Lucking Bigué, Jordane Grenier, Alexandre Girard, and Jean-Sébastien Plante. Design and control of a multifunctional ankle exoskeleton powered by magnetorheological actuators to assist walking, jumping, and landing. *IEEE Robotics and Automation Letters*, 4(3):3083–3090, 2019.

[52] Jeff Denis, Jean-Sébastien Plante, and Alexandre Girard. Low-level force-control of mr-hydrostatic actuators. *IEEE Robotics and Automation Letters*, 6(2):3849–3856, 2021.

[53] Catherine Véronneau, Jeff Denis, Louis-Philippe Lebel, Marc Denninger, Jean-Sébastien Plante, and Alexandre Girard. A lightweight force-controllable wearable arm based on magnetorheological-hydrostatic actuators. In *2019 international conference on robotics and automation (ICRA)*, pages 4018–4024. IEEE, 2019.

[54] Catherine Véronneau, Jeff Denis, Louis-Philippe Lebel, Marc Denninger, Vincent Blanchard, Alexandre Girard, and Jean-Sébastien Plante. Multifunctional remotely actuated 3-dof supernumerary robotic arm based on magnetorheological clutches and hydrostatic transmission lines. *IEEE Robotics and Automation Letters*, 5(2):2546–2553, 2020.

[55] Charles Khazoom, Pierre Caillouette, Alexandre Girard, and Jean-Sébastien Plante. A supernumerary robotic leg powered by magnetorheological actuators to assist human locomotion. *IEEE Robotics and Automation Letters*, 5(4):5143–5150, 2020.

[56] Eric Schwarm, Kevin M Gravesmill, and John P Whitney. A floating-piston hydrostatic linear actuator and remote-direct-drive 2-dof gripper. In *2019 international conference on robotics and automation (ICRA)*, pages 7562–7568. IEEE, 2019.

[57] Chunpeng Wang and John P Whitney. Series elastic force control for soft robotic fluid actuators. *arXiv preprint arXiv:2004.01269*, 2020.

[58] Natalie Burkhard, Samuel Frishman, Alexander Gruebele, J Peter Whitney, Roger Goldman, Bruce Daniel, and Mark Cutkosky. A rolling-diaphragm hydrostatic transmission for remote mr-guided needle insertion. In *2017 IEEE international conference on robotics and automation (ICRA)*, pages 1148–1153. IEEE, 2017.

[59] Samuel Frishman, Ali Kight, Ileana Pirozzi, Mela C Coffey, Bruce L Daniel, and Mark R Cutkosky. Enabling in-bore mri-guided biopsies with force feedback. *IEEE transactions on haptics*, 13(1):159–166, 2020.

[60] Samuel Frishman, Robert D Ings, Vipul Sheth, Bruce L Daniel, and Mark R Cutkosky. Extending reach inside the mri bore: A 7-dof, low-friction, hydrostatic teleoperator. *IEEE Transactions on Medical Robotics and Bionics*, 3(3):701–713, 2021.

[61] B. Kim and A. D Deshpande. An upper-body rehabilitation exoskeleton harmony with an anatomical shoulder mechanism: Design, modeling, control, and performance evaluation. *The International Journal of Robotics Research*, 2017.

[62] T. G. Sugar, J. He, E. J. Koeneman, J. B. Koeneman, R. Herman, H. Huang, R. S. Schultz, D. E. Herring, J. Wanberg, S. Balasubramanian, P. Swenson, and J. A. Ward. Design and control of rupert: A device for robotic upper extremity repetitive therapy. *IEEE Transactions on Neural Systems and Rehabilitation Engineering*, 2007.

[63] Saeed Hashemi and William K Durfee. Low friction, long-stroke rolling diaphragm cylinder for passive hydraulic rehabilitation robots. In *Frontiers in Biomedical Devices*, volume 40672, page V001T05A016. American Society of Mechanical Engineers, 2017.

[64] Saeed Hashemi, Steven Sobojinski, and William K Durfee. Low-friction antagonist hydraulic transmission using long-stroke rolling diaphragm cylinders. In *Fluid Power Systems Technology*, volume 58332, page V001T01A073. American Society of Mechanical Engineers, 2017.

[65] Stefano Chiaverini, Bruno Siciliano, and Luigi Villani. A survey of robot interaction control schemes with experimental comparison. *Transactions on mechatronics*, 1999.

[66] Alin Albu-Schäffer, Christian Ott, and Gerd Hirzinger. A unified passivity-based control framework for position, torque and impedance control of flexible joint robots. *The international journal of robotics research*, 2007.

[67] Andrea Calanca, Riccardo Muradore, and Paolo Fiorini. A review of algorithms for compliant control of stiff and fixed-compliance robots. *Transactions on Mechatronics*, 2015.

[68] Nicholas Paine, Sehoon Oh, and Luis Sentis. Design and control considerations for high-performance series elastic actuators. *IEEE/ASME Transactions on Mechatronics*, 19(3): 1080–1091, 2013.

[69] ZJ Palmor. Time delay compensation: Smith predictor and its modifications. In *The control handbook*. CRC press, 1996.

[70] Chae H An and John M Hollerbach. Dynamic stability issues in force control of manipulators. In *1987 American Control Conference*, pages 821–827. IEEE, 1987.

[71] Bruno Siciliano, Lorenzo Sciavicco, Luigi Villani, and Giuseppe Oriolo. Robotics: Modelling, planning and control, 2010.

[72] Felix Ruppert and Alexander Badri-Spröwitz. Series Elastic Behavior of Biarticular Muscle-Tendon Structure in a Robotic Leg. *Frontiers in Neurorobotics*, 13:64, August 2019. ISSN 1662-5218. doi: 10.3389/fnbot.2019.00064.

[73] Simon Mochon and Thomas A McMahon. Ballistic walking: An improved model. *Mathematical Biosciences*, 52(3-4):241–260, 1980.

[74] J.W. Grizzle, J. Hurst, B. Morris, Hae-Won Park, and K. Sreenath. MABEL, a new robotic bipedal walker and runner. In *American Control Conference, 2009. ACC '09.*, pages 2030 –2036, June 2009. doi: 10.1109/ACC.2009.5160550.

[75] Alexander Spröwitz, Alexandre Tuleu, Massimo Vespignani, Mostafa Ajallooeian, Emilie Badri, and Auke Ijspeert. Towards Dynamic Trot Gait Locomotion: Design, Control and Experiments with Cheetah-cub, a Compliant Quadruped Robot. *Int. J. of Robotics Research*, 32(8):932–950, 2013. ISSN 0278-3649.

[76] Atabak Nejadfard, Steffen Schütz, Krzysztof Mianowski, Patrick Vonwirth, and Karsten Berns. Design of the musculoskeletal leg CARL based on the physiology of mono-articular and biarticular muscles in the human leg. *Bioinspiration & Biomimetics*, 14(6):066002, September 2019. ISSN 1748-3190. doi: 10.1088/1748-3190/ab3896.

[77] Yong-Jae Kim. Anthropomorphic low-inertia high-stiffness manipulator for high-speed safe interaction. *IEEE Transactions on robotics*, 33(6):1358–1374, 2017.

[78] Kenichi Narioka, Andre Rosendo, Alexander Spröwitz, and Koh Hosoda. Development of a Minimalistic Pneumatic Quadruped Robot for Fast Locomotion. In *Proceedings of IEEE International Conference on Robotics and Biomimetics (ROBIO)*, pages 307–311, Guangzhou, China, 2012. doi: 10.1109/ROBIO.2012.6490984.

[79] Simon Rutishauser, Alexander Spröwitz, Ludovic Righetti, and A.J. Ijspeert. Passive compliant quadruped robot using central pattern generators for locomotion control. In *Proceedings of 2nd IEEE RAS & EMBS International Conference on Biomedical Robotics and Biomechatronics (Biorob)*, Scottsdale, AZ, USA, October 2008. IEEE Biorob 2008. doi: 10.1109/BIOROB.2008.4762878.

[80] Marc H. Raibert. Trotting, pacing and bounding by a quadruped robot. *Journal of Biomechanics*, 23(Supplement 1):79–81, 1990. ISSN 0021-9290. doi: 10.1016/0021-9290(90)90043-3.

[81] Claudio Semini, Nikos G. Tsagarakis, Emanuele Guglielmino, Michele Focchi, Ferdinando Cannella, and Darwin G. Caldwell. Design of HyQ–a hydraulically and electrically actuated quadruped robot. *Proceedings of the Institution of Mechanical Engineers, Part I: Journal of Systems and Control Engineering*, 225(6):831–849, 2011.

[82] Hans Johannesson. *On The Optimization Of Hydraulic Cylinder Seals*. PhD thesis, 1980.

[83] Hiroyuki Nabae, Morizo Hemmi, Yoshiharu Hirota, Tohru Ide, Koichi Suzumori, and Gen Endo. Super-low friction and lightweight hydraulic cylinder using multi-directional forging magnesium alloy and its application to robotic leg. *Advanced Robotics*, 32(9):524–534, 2018.

[84] RMcN Alexander and HC Bennet-Clark. Storage of elastic strain energy in muscle and other tissues. *Nature*, 265(5590):114–117, 1977.

[85] Pierre Cherelle, Victor Grosu, Manuel Cestari, Bram Vanderborght, and Dirk Lefeber. The AMP-Foot 3, new generation propulsive prosthetic feet with explosive motion characteristics: design and validation. *BioMedical Engineering OnLine*, 15:285, 2016. ISSN 1475-925X. doi: 10.1186/s12938-016-0285-8.

[86] H. Mineshita, T. Otani, K. Hashimoto, M. Sakaguchi, Y. Kawakami, H. O. Lim, and A. Takanishi. Robotic Ankle Mechanism Capable of Kicking While Jumping and Running and Adaptable to Change in Running Speed. In *2019 IEEE-RAS 19th International Conference on Humanoid Robots (Humanoids)*, pages 505–510, October 2019. doi: 10.1109/Humanoids43949.2019.9035057.

[87] Syn Schmitt and Michael Günther. Human leg impact: energy dissipation of wobbling masses. *Archive of Applied Mechanics*, 81(7):887–897, July 2011. ISSN 0939-1533, 1432-0681. doi: 10.1007/s00419-010-0458-z.

[88] R. Niiyama, A. Nagakubo, and Y. Kuniyoshi. Mowgli: A Bipedal Jumping and Landing Robot with an Artificial Musculoskeletal System. In *2007 IEEE International Conference on Robotics and Automation*, pages 2546–2551, 2007. doi: 10.1109/ROBOT.2007.363848.

[89] Qin Tu, Yanjie Wang, Donghai Yue, and Frank Agyen Dwomoh. Analysis on the Impact Factors for the Pulling Force of the McKibben Pneumatic Artificial Muscle by a FEM Model. *Journal of Robotics*, 2020:4681796, 1 2020. ISSN 1687-9600. doi: 10.1155/2020/4681796.

[90] R. McN Alexander. Three Uses for Springs in Legged Locomotion. *The International Journal of Robotics Research*, 9(2):53–61, April 1990. ISSN 0278-3649, 1741-3176. doi: 10.1177/027836499000900205.

[91] Felix Grimminger, Avadesh Meduri, Majid Khadiv, Julian Viereck, Manuel Wüthrich, Maximilien Naveau, Vincent Berenz, Steve Heim, Felix Widmaier, Thomas Flayols, Jonathan Fiene, Alexander Badri-Spröwitz, and Ludovic Righetti. An open torque-controlled modular robot architecture for legged locomotion research. *IEEE Robotics and Automation Letters*, 5(2):3650–3657, 2020. doi: 10.1109/LRA.2020.2976639.

[92] Esa Kostamo, Michele Focchi, Emanuele Guglielmino, Jari Kostamo, Claudio Semini, Jonas Buchli, Matti Pietola, and Darwin Caldwell. Magnetorheologically Damped Compliant Foot for Legged Robotic Application. *Journal of Mechanical Design*, 136(2), 2013.

[93] Emanuele Guglielmino, Charles W Staimmers, Kevin A Edge, Tudor Sireteanu, and Danut Stancioiu. Damp-by-wire: magnetorheological vs. friction dampers. *IFAC Proceedings Volumes*, 38(1):340–345, 2005.

[94] Philippe Fauteux, Michel Lauria, Benoît Heintz, and François Michaud. Dual-differential rheological actuator for high-performance physical robotic interaction. *IEEE Transactions on Robotics*, 26(4):607–618, 2010.

[95] Elena Garcia, Juan Carlos Arevalo, Gustavo Muñoz, and P Gonzalez-de Santos. Combining series elastic actuation and magneto-rheological damping for the control of agile locomotion. *Robotics and Autonomous Systems*, 59(10):827–839, 2011.

[96] Dominique Chapuis, Roger Gassert, Etienne Burdet, and Hannes Bleuler. A hybrid ultrasonic motor and electrorheological fluid clutch actuator for force-feedback in mri/fmri. In *2008 30th Annual International Conference of the IEEE Engineering in Medicine and Biology Society*, pages 3438–3442. IEEE, 2008.

[97] N. Takesue, G. Zhang, J. Furusho, and R. Sakaguchi. Precise position control of robot arms using a homogeneous er fluid. In *Proceedings. 1998 IEEE International Conference on Robotics and Automation (Cat. No.98CH36146)*, volume 3, pages 2470–2475 vol.3, 1998. doi: 10.1109/ROBOT.1998.680712.

[98] Manuel Catalano, Giorgio Grioli, Manolo Garabini, Felipe Weilemann Belo, Andrea Di Basco, Nikos Tsagarakis, and Antonio Bicchi. A variable damping module for variable impedance actuation. In *2012 IEEE International Conference on Robotics and Automation*, pages 2666–2672. IEEE, 2012.

[99] Babak Ebrahimi, Mir Behrad Khamesee, and Farid Golnaraghi. A novel eddy current damper: theory and experiment. *Journal of Physics D: Applied Physics*, 42(7):075001, 2009.

[100] Abdenbi Mohand-Ousaid, Guillaume Millet, Stéphane Régnier, Sinan Haliyo, and Vincent Hayward. Haptic interface transparency achieved through viscous coupling. *The International Journal of Robotics Research*, 31(3):319–329, 2012.

[101] Andrew HC Gosline and Vincent Hayward. Eddy current brakes for haptic interfaces: Design, identification, and control. *IEEE/ASME Transactions On Mechatronics*, 13(6): 669–677, 2008.

[102] Henry A Sodano, Jae-Sung Bae, Daniel J Inman, and W Keith Belvin. Improved concept and model of eddy current damper. 2006.

[103] S. D. Eppinger and W. P. Seering. Three dynamic problems in robot force control. *IEEE Transactions on Robotics and Automation*, 8(6):751–758, 1992.

[104] S. Eppinger and W. Seering. Understanding bandwidth limitations in robot force control. In *IEEE International Conference on Robotics and Automation*, volume 4, pages 904–909, 1987.

[105] S. Eppinger and W. Seering. Introduction to dynamic models for robot force control. *IEEE Control Systems Magazine*, 7(2):48–52, 1987.

[106] W. Townsend and J. Salisbury. The effect of coulomb friction and stiction on force control. In *Proceedings. 1987 IEEE International Conference on Robotics and Automation*, volume 4, pages 883–889, 1987.

[107] R. Roberts, R. Paul, and B. Hillberry. The effect of wrist force sensor stiffness on the control of robot manipulators. In *Proceedings. 1985 IEEE International Conference on Robotics and Automation*, volume 2, pages 269–274, 1985.

[108] R. Wrobel, M. Lukaniszyn, M. Jagiela, and K. Latawiec. A new approach to reduction of the cogging torque in a brushless motor by skewing optimization of permanent magnets. *Electrical Engineering*, 2003.

[109] M. Piccoli and M. Yim. Cogging torque ripple minimization via position-based characterization. In *Robotics: Science and Systems 2014*, 2014.